

https://dspace.org/

Developing an advanced understanding of Au-U-C associations in the Witwatersrand Basin : using traditional and experimental techniques

Woods, Tremain

2017

http://hdl.handle.net/10539/23611

Woods, Tremain Hugh Encombe (2017) Developing an advanced understanding of Au-U-C associations in the Witwatersrand Basin: using traditional and experimental techniques, University of the Witwatersrand, Johannesburg, <http://hdl.handle.net/10539/23611>

Downloaded from a DSpace repository. https://dspace.org/

Developing an advanced understanding of Au-U-C Associations in the Witwatersrand Basin: Using traditional and experimental techniques

Tremain Woods

A thesis submitted to the Faculty of Science, University of the Witwatersrand, Johannesburg, in fulfilment of the requirements for the degree of Doctor of Philosophy.

School of Geosciences
Johannesburg
2017

Declaration

I declare that this dissertation is my own, unaided work. It is being submitted for the Degree of Doctor of Philosophy in the University of the Witwatersrand, Johannesburg. It has not been submitted before for any degree or examination in any other University.

_____

Tremain Woods

_____ Day of _____ 2017

Abstract

The Witwatersrand Basin is the single largest gold source ever found. Gold exhibits a strong association with carbon and as much as 40% of the gold mined from the metasedimentary basin is found in carbon-bearing reefs. Carbon also contains high concentrations of uranium minerals. Although the carbon, gold and uranium association is well-documented, there is little consensus about the formation of these associations. Thus, a detailed geological investigation was undertaken on material from 12 carbon-bearing reefs throughout the Central Rand Group from across the Witwatersrand Basin. Concurrently a novel experimental component of the investigation was conducted in an attempt to simulate, for the first time ever, the Au-U-C associations in the Witwatersrand Basin.

Petrography revealed that in more than 60 samples from carbon-bearing Witwatersrand Reefs, gold most often occurred between carbon spindles, as minor inclusions within carbon spindles and as coatings to the carbon forms. Furthermore, gold within the conglomerates occurred as veinlets, rims on oxide grains, as micro-particles in phyllosilicates and secondary quartz and as inclusions in secondary pyrite grains. These textures were interpreted as secondary features formed during metamorphism and alteration of the Basin. Hydrocarbons displayed textures that were also interpreted as being secondary; these included nodules that infilled interstices within the reef matrix and multiple phases of hydrocarbon enclosed within spindles comprising carbon seams. Electron microscope images were taken of a hydrothermal carbon nodule enclosed in cubic pyrite. The images revealed sheet-like hydrocarbons and fibrous/tube-like forms. Critically, the hydrothermal carbon nodule also contained micro-particulate crystalline gold and pyrite within vesicles or gas bubbles within in the nodule. In the carbon seams, uraninite occurred within the spindles. The uraninite appeared fragmented and displaced by hydrocarbon growth structures. Therefore, it was suggested that uraninite was the precursor to secondary hydrocarbon and gold precipitation.

Detailed petrography revealed the textures of particulate Au-U-C associations in the Witwatersrand Basin but elemental micro-mapping was necessary to determine the distribution of metals, major elements, trace elements and rare earth elements within carbon seams and carbon nodules. Carbonaceous materials were closely associated with disseminated elemental sulphur, mobile elements and rare earth elements. The occurrence of mobile elements and sulphur disseminated through the hydrocarbon suggested that the carbonaceous matter was formed from a fluid phase.

Organic sulphur compounds in fluids derived from sedimentary organic matter are theorised to enhance the solubility of various metals in hydrocarbon phases. The occurrence of Au, As, Ag, Ti, V, U, Hg, Fe, Co, Cu, Cr, Mn and other metals in the hydrocarbons in the Basin indicated that a process other than radiolytic polymerisation may have been involved in the concentration of certain metals from a liquid phase. The similarity of metals concentrated in Witwatersrand carbonaceous matter to those of modern day crude oils and petroleum liquids derived from the degradation of Type I kerogens provided a potential mechanism for remobilisation in the Basin.

These observed Au-U-C associations laid the foundation for experimental simulation. Catalytic Chemical Vapour Deposition experiments used acetylene and hydrogen gas to precipitate solid nanocarbon materials onto uranium-bearing powders. Results showed that for increasing uranium concentration, greater masses of carbonaceous materials were deposited onto the uranium-bearing powders. Therefore, carbonaceous product deposition was confirmed to be correlated with uranium concentrations. When uranium was leached out of the samples, the mass of carbon deposited was significantly decreased. The growth of carbon started at 300°C, was physically visible at 450°C and completely encapsulated the powders forming a product similar to Witwatersrand carbon seams at 600°C. Raman spectra indicated that the experimentally formed carbonaceous products had similar signatures to those of Witwatersrand carbon. The simulation of C-U associations was confirmed by electron microscopy, which showed that carbon nanotubes, carbon nanofibers and sheet-like materials precipitated onto uraninite grains under experimental conditions. These experimentally formed structures were comparable to those observed in Witwatersrand seam carbon, especially the sheet-like and fibrous/tube-like materials.

It was suspected that gold distribution in carbon seams could provide useful data for hydrocarbon formation processes. Consequently micro-computed tomography, in conjunction with automated electron dispersive spectra, was used to examine the distribution of gold in three dimensions. The sample analysed was a carbon seam from the Carbon Leader Reef that contained exceptionally high gold grades. Gold in this carbon seam was found to occur most concentrated between carbon spindles in addition to small particles within spindles. Furthermore gold concentrations were highest at the footwall and hanging wall contacts and decreased towards the centre of the seam. The hydrocarbon spindle form also changed from bulbous at the contacts to more uniform and elongated in the centre of the carbon seam. It was therefore suggested that hydrocarbon growth and gold

crystallisation in carbon seams was akin to crystal growth in quartz veins, where spindles are elongated parallel to the principal stress direction.

In order to experimentally simulate Au-U-C associations, gold in solution at high pressures was required. Solvothermal experiments that used an autoclave and sucrose in solution were undertaken. Sucrose represented a common component found in petroleum liquids derived from Type I kerogens, similar to what is postulated for the Witwatersrand Basin. The experiments showed that hydrocarbons could precipitate at lower temperatures compared to temperatures observed in the Basin – c.a. 180°C. In addition, the effect of pressure was to enhance the breakdown of sucrose into more sheet-like carbonaceous products when 800 kPa of nitrogen gas was added to the reaction vessel. Finally, a solution of 0.01 M aurichloric acid was added to the experiments to determine if gold in solution would be precipitated during hydrocarbon precipitation. Results showed that almost all the gold was precipitated from solution as crystalline and nano-particulate gold. Strikingly, gold that precipitated was enclosed by hydrocarbons and was also seen to adhere onto the surfaces of sheet-like carbonaceous materials, indicating that the gold and hydrocarbon are intimately associated and that hydrocarbons facilitate the precipitation of gold from solution.

Although experimental conditions could not match geological conditions exactly, the experimental products were comparable to the Witwatersrand Au-U-C associations. The results from this research show that catalytic electron promotion of uranium and other metals play an important role in hydrocarbon structuring and precipitation. The model of fluid remobilisation of hydrocarbons and gold is further enhanced by the evidence presented in this study.

In conclusion, remobilisation textures were seen in the Au-U-C associations from the Witwatersrand Basin. Similar associations were experimentally precipitated using a hydrocarbon and gold-rich fluid.

Dedication

For Mom, Dad and Nathan -

Your support taught me that failure is merely an opportunity to learn

Acknowledgements

Throughout the course of this study guidance, assistance and invaluable input was provided by supervisors: Prof. Gillian Drennan, Prof. Shane Durbach and Prof. Judith Kinnaird. The research, learning and growth documented in this thesis would not be possible without you, thank you.

The research produced in this thesis relied on the assistance of a number of collaborators, an exceptional amount of time and effort was contributed and the author is grateful to each one. The paper is an output of the Witwatersrand Basin research team in the DST-NRF Centre of Excellence for Integrated Mineral and Energy Resource Analysis (CIMERA).

The author is grateful to Ms. M. Amwaama, Mr. N. Pao and Mr. A. Moya for their valuable input and ideas during the course of the CCVD experiments (Chapter 5). Additionally, we are grateful to Mr. B. Chassoulas and Mr. T. Dzara for assistance with the equipment used in the experiments. Mr. A. Mosai and Prof. H Tutu for are thanked their assistance with leeching uranium. The author appreciates the valuable input and ideas during the course of this study by Prof. L. Robb and Prof. J. Kinnaird. Additionally, the author is grateful to the Materials Sciences Division of iThemba LABS for the assistance during the long hours of data acquisition for the PIXE results. The PIXE results are the result of the tireless assistance of Dr. W. Przybylowicz and the quality of these are reflected in Chapter 4. The author thanks Dr. P. Horvath for assistance with the microprobe mapping that supplemented PIXE results. Additionally the author is also grateful to Mr. M. Teracin for his assistance in digitising the map and stratigraphic column of the Witwatersrand Basin.

The author also made use of the expertise of Dr. K. Carlson, Dr. H. Hughes and Mr. I. Tonžetić for data acquisition, processing and interpretation in Chapter 6, the author is grateful to them for the assistance provided. The author is thankful to Prof. A. Ziegler, Dr. D. Reddy, Dr. R. Erasmus and Mr. J. Gerber of the Microscopy and Microanalysis Unit at the University of the Witwatersrand for the assistance with the microscopy and analyses presented throughout this thesis. Lastly, a thesis requires a lot of proof reading, thank you to Mr. R. Douglas and Ms. A. Eliot for their assistance throughout the course of this study. Finally, to everyone who assisted this study in some way, big or small, thank you.

The author would like to acknowledge the funding centres, without the following initiatives this research would not have been possible. DST-NRF Centre of Excellence in Strong Materials at the University of the Witwatersrand provided funding, support and equipment during the course of this study. CIMERA, provided the last funds required to complete the final experiments, analyses and finalise the publications produced from this research. Other sources of financial assistance included: the GSSA's REI funds, the Society for Economic Geologists' Hugh E. McKinstry fund, J.C. Carstens Post Graduate Funds and the Faculty Research Committee of the University of the Witwatersrand.

Table of Contents

Declaration 2

Abstract 3

Dedication 6

Acknowledgements 7

List of Figures 13

List of Tables 16

List of Appendices 17

List of Abbreviations 18

1 INTRODUCTION AND GEOLOGICAL BACKGROUND 19

1.1 Introduction 19

1.2 This Study 20

1.3 Stratigraphy and Sedimentology 21

1.4 Gold fields 24

1.5 Metamorphism 25

1.6 Structure and Tectonics 26

1.7 Mineralisation 27

1.7.1 Gold 27

1.7.2 Pyrite 28

1.7.3 Uranium-bearing Phases 28

1.7.4 Carbonaceous Matter 29

1.7.5 Other Minerals 31

1.8 Mineralisation Models and Phases 32

1.9 Importance of Fluids 34

1.10 Metal solubility in Oils and Brines 37

1.11 Carbon Nanostructures: Reactions and Applications 39

1.12 Publications and format of Chapters 2 - 8 40

2 METHODOLOGY AND EXPERIMENT SET UP 41

2.1 Sampling and Sample Preparation 41

2.2 Petrographic Microscopy 42

2.3 Chemical Analyses 43

2.4 Proton Induced X-ray Emission Analysis 44

2.5 Electron Probe Micro-Analysis 46

2.6 Laser Raman Spectroscopy 46

2.7 Micro-CT scanning 46

2.8 Scanning Electron Microscopy (SEM) and Auto-SEM 47

2.9 Transmission Electron Microscopy 48

2.10 Thermal Analysis 49

2.11 Experimental Growth of Carbon Nanostructures (CNSs) 49

2.12 Solvothermal Experiment Setup 51

3 PETROGRAPHIC STUDY 54

3.1 Petrography and Variation of Au-U-C Features of Various Witwatersrand Reefs 54

3.1.1 Uranium-Bearing Phases 54

3.1.2 Gold 57

3.1.3 Carbon Forms 60

3.1.4 Sulphides and Pyrite 69

3.1.5 Alteration and Other Minerals 72

3.2 Petrography Discussion 74

3.3 Conclusions 76

4 PIXE STUDY OF ELEMENT DISTRIBUTION WITHIN CARBON FORMS 77

4.1 Introduction 77

4.2 PIXE Elemental Maps of Seam Carbon 77

4.2.1 "C" Reef carbon seam in contact with quartz vein 78

4.2.2 CLR carbon seam cross-cut by calcite veinlets 80

4.2.3 Basal Reef carbon spindles 82

4.2.4 Vaal Reef carbon spindles and fractured pyrite 84
4.3 PIXE Study of Elemental Distribution within Carbon Nodules 87
4.3.1 Steyn Reef carbon nodules with uraninite grains 87
4.3.2 VCR carbon nodule 89
4.3.3 "C" – Reef porous nodule 91
4.4 PIXE Discussion 94
4.5 Conclusions 97
5 CATALYTIC CHEMICAL VAPOUR DEPOSITION OF CARBON ONTO URANIUM-BEARING POWDERS TO SIMULATE FORMATION OF SEAM CARBON IN WITWATERSRAND REEFS 98
5.1 Introduction 98
5.2 Product Mass 99
5.3 Laser Raman Spectrometry 105
5.4 Thermogravimetric Analyses 107
5.5 Transmission Electron Microscopy 108
5.6 Discussion 111
5.7 Conclusions 115
6 MICRO-CT DATA FROM THE CARBON LEADER REEF 117
6.1 Introduction 117
6.2 Sample and Petrography 117
6.3 Results 118
6.3.1 Internal structure of the carbon seam 118
6.4 Minerals associated with gold in between the carbon spindles 122
6.4.1 Gold distribution in Three Dimensions 126
6.5 Discussion 129
6.5.1 Spindles and Mineralisation 129
6.5.2 3D Gold Distribution 130
6.6 Conclusions 131
7 SOLVOTHERMAL EXPERIMENTS 133

7.1 Introduction 133
7.2 Mass and Physical Changes 134
7.3 Laser Raman Spectroscopy 135
7.4 Thermal Analysis 137
7.5 Transmitted Electron Microscopy 138
7.6 Gold in Solution: Replicating Au-U-C associations 139
7.7 Discussion 143
7.8 Conclusions 145

8 DISCUSSION AND CONCLUSION 147

8.1 Discussion and Summary of Findings 147
8.2 Implications 151
8.3 Recommendations 153

References 154

Appendices .....

List of Figures

Figure 1.1 Geological Map of the Witwatersrand Basin in South Africa 22
Figure 1.2 Stratigraphic Column of the Witwatersrand Basin 23
Figure 1.3 Schematic Diagram showing the form of Carbonaceous Matter 30
Figure 1.4 Schematic Diagram of Petroleum Generation 35
Figure 2.1 CCVD experimental set-up. 50
Figure 2.2 Schematic diagram of a solvothermal experimental set-up 52
Figure 3.1 Reflected light image of secondary phases of brannerite and coffinite minerals in BDN2 55
Figure 3.2 Reflected light image of carbon seam spindles containing “blown-up” uraninite in CREEF EM1 56
Figure 3.3 Reflected light image of relict uraninite grains in MGS4063 57
Figure 3.4 Reflected light image of gold in veinlets and phyllosilicate matrix minerals in MGS4071 58
Figure 3.5 Reflected light image of gold within euhedral pyrite in MGS6514 59
Figure 3.6 Reflected light image of various gold forms in MGS4071 60
Figure 3.7 Reflected light image of rounded carbon nodules in CREEF07 61
Figure 3.8 Reflected light image of an irregular carbon nodule in VCR1 62
Figure 3.9 Reflected light image of a thin discontinuous carbon seam in CREEF07 63
Figure 3.10 Reflected light image of carbon spindles with gold between the filaments in WD20 64
Figure 3.11 Reflected light image of a carbon seam cut by calcite veins in DFN10 65
Figure 3.12 Reflected light image of carbon seam spindles with less U and no calcite veins in DFN10 65
Figure 3.13 Electron Microscope Image of the Carbon Nodule in Recrystallised Pyrite 66
Figure 3.14 Electron Microscope Image showing the micron-scale inclusions of minerals 67
Figure 3.15 Electron Microscope Image showing the micron forms of carbonaceous materials 68
Figure 3.16 Reflected light image of typical rounded pyrite textures in LGM6 70
Figure 3.17 Reflected light image of euhedral pyrite within a phyllosilicate veinlet in LGM16 ... 71

Figure 3.18 Reflected light image of multiple pyrite forms in a single grain in MGS6513 71
Figure 3.19 Transmitted, plane-polarised light image of alteration minerals in BDN2..... 73
Figure 3.20 Transmitted light image of alteration minerals within matrix of BDN2 73
Figure 4.1 Reflected light image of carbon spindles and gold analysed in CREEF01 78
Figure 4.2 PIXE elemental micro-maps of CREEF01..... 79
Figure 4.3 Reflected light image of carbon seam cut by calcite veinlets in DFN10..... 80
Figure 4.4 PIXE elemental micro-maps of DFN10..... 81
Figure 4.5 Reflected light image of elongated carbon spindles in LGM3 82
Figure 4.6 PIXE elemental micro-maps of LGM3 83
Figure 4.7 Reflected light image of rounded carbon spindles formed around pyrite in MGS6513 85
Figure 4.8 PIXE elemental micro-maps of MGS6513 86
Figure 4.9 Reflected light image of carbon nodules encapsulating rounded uraninite in PSGM 87
Figure 4.10 PIXE elemental micro-maps of PSGM 88
Figure 4.11 Reflected light image of carbon nodule in the VCR1..... 89
Figure 4.12 PIXE elemental micro-maps of a carbon nodule from the VCR..... 90
Figure 4.13 Reflected light image of a porous nodule from the “C’ = Reef..... 92
Figure 4.14 PIXE elemental micro-maps of “C” – Reef nodule 93
Figure 5.1 Change in appearance of CCVD experimental products..... 100
Figure 5.2 The mass of the black product formed during CCVD growth 101
Figure 5.3 The mass of product formed vs Uranium concentration, for <32 µm uraniferous powders from CCVD reactions at 600°C; the line shows the exponential regression for the IDAM10, DH034 and HILG13 data. The HILG19 data is a statistical outlier. Each symbol represents the average of 3 experiments. 102
Figure 5.4 The mass of product formed during the CCVD reaction with <32 µm uraniferous powders at 600°C, versus the concentration of Copper. The fitted line demonstrates the observed trend if the HILG19 data, a statistical outlier is considered separately. 103
Figure 5.5 The mass of product formed during the CCVD reaction with <32 µm uraniferous powders at 600°C, versus the concentration of (a) Molybdenum and (b) Strontium. The fitted line

demonstrates the observed trend if the HILG19 data, a statistical outlier is considered separately. 104
Figure 5.6 Raman spectra of the CCVD experimental products and Witwatersrand Carbon samples 105
Figure 5.7 The first derivative curve of the TGA analysis of the CCVD products (for HILG19 powders <32 µm) from 450°C and 600°C experiments 107
Figure 5.8 TEM micrographs of the CNSs that formed in the CCVD experiments..... 109
Figure 5.9 Additional TEM micrographs of the CNSs that formed in the CCVD experiments 110
Figure 5.10 SEM Images of Beisa Reef compared to CCVD sample..... 111
Figure 6.1 Photograph of Carbon Leader Reef sample..... 118
Figure 6.2. Stitched petrographic image of CLR ore block. 119
Figure 6.3 Enlarged reflected light images of CLR sample features 120
Figure 6.4. SEM BSE image overlaid over stitched optical microphotograph showing areas mapped by EDS. 123
Figure 6.5 BSE image of seam portion of CLR sample 124
Figure 6.6 Mineral classification of CLR sample as shown by Auto-SEM-EDS 125
Figure 6.7. Gold regions of interest from µCT data threshold 126
Figure 6.8. Tomography slices through CLR sample. The slices are taken from the base of the seam (a) moving up towards the quartzite hanging wall (h). 128
Figure 7.1 Product formed during solvothermal reaction of sucrose and HILG13 < 32µm 134
Figure 7.2 Raman spectra of the solvothermal products compared to Witwatersrand Carbon seam 136
Figure 7.3 First derivative graphs of solvothermal products using HILG13 <32um powders 137
Figure 7.4 TEM images of solvothermal products 138
Figure 7.5 TEM of Solvothermal products formed on HILG13 32-75µm powders..... 139
Figure 7.6 Solution produced by solvothermal gold in solution experiment..... 141
Figure 7.7 Optical microscope image of the solvothermal products formed from the gold in solution solvothermal experiment 141
Figure 7.8 TEM images of gold products precipitated from a gold solution 142

List of Tables

Table 1.1 Typical hydrocarbon composition of a subsurface petroleum from the Bruce Oil Field (After England et al., 1987) 36
Table 1.2 Compositions of various hydrothermal fluids compared to modern day sea water 38
Table 2.1 Reefs sampled and the locality of the reefs in the Witwatersrand Basin 41
Table 2.2 Samples selected for PIXE micro-maps 45
Table 2.3 Specific gravity of minerals commonly found in Witwatersrand Carbon seams 47
Table 5.1 Powdered substrates placed under CCVD conditions, arranged in increasing uranium concentration per size fraction 99
Table 5.2 Product masses of standard HILG19 powders compared to those in which U had been leached. 105
Table 5.3 Thermal analyses and laser Raman data for the carbonaceous products formed by CCVD at 450°C and 600°C as compared with laser Raman data for Witwatersrand Carbon. 106
Table 7.1 Raman and Thermal Analyses for solvothermal products compared to Witwatersrand Carbonaceous Materials 136

List of Appendices

A. Peer-Reviewed Papers
B. Sample List for this study
C. Microscope Petrography Summary Tables
D. Additional SEM Images
E. PIXE Data from Carbon Seams
F. PIXE Data from Carbon Nodules
G. EPMA Additional WDS Data
H. CCVD Supplementary Data
I. CT and Auto-SEM Supplementary Data
J. Solvothermal Supplementary Data

List of Abbreviations

µCT – Micro-Computed Tomography

Au-U-C – Gold-Uranium-Carbon

CCVD – Catalytic Carbon Vapour Deposition

CLR – Carbon Leader Reef

CNSs – Carbon Nanostructures

CRG – Central Rand Group

"C" – Reef – Crystalkop Reef

EBS - Elastic Backscattering

EDS – Energy Dispersive X-ray Spectroscopy

EPMA – Electron Probe Micro-Analyses

g/t. - grams per tonne

ICP-OES – Inductively Coupled Plasma Optical Emission Spectroscopy

LRS – Laser Raman Spectroscopy

MIA – Multiple Image Alignment

MMU – Microscopy and Microanalysis Unit

NSO – Nitrogen Sulphur Oxygen compounds

OSC – Organic Sulphur Compounds

PIXE – Proton Induced X-ray Emission

ppm – Parts per Million (equivalent of µg/g)

REE – Rare Earth Elements

SEM – Scanning Electron Microscopy

TEM – Transmission Electron Microscopy

TGA – Thermogravimetric Analysis

VLS – Vapour-Liquid-Solid

VCR – Ventersdorp Contact Reef

WRG – West Rand Group

WDS – Wave Dispersive Spectroscopy

XRF – X-ray Fluorescence Spectroscopy

1 Introduction and Geological Background

1.1 Introduction

The Witwatersrand Basin is unique in terms of its geology, mineralisation and economic significance. The Basin has yielded as much as 40% of all gold ever mined since its discovery in 1886 (McCarthy, 2009). The Basin remains 10 times larger than the second largest gold field (Grasberg Igneous Complex) discovered to date (Phillips and Powell, 2011). The Witwatersrand Basin is also a well preserved Archean Basin, and provides insight to a much younger Earth (Smart *et al*., 2016). Research on the Witwatersrand Basin spans over 110 years and almost every aspect has been investigated in some capacity. However, controversy still surrounds the origin and formation of the mineralisation in the Witwatersrand Basin.

Given its economic and cultural relevance, gold is the most researched mineral within the Witwatersrand Basin (e.g. Phillips and Law, 2000). The source of the gold and the mineralisation processes that influenced the gold, have long been debated (Minter, 1999; Frimmel and Minter, 2002). Other minerals such as pyrite, uraninite and platinoids have provided evidence for speculation about the origins of the mineralisation in the Basin (Cousins, 1973; Simpson and Bowles, 1977; Large *et al*., 2013), but research remains focussed on the processes that concentrated gold. Gold in the Witwatersrand Basin exhibits a unique association with carbon and uranium. As much as 40% of the gold found in the basin is associated with carbonaceous materials (Mossman *et al*., 2008). This association has garnered much attention and it is clear from the research that the relationship between the two is still not fully understood (England *et al*., 2002; Heinrich, 2015).

The focus of this research project was to thoroughly examine and replicate the various Au-U-C associations in the Witwatersrand Basin in order to better understand the processes that resulted in this association and their impact on gold distribution.

1.2 This Study

This research sought to expand on the current wealth of knowledge and by experimentally replicating the Au-U-C associations and develop a more advanced understanding of the processes that led to the formation of the Witwatersrand Basin. Hence the primary aim of this research project was to examine and then experimentally simulate a possible mechanism for the formation of gold-uranium-carbon deposits within the Basin. To accomplish this, the research conducted had to be a collaborative effort of geological and chemical investigations. The dual nature of this research meant that two sets of objectives and hypotheses/key questions were set.

The main hypothesis tested was that the carbon that is observed in carbon seams and nodules in the Witwatersrand Basin were formed by structured nanocarbon growth around grains of detrital uraninite, or a similar process thereof. A more traditional geological investigation was undertaken to characterise the carbon forms that occur within the Witwatersrand Basin. The objectives of the geological investigation included:

- An investigation into the gold variations within the Witwatersrand Basin,
- Examining the microscopic and macroscopic forms of carbon in the gold bearing reefs,
- Determining the chemical composition and signature of carbonaceous materials and surrounding minerals (especially metamorphic and hydrothermal minerals),
- Characterisation of the Au-U-C associations to guide experiments,
- Developing and adding to the models of formation for gold and hydrocarbons,

From a chemical perspective, the experimental growth of carbonaceous products was found to be commonplace in catalysis and strong materials research (Coleman *et al*., 2006; Coville *et al*., 2011). There were a number of useful experimental techniques that, if adapted, would have suited a vapour/liquid-solid (VLS) growth mechanism of structured nanocarbon materials. The techniques adapted were catalytic chemical vapour deposition (CCVD, as in (Moshkalyov *et al*., 2004) and solvothermal synthesis (Kuang *et al*., 2004; Deshmukh *et al*., 2010). In order to experimentally replicate carbon, as it was observed in the Witwatersrand Basin, CCVD and solvothermal techniques were adapted to simulate conditions that may have brought about its

formation. The aim of the chemical experiments was to replicate one or more of the carbon forms associated with uranium bearing minerals, as was observed in the Witwatersrand samples. The objectives of the chemical experiments included:

- Determining if CCVD and solvothermal techniques were suitable for simulating processes that may have formed Au-U-C associations in the Witwatersrand Basin,
- Establishing whether uranium-bearing minerals were suitable catalysts/substrates for nanocarbon growth,
- Ascertaining what effects temperature, particle size and uranium concentration had on CCVD product formation,
- Ascertaining the effects that pressure, temperature and a fixed concentration of a gold solution had on solvothermal product formation, and
- Comparing the forms and Raman signatures of the chemically formed products to those of the carbonaceous materials from the Witwatersrand samples.

The results of the geological and chemical investigations were then compared with one another.

1.3 Stratigraphy and Sedimentology

South Africa is host to the Witwatersrand Basin, a Mesoarchean Basin spanning some 300 km across Gauteng, Mpumalanga, the North-West Province and the Free State (Smith and Minter, 1980; Phillips, 2011). First discovered in 1886 by George Harrison on a farm near what is now Johannesburg, the Witwatersrand Basin is the single largest source of gold on Earth (McCarthy, 2009). Initially the gold was mined from quartz pebble conglomerates in the Johannesburg area. Later exploration allowed for the expansion to the east and west, forming the "Golden Arc" (Frimmel and Minter, 2002). The Witwatersrand Basin is approximately 7 km thick and was deposited between 3074 and 2714 Ma (Robb *et al*., 1991; Koglin *et al*., 2010b). Age data for the Witwatersrand Basin is well constrained from U-Pb isotope data obtained from zircons (Armstrong *et al*., 1991; Koglin *et al*., 2010b). Zircon data and metamorphic minerals also constrain the timeline for the formation and subsequent alteration of the Basin (see 1.6). The

Witwatersrand Basin is composed of dominantly siliciclastic sediments: quartzite, shale and conglomerate, interlayered with minor volcanics (Young, 1917; Smith and Minter, 1980). Figure 1.1 shows the extent of the Basin and the location of the major gold fields.

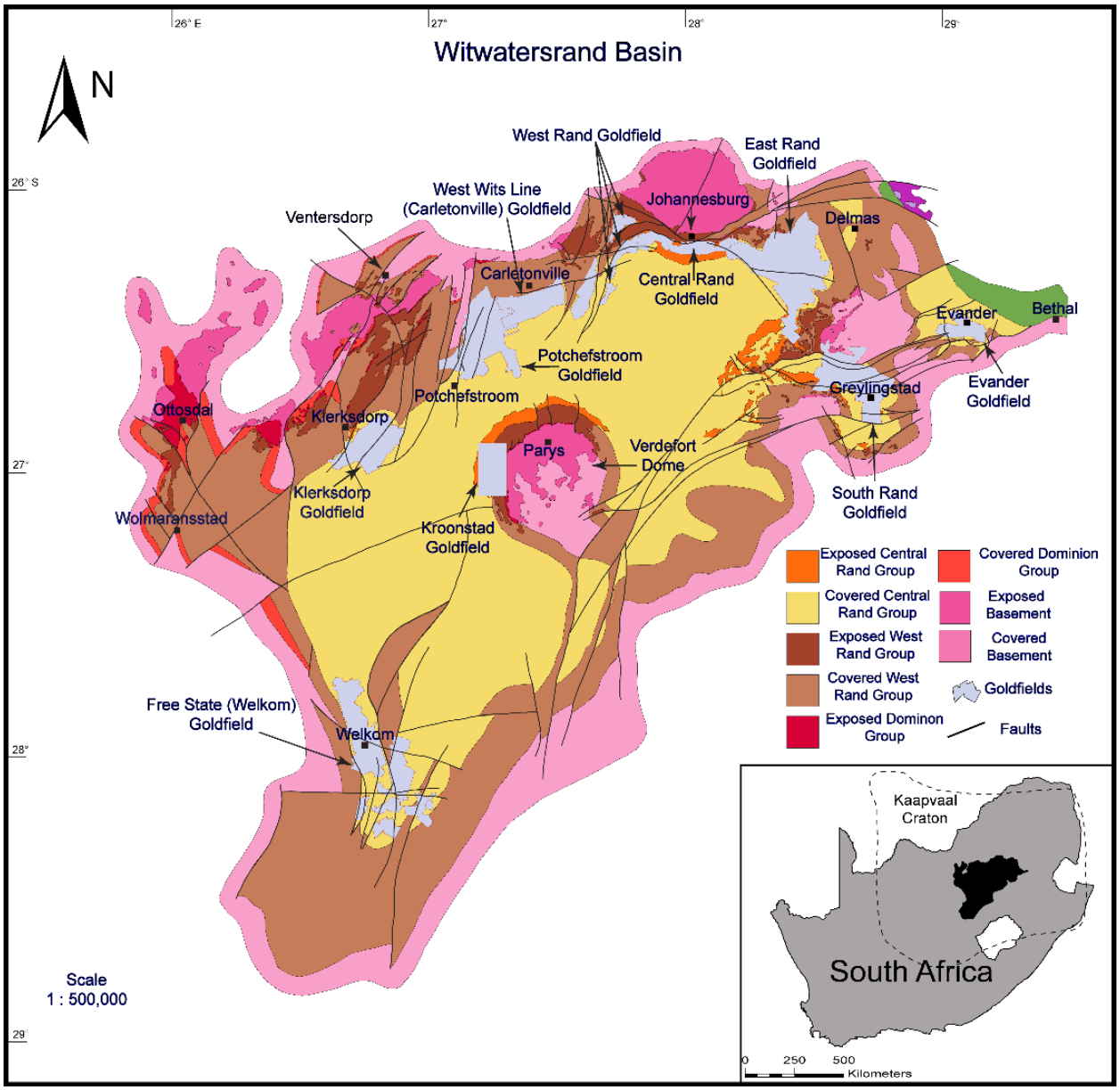


Figure 1.1 Geological Map of the Witwatersrand Basin in South Africa
Showing the outline of the Basin, the major Groups and gold fields relative to the Kaapvaal Craton in South Africa (Modified after Pretorius *et al*., 1986)

The Witwatersrand Basin is underlain by the Kaapvaal Craton, including Archean granites and greenstones, as well as the Dominion Group sediments (McCarthy, 2009). The volcano-sedimentary sequence that comprises the Witwatersrand Basin is the erosional remnant of

sediments deposited into two different tectonic environments – an extensional basin and a foreland basin (Stanistreet and McCarthy, 1991; Robb *et al*., 1997). Figure 1.2 shows the stratigraphy of the Witwatersrand Basin including the reefs and ages thereof.

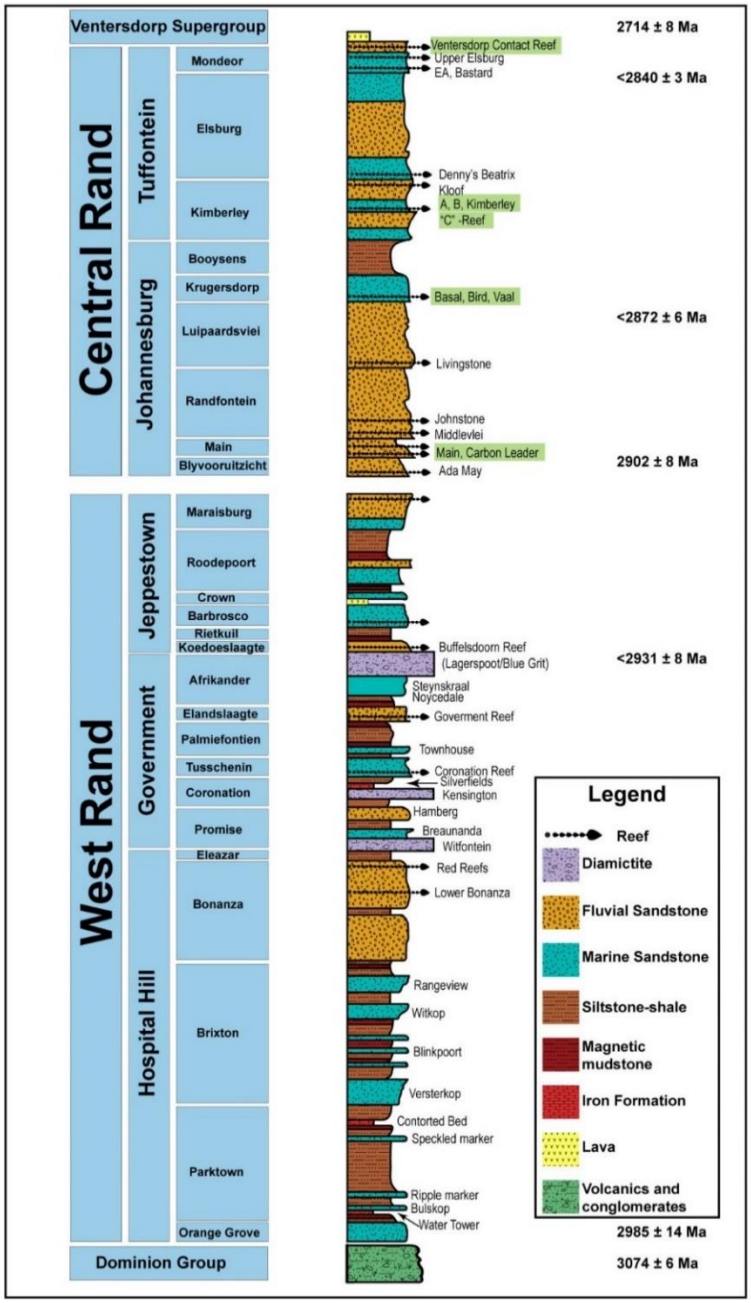


Figure 1.2 Stratigraphic Column of the Witwatersrand Basin
Showing the major stratigraphic subdivisions, the ages of certain markers, the dominant lithology of Formations and the positions of the most important reefs (reefs sampled in this research highlighted green). There are variations in nomenclature between gold fields, after Frimmel and Minter (2002).

Stratigraphically the Witwatersrand Basin is divided into the Central Rand Group (CRG) and the West Rand Group (WRG), based on depositional environment (SACS, 1980).The West Rand Group comprises the sediments deposited into an extensional basin in a shallow inland sea (Stanistreet and McCarthy, 1991; Robb *et al*., 1997) after which the Central Rand Group was deposited onto a foreland basin overlying the West Rand Group (Mellor and Banks, 1916). Sedimentation of the Witwatersrand Basin was terminated by the extrusion of the Ventersdorp Supergroup flood basalts (Van der Westhuizen *et al*., 1991; Hall *et al*., 1997). Following this, the Transvaal Supergroup was deposited onto the Witwatersrand Supergroup to the North after which the Bushveld Complex intruded the Transvaal Supergroup at approximately 2054 Ma (Zeh *et al*., 2015). The Vredefort impact structure was formed when a meteorite struck the Basin close to the centre approximately 2020 Ma (Reimold and Gibson, 1996). Recent tectonic events are not thought to have affected the Witwatersrand Basin in any significant manner (Robb *et al*., 1997)

1.4 Gold fields

Gold has been mined from 8 gold fields across the Witwatersrand Basin (McCarthy, 2009), shown in Figure 1.1. Mining started in the Central Rand Gold field and focussed on the Main Reef, Main Reef Leader and South Reefs (Young, 1917). The Central Rand Gold field continues west to a fault system called the Witpoortjie Gap (McCarthy, 2009). Exploration further west of this break in mineralisation revealed the West Rand Gold field (McCarthy, 2009). Further west the “West Wits Line” is located, comprising the Potchefstroom and Carletonville Gold fields. The last gold field discovered was south west of the “West Wits Line”, where the Klerksdorp Gold field is located (McCarthy, 2009). Further south the Welkom Gold field also yielded significant gold production. East of the Central Rand Gold field the East Rand, Evander and South Rand Gold fields also produced significant amounts of gold. Mining of these gold fields focussed on the Central Rand Group, which contained higher concentrations of gold than the West Rand Group (Phillips and Law, 1994). Naming of economic reefs varies between gold fields (SACS, 1980). The concentrations of gold also vary in the reefs between gold fields, some reefs contain less gold and were uneconomic to mine. Large portions of gold in the Witwatersrand Basin have been

mined out, however significant operations continue in Klerksdorp and Carletonville (Smith and Minter, 1980). The result of the great proliferation of gold from the basin means that current mining operations must run at depths of up to 4 km and at great expense (Anglogold Ashanti, 2015). Mining operations are greatly affected by diminishing grades, intrusive bodies and structure.

1.5 Metamorphism

The key to the debate surrounding the Witwatersrand mineralisation controversy is the metamorphism of the Basin. The entire Witwatersrand Basin is seen to have undergone regional metamorphism to greenschist facies. Metamorphic conditions have been constrained by silicate mineral assemblages to approximately 300°C – 350°C and 150,000 – 300,000 kPa. Common silicate minerals that formed due to metamorphism include: pyrophyllite, chloritoid, chlorite, muscovite, remobilised quartz and sericite (Phillips and Law, 2000; Rasmussen *et al*., 2007). Other metamorphic minerals are rarer, these include andalusite, kyanite, garnet and cordierite and these also indicate higher localised temperatures (Phillips and Law, 1994). Localised high temperature metamorphism was associated with granulites close to the Vredefort Dome, where temperatures could have been up to 700°C (Phillips and Law, 1994). Therefore, metamorphic temperatures associated with silicate minerals are well constrained and indicate the average temperature and pressures across the Witwatersrand Basin. Metamorphism in the Witwatersrand Basin is largely attributed to post-deposition burial, extrusion of the Ventersdorp Supergroup and emplacement of the Bushveld Complex about 100 km to the North at approximately 2054 Ma (Phillips and Law, 1994; Robb *et al*., 1997; Rasmussen *et al*., 2007; Phillips and Powell, 2011; Zeh *et al*., 2015).

However it should be noted that there are cases for higher temperatures that are more widespread in the Basin. Fluid inclusion studies found both gold and hydrocarbons in inclusions from quartz veins (Drennan *et al*., 1999). Additional pressure and temperature conditions were obtained from extensive fluid inclusion investigations. Hydrocarbon rich fluid inclusions indicated that temperatures could have been as much as 500°C during fluid remobilisation in quartz veins

(Drennan *et al*., 1999). Cubic-striated pyrite occurs in reefs throughout the Witwatersrand Basin, research shows that these striations are related to temperature can only form in conditions where temperature is higher than 350°C (Murowchick and Barnes, 1987; Drennan and Robb, 2006). Therefore, a framework is provided for fluid remobilisation of minerals at temperatures of 350°C on average across the Basin, with higher localised temperatures of up to 500°C from fluid inclusions and 700°C for granulites near the Vredefort Dome. Thus, experimental work can be constrained by metamorphic temperatures within the Witwatersrand Basin.

1.6 Structure and Tectonics

Post deposition structure events are recognised as an important feature of the Witwatersrand Basin (Jolley *et al*., 2007; Dankert and Hein, 2010). Folding and faulting affect the Basin, especially in the northwest in the Klerksdorp Gold field (Catuneanu and Biddulph, 2001). Normal faulting, reverse faulting and folding are related to compression, sagging of the Basin and post-depositional events (Dankert and Hein, 2010). Numerous studies point to multiple faulting and folding events related to tectonics. Various researchers have pointed to a number of time periods in which the Witwatersrand Basin was actively deformed (McCarthy, 2009). These events can be classified into 3 broad deformation events:

i) Syndepositional deformation (2840 – 2902 Ma): resulted during fluvial deposition of the CRG due to compression, this formed thrust faults that affected sedimentation.
ii) Middle Ventersdorp Age deformation: as the compressional forces abated, the region relaxed and faults were reactivated as normal faults. Additionally, new faults that allowed for the Platberg Group to be deposited in depressions after extrusion of the Klipriviersberg Group (Stanistreet and McCarthy, 1991; Dankert and Hein, 2010)
iii) Post Transvaal Age deformation: most notably affected by the emplacement of the Vredefort Impact event (Reimold and Gibson, 1996). The deformation is seen as a central dome within the centre of the Basin, with a number of faults forming along with the structure. These faults are also seen as bedding-parallel thrust faulting in the gold fields.

Faults also contain evidence of gold and other mineral remobilisation (Jolley *et al*., 2004). The occurrence of gold in these faults has led to the theory that gold, uranium, carbonaceous matter and other minerals could have been remobilised in fault systems (England *et al*., 2002; Jolley *et*

al., 2004). While the extent of remobilisation has been questioned, there is evidence for both small-scale and regional remobilisation of minerals (Robb *et al*., 1997; Jolley *et al*., 2004). However modern high-resolution seismic techniques provide evidence of wide-scale faulting, especially in the VCR (Manzi *et al*., 2012b; Manzi *et al*., 2013). Seismic techniques also provide evidence of water and methane movement along faults in modern mines, further enhancing the view that faults in the Witwatersrand Basin provide extensive conduits for fluid movement (Manzi *et al*., 2012a).

1.7 Mineralisation

1.7.1 Gold

The gold mines use meta-sedimentary structures to guide operations (Catuneanu and Biddulph, 2001). Gold grades within the Basin vary between very low concentrations in uneconomic reefs to approximately 4 – 12 g/t on average for the economic reefs (Feather and Koen, 1975; Minter, 1976; Frimmel and Minter, 2002), with highest grades of up 100 g/t found for the Carbon Leader Reef (Anglogold Ashanti, 2015). The form of the gold is the result of both sedimentary (detrital) processes and post-depositional hydrothermal processes. Gold occurs as rounded-abraded toroidal micro-particles as well as interstitial crystalline particles (Minter *et al*., 1993; Minter, 1999). Particulate gold is very small in size and ranges between 0.04 and 0.5 mm, although some larger forms can be found, however, these are rare (Minter *et al*., 1993). Minter *et al.* (1993) dissolved the silicates from a sample and reported that only 25% of gold extracted from the sedimentary fore-sets of the Basal Reef was hydrothermal. However, these figures are representative of just one exceptional sample, and may not account for mineralisation in all the reefs. Gold also occurs as microcrystalline inclusions in pyrite (Agangi *et al*., 2013; Large *et al*., 2013). Significantly gold is found remobilised in veins cross-cutting reefs and disseminated within carbon nodules within veins (Drennan and Robb, 2006; Drennan and Robb, 2015). The remobilisation of gold and the strong association with carbonaceous matter (see 1.7.4) is explored in this research.

1.7.2 Pyrite

Pyrite is a major constituent of the Basin and sulphides can form as much as 3% of the reefs (Feather and Koen, 1975; Large *et al*., 2013). Small amounts of chalcopyrite, arsenopyrite, galena, and other sulphide minerals were found as inclusions in pyrite or discrete mineral phases along with pyrite (Saager, 1981; Maclean and Fleet, 1989). Pyrite is an area of strong research focus within the Witwatersrand Basin. A number of pyrite types have been recognised:

i) Allogenic pyrite, emplaced at the same time as deposition via sedimentary processes (Saager, 1981)
ii) Porous pyrite, which is rounded and strongly correlated with higher grades of gold was postulated to have originated as detrital "mud balls" (Koglin *et al*., 2010a; Agangi *et al*., 2013)
iii) Authigenic pyrite, hydrothermally emplaced or over-printed pyrite grains that were subhedral to euhedral (Large *et al*., 2013).

The pyrites in the Witwatersrand Basin were predominantly allogenic, with approximately 50 to 75% of the pyrites found being rounded allogenic pyrites deposited syngenetically (Saager, 1981). The size of pyrite grains is generally small, around 0.2 mm, although centimetre-scale pyrites have been identified in hydrothermally altered strata (Feather and Koen, 1975; Saager, 1981). Geochemical studies on the detrital pyrites revealed that they may have been derived from Archean greenstones and that authigenic hydrothermal pyrites were derived internally from the Basin (Myers, 1993; Guy *et al*., 2012; Agangi *et al*., 2013). Pyrites also appear to have some influence on mineralisation and require further investigation for their chemical interactions with gold in the Witwatersrand Basin.

1.7.3 Uranium-bearing Phases

Uranium-bearing phases in the Witwatersrand Basin has a bimodal occurrence; primary rounded uraninite grains and secondary remobilised veinlets and fine-grained masses have been described (Feather and Koen, 1975; Smith and Minter, 1980). Primary uraninite was deposited

by fluvial processes, UO_2 with some minor U_3O_8, derived from a granitic Archaean hinterland (Minter, 1976; Pretorius, 1981; Robb *et al*., 1992). Uraninite grains contain small bright specks of galena, which is likely to have formed from the decay of uranium. It is argued that this uraninite has remained largely *in-situ* due to the heavy immobile nature of the ^{235}U isotope (Simpson and Bowles, 1977; Smits, 1984; Minter *et al*., 1988). Uranium is also remobilised into secondary coffinite, leucoxene and brannerite that occurs concentrated as a fine-grained mass or in veinlets within the reefs (Feather and Koen, 1975; Minter *et al*., 1988). Additionally, secondary uranium is found disseminated in carbon nodules from veins (Drennan and Robb, 2006). Therefore, the origin of the detrital uraninite is widely agreed to be from Archean greenstone terranes (Simpson and Bowles, 1977; Smits, 1984; Depiné *et al*., 2013), but it is also known that uranium was later redistributed by post-depositional fluids.

1.7.4 Carbonaceous Matter

The key to the mineralisation appears to be the Au-U-C associations in the Witwatersrand Basin. Across the Basin the highest gold grades are most often associated with high concentrations of carbonaceous matter and uranium (Gray *et al*., 1998). As much as 40% of the gold in the reefs is contained in, or associated with, carbonaceous matter (Smieja-Król *et al*., 2009; Phillips, 2011). Carbon documented in the Witwatersrand Basin occurs as rounded nodules or "flyspecks" along reef horizons, where multiple nodules occur in close proximity they can be stratified and the largest portions of carbon form thick friable seams ranging from a few millimetres up to 30 cm in thickness (England *et al*., 2002). Figure 1.3 shows the form of flyspeck and seam carbon. Where the carbon seams are well-developed they have large spindles with fibrous morphology that taper inwards and occur perpendicular to the bedding. The carbonaceous materials in these seams contain rounded fractured uraninite grains that are fragmented and completely surrounded by carbonaceous matter (Smits, 1984; Drennan and Robb, 2006). Drennan and Robb (2006) found that carbon nodules were common in veins as remobilised inclusions and coatings that contained significant amounts of disseminated Fe, U and Au. Drennan and Robb (2006) also noted that numerous phases of hydrocarbon could be seen cutting previously emplaced

carbonaceous matter. The forms of carbonaceous matter are well known, however the origin of the carbonaceous matter has been hotly debated (Hallbauer, 1975; Mossman *et al*., 2008; Smieja-Król *et al*., 2009)

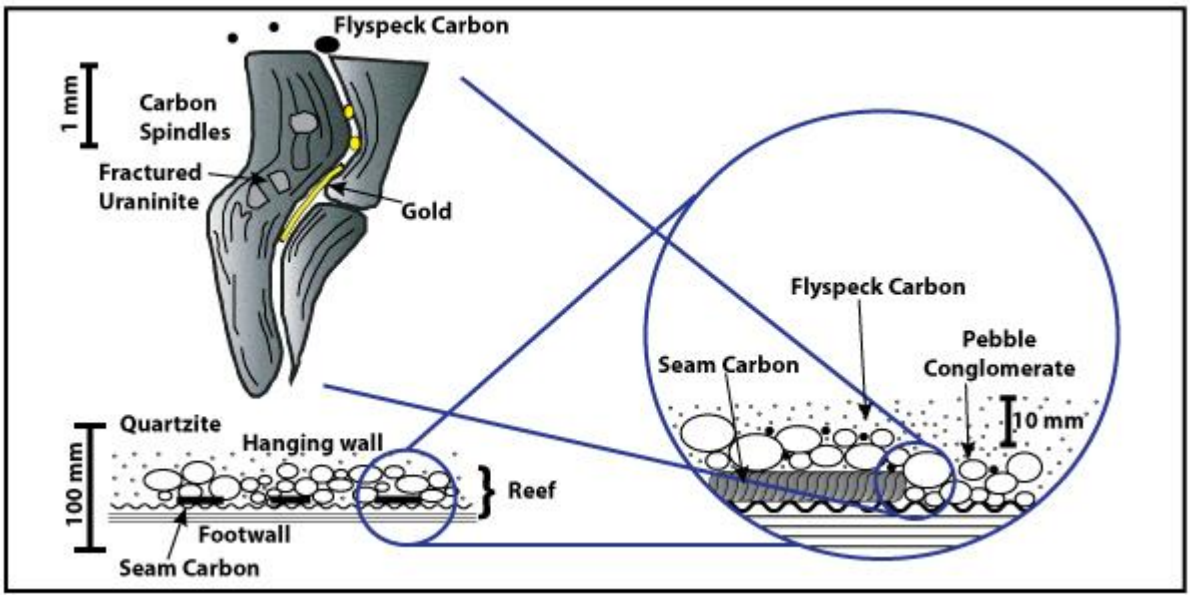


Figure 1.3 Schematic Diagram showing the form of Carbonaceous Matter
Schematic diagram showing the typical distribution of carbon in gold reefs within the Witwatersrand Basin. Modified after Gray *et al.* (1998).

The origin of the carbonaceous matter has been determined using carbon isotope data that points to a biogenic origin of the carbonaceous material from cyanobacteria within the Witwatersrand Basin (Zumberge *et al*., 1978; Spangenberg and Frimmel, 2001). The biogenic nature of the Witwatersrand carbonaceous matter gained support after (Hallbauer, 1975) published electron microscope images of forms that purportedly represented the remains of organic matter. Similar forms were reported by (Smieja-Król *et al*., 2009). The organic matter was viewed as algal mats that could have acted as traps for heavy minerals, including gold, in a sedimentary setting (Hallbauer, 1975; Mossman *et al*., 2008). However, textural evidence from the carbon seams and nodules contradicts a syndepositional model for formation. The occurrences of carbonaceous matter in hydrothermal cross cutting quartz veins (Drennan and Robb, 2006), aromaticity of the hydrocarbons (Schidlowski, 1981), reflectance values (Gray *et al*., 1998), oil entrapment in fluid inclusions in quartz grains (Drennan *et al*., 1999; England *et al*.,

2002) and pervasive distribution of Au and U throughout carbonaceous materials yet lack of other heavy detrital minerals (Drennan and Robb, 2006; Fuchs *et al*., 2016a) are just some lines of evidence that contradict a strictly syndepositional model of formation.

Instead a model was proposed that favoured Archean oil migration and then precipitation via radiolytic polymerisation around uraninite grains (Schidlowski, 1981; England *et al*., 2002). Furthermore, the isotope data and rare earth element (REE) signatures indicate that the carbonaceous matter could have been derived from the lower shale units within the Witwatersrand Basin (Spangenberg and Frimmel, 2001; Fuchs *et al*., 2016b). The significance of fluid movement in the Witwatersrand Basin is examined further in Section 1.9. Although evidence exists for post burial migration of oil (and gold), the model requires further investigation.

Consequently, the terms used for carbonaceous matter in the Witwatersrand Basin have implications for its formation. The technical terms for naming carbon in the Witwatersrand Basin are:

1. "kerogen" for remnant sedimentary organic material of algal origin,
2. "bitumen" for solid or viscous residues of migrated hydrocarbons that are generally poorly soluble in organic solvents, or
3. "hydrocarbons" which are associated with dynamic processes that led to formation of carbonaceous materials (Drennan and Robb, 2006; Mossman *et al*., 2008). Drennan and Robb (2006), proposed that almost all of the carbonaceous matter had been remobilised and that any "kerogen" that remained was indistinguishable from the remobilised "bitumen".

Therefore 'carbon' from the Witwatersrand Basin investigated in this thesis is simply referred to as 'carbonaceous materials', 'hydrocarbon' or by its form i.e. carbon seams and carbon nodules.

1.7.5 Other Minerals

The complexity of the Witwatersrand Basin is shown in the wide variety of minerals found in small quantities. The dominantly quartz rich basin contains a number of phyllosilicates formed

by metamorphism (Phillips, 1987). In addition to the silicate minerals, and minerals mentioned above, a number of other minerals can be found: platinum group minerals, rutile, ilmenite, chromite and diamonds. Zircon is also common throughout the reefs and has been used for U-Pb dating studies that constrain the ages of various stratigraphic horizons (e.g. Armstrong *et al*., 1991b; Koglin *et al*., 2010b). Platinoids, occur as 60 µm small rounded grains within the conglomerates (Cousins, 1973). It is suggested that both chemical weathering and sedimentary action was responsible for the morphology of the platinoids. Additionally, the geochemistry of the platinum minerals indicates that the waters at the time of deposition were very saline (Cousins, 1973; Feather, 1976). The oxides preserved in the Witwatersrand Basin include: rutile, chromite, ilmenite and zircon (Feather and Koen, 1975; Tucker, 1980). These oxides have a detrital form (Feather and Koen, 1975), although research has found small remobilised forms within remobilised silicate materials (Phillips and Law, 1994; Fuchs *et al*., 2016a). Diamonds are also relatively abundant in the reefs, especially within the East Rand Gold field (Feather and Koen, 1975). Diamonds in the Witwatersrand Basin are clearly the result of placer emplacement (Feather and Koen, 1975). The isotopic signature has led to insights into the early plate tectonics of the Earth, indicating that modern tectonics operated as early as 3.5 Ga (Smart *et al*., 2016). It is therefore argued that the processes associated with modern tectonics may also have been operating at the time of the formation of the Witwatersrand Basin, even if atmospheric conditions were not the same (Heinrich, 2015).

1.8 Mineralisation Models and Phases

Mineralisation is the key field of interest surrounding the Witwatersrand Basin currently. Most recent research focuses on the formation of the prominent minerals in the Witwatersrand Basin e.g. Frimmel and Hennigh (2015), Fuchs *et al.,* (2016a) and Heinrich (2015). However, controversy still surrounds the genesis of many minerals present. There are 3 major models used to describe the origin or formation of the Witwatersrand mineralisation that have been proposed and reviewed through extensive research over the years.

The first model proposed by Mellor (1917) the ***placer model*** postulated that the sediments and economic minerals in the Witwatersrand Basin were deposited by rivers. Fluvial action in the placer model was responsible for the distribution and concentration of gold, uranium and pyrite together with pebble lags. Evidence supported this model in many ways, as the shape of the economic minerals, as well as their distribution, was usually correlated with sedimentary structures (Smith and Minter, 1980; Smits, 1984; Minter *et al*., 1988; Minter *et al*., 1993).

Researchers also noted from an early stage that that numerous economic minerals displayed evidence of hydrothermal emplacement or remobilisation (Graton, 1930; Davidson, 1953). In order to satiate these findings an alternative ***hydrothermal model*** was developed, which postulated that only a small amount of gold was emplaced by sedimentary processes and that the bulk of the gold was brought in by hydrothermal fluids from some unknown source outside the basin (Phillips, 1987; Barnicoat *et al*., 1997; Jolley *et al*., 2004; Phillips and Powell, 2011). While this model does provide some explanation for the strong hydrothermal signature of many economic minerals, it does not reconcile why the gold has such a strong sedimentary control (Frimmel *et al*., 1999; Minter, 1999). It also does not explain the age of the gold that was dated at ~3.3Ga (Kirk *et al*., 2001).

Researchers today favour a model that satisfies components of both the "placer" and "hydrothermal" models. The ***modified placer model*** (Robb *et al*., 1997; Drennan *et al*., 1999; Stewart *et al*., 2004) agrees that the gold, uranium, pyrite and other minerals were washed into the Basin by fluvial processes, however, these minerals were later remobilised in hydrothermal fluids (Jolley *et al*., 2004; Hayward *et al*., 2005; Simanovich, 2009; Horscroft *et al*., 2011). This model favours multiple pulses of fluid movement and accounts for many of the mineralisation features, however a number of questions still persist (Phillips and Powell, 2011; Mathur *et al*., 2013).

Researchers cite numerous factors such as anomalous concentrations of gold, source material of the gold, the unique Au-U-C structures, the lack of sizeable gold nuggets and the chemical variations of pyrite as problems with current models for mineralisation (Horscroft *et al*., 2011; Agangi *et al*., 2015). In addition to the three major schools of thought, recent research has

provided an alternate model for the formation of the Witwatersrand Basin (Frimmel and Hennigh, 2015; Heinrich, 2015). They hypothesise that gold may have been dissolved from the land surface by highly acidic, meteoric waters and transported in solution into the Basin. Once in the Basin, gold from solution could have been precipitated near biogenic forms that released free oxygen into the Witwatersrand sediments, altering the oxidation state (Frimmel and Hennigh, 2015; Heinrich, 2015). However, there are shortcomings with this view as it does not explain why carbonaceous materials seen in the basin are discontinuous, contain significant amounts of REE, multiple phases of carbonaceous materials and are intimately associated with uranium bearing phases.

1.9 Importance of Fluids

Fluids are essential to understanding the extent of remobilisation in the Witwatersrand Basin carbon (Drennan *et al*., 1999; Parnell, 1999; Safonov and Prokof'ev, 2006). Fluid inclusion studies have found that at least 4 fluid systems exist within the Witwatersrand Basin: H_2O-CO_2, H_2O-CH_4-CO_2, CH_4-N_2 rich fluids as well as aqueous fluids (Drennan *et al*., 1999). These systems are important as it was found that remobilised gold occurs within the faults and veins that host the fluid inclusions as well as in the carbon nodules extracted from the hydrocarbon-rich fluid inclusions (Drennan *et al*., 1999). The preservation of hydrocarbons in fluid inclusions led Drennan *et al.* (1999a) and England *et al.* (2002) to conclude that 'oil' (or fluid hydrocarbons) migration was a strong factor in the Witwatersrand Basin and had the potential to transport large concentrations of gold (see sections 1.7.4 and 1.8). The close relationship of carbon to uranium provides an insight as to how the Au-U-C associations may have formed. Schidlowski (1981) proposed that the radiation from detrital uraninite caused liquid hydrocarbons to radiolytically polymerise and form solid carbon that encapsulated rounded uraninite phases. Continued precipitation resulted in fracturing and displacement of these rounded uraninite grains into smaller, angular fragments, separated by interstitial hydrocarbon (Landais *et al*., 1990; Drennan and Robb, 2006; Drennan and Robb, 2015).

Therefore many authors agree that there has been remobilisation of carbon, gold, pyrite and silicate materials (Frimmel and Gartz, 1997; Frimmel and Minter, 2002; Koglin *et al.*, 2010 . However, the scale of the remobilisation in the Witwatersrand Basin is contested. Gartz and Frimmel (1999) and Meier *et al.* (2009) state that remobilisation occurred on a millimetre to centimetre-scale and did not play a large role in redistributing minerals after deposition. In contrast, Jolley *et al.* (2004) and Parnell (1999) and Drennan (thesis) provide evidence of remobilisation in the order of metres to hundreds of metres along faults and parallel to bedding, that resulted in wide spread redistribution of minerals and metals in the Witwatersrand Basin.

Therefore, additional consideration should be given to the products that are generated from the thermal degradation of sedimentary algal matter (Type I kerogens). Typically, Type I kerogens are comprised of hydrocarbons (C atoms bonded to H atoms) and other atoms that are grouped with nitrogen, sulphur and oxygen (Pepper and Corvit, 1995). A summary of the generation of hydrocarbons is shown in Figure 1.4.

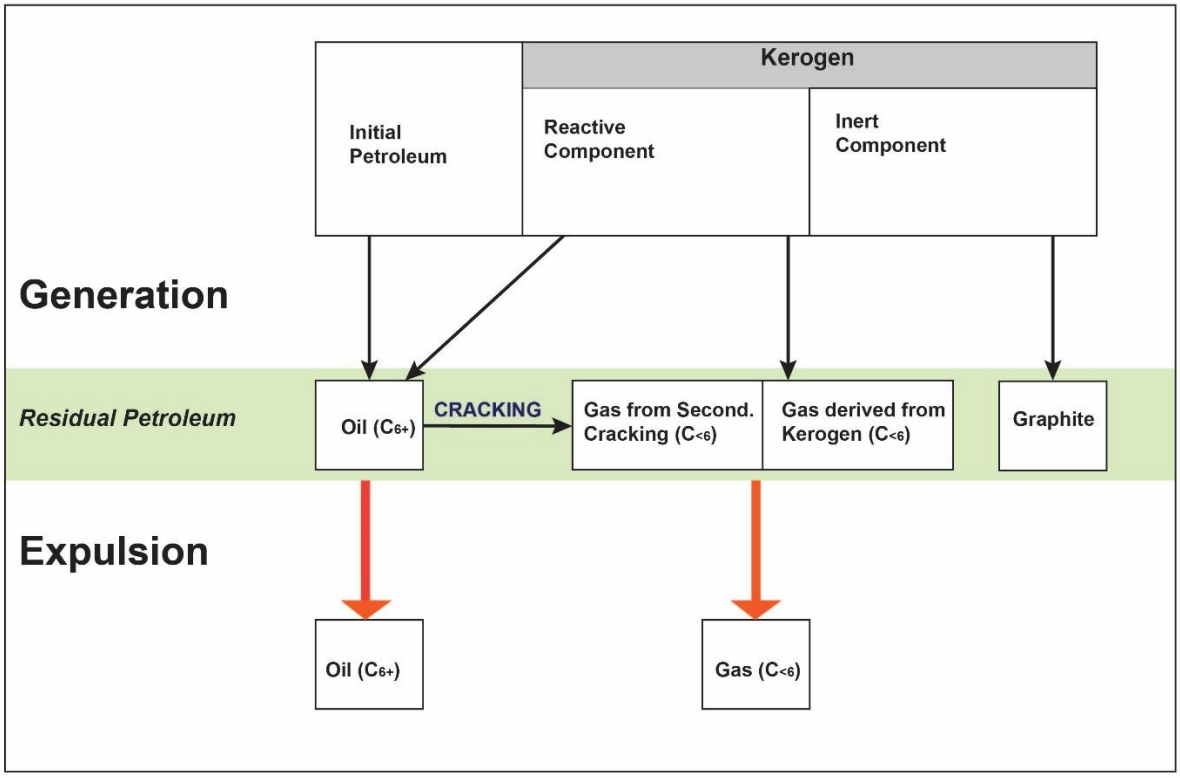


Figure 1.4 Schematic Diagram of Petroleum Generation
The degradation of Type I kerogens as shown by kinetic models (after, Pepper and Corvit, 1995). Of particular interest to this research is the generation of residual petroleum that includes various oils and gasses.

When organic matter degrades it produces oils and gases (petroleum) from the original matter that is comprised of hydrocarbons and NSO compounds (compounds of nitrogen, sulphur and oxygen that incorporate carbon and hydrogen bonded as complex molecules). Additionally, the resulting product also contains resins and asphaltenes (fragments of the original matter) and non-hydrocarbon gases – N_2, H_2S and CO_2 (Pepper and Corvit, 1995). The products generated by the decomposition of complex hydrocarbons with high molecular weight into simpler hydrocarbons is further subdivided. The resulting hydrocarbons can either be a 'gas' if the hydrocarbon has 1 to 5 carbon atoms, or an 'oil' if the hydrocarbon has 6 or more carbon atoms (England *et al*., 1987). A significant portion of the hydrocarbons formed from the pyrolysis of kerogens is also derived from the secondary cracking of the NSO compounds. The residual petroleum formed from the decomposition of sedimentary organic matter thus contains various liquid and gaseous components. The likely hydrocarbon composition of petroleum derived from Type I kerogens is well constrained. England *et al*. (1987) showed the typical composition of an average petroleum reservoir (Table 1.1).

Table 1.1 Typical hydrocarbon composition of a subsurface petroleum from the Bruce Oil Field (After England et al., 1987)

Components	Subsurface Petroleum Liquid (wt. %)	Subsurface Petroleum Liquid (mol %)	Components	Subsurface Petroleum Liquid (wt. %)	Subsurface Petroleum Liquid (mol %)
CO_2	1.1	1.9	C_{16}	2.6	0.8
N_2	0.1	0.3	C_{17}	2.3	0.7
C_1	10.9	49.9	C_{18}	1.9	0.5
C_2	3.3	8.1	C_{19}	1.4	0.4
C_3	3.4	5.8	C_{20}	0.9	0.2
C_4	3	3.8	C_{21}	0.9	0.2
C_5	2.5	2.5	C_{22}	0.7	0.2
C_6	2.8	2.3	C_{23}	0.4	0.09
C_7	4.8	3.5	C_{24}	0.3	0.06
C_8	6.3	4	C_{25}	0.2	0.04
C_9	5.1	2.9	C_{26}	0.1	0.02
C_10	3.7	1.9	C_{27}	0.1	0.02
C_{11}	3	1.4	C_{28}	0.07	0.01
C_{12}	2.9	1.2	C_{29}	0.04	0.007
C_{13}	2.9	1.1	C_{30}	0.02	0.003
C_{14}	3	1.1	Others	26.57	4.2
C_{15}	2.7	0.9	**Total**	**100**	**100**

In a typical mature petroleum most of the hydrocarbons contain 10 or fewer carbon atoms and most of the more complex hydrocarbons still only contained 22 or fewer carbon atoms (England *et al*., 1987). Therefore, research provides a framework for the decomposition of sedimentary algal matter into residual petroleum that can be used to guide experimental parameters for the hydrocarbon source used in this research.

1.10 Metal solubility in Oils and Brines

Hydrocarbons could have represented a significant medium for the transportation of metals within the Witwatersrand Basin. However, in order for experiments to simulate some of the potential processes, an examination of metal solubility in oils was required. Transport of elements in oils and brines is well documented in modern oilfields (Collins, 1975; Filby, 1994). Currently there is strong focus on metal transport within oils and brines in hydrothermal systems (Williams-Jones *et al*., 2009; Seward *et al*., 2013). Numerous metals have been detected in crude oils, these include: V, Ni, Cr, Mn, As, Hg, U and Fe among others (Shah and Filby, 1970). There were also a number of metals that were found in oilfield brines, these include: Ca, Mg, K and Sr amongst others (Kharaka *et al*., 1987). The temperatures for metal transport both oils and brines in modern analogues were within the ranges estimated for the Witwatersrand Basin - ~100°C in crude oils, and ~300°C in active hydrothermal systems (Seward *et al*., 2013). Table 1.2 lists some common elements found in crude oils in addition to the metals that are found in oils. Gold has also been detected in crude oils. Shah and Filby (1970) found trace gold concentrations between 1 and 3 ppb. These concentrations do appear low, but this is to be expected as solubility for gold in crude oils was found to be 2 to 3 ppb at 100°C but as much as 50 ppb at higher temperatures - 250°C (Zezin *et al*., 2007; Williams-Jones *et al*., 2009). These fluids, along with the evidence of hydrothermal activity in the Witwatersrand Basin, provide some constraints that could be utilised in experimental design. Therefore, modern fluid-metal solubility gives a suitable indication to the metals and elements that can be dissolved within oils and brines. Given that chemically these elements do have significant interactions with each other as ligands (oils) or complexes (brines), consideration should be given to this form of fluid transport in the context of the Witwatersrand Basin.

Table 1.2 Compositions of various hydrothermal fluids compared to modern day sea water

	Sea Water	**Taupo Geothermal Fluid**	**Mississippi Oilfield Brines**	**Crude Oil**	**Chinese Oil**
Source	**(Seward *et al.*, 2013)**	**(Seward *et al.*, 2013)**	**(Seward *et al.*, 2013)**	**(Shah and Filby, 1970)**	**(Chifang *et al.*, 1991)**
Temperature	2	275	107	-	-
pH	7.8	8.01	5.65	-	-
Na (ppm)	469	1154.697	76.25	-	298.4
K (ppm)	9.8	125.64	17.68	-	-
Ca (ppm)	10.2	0.227	774.34	-	-
Mg (ppm)	52.8	0.004	-	-	-
Mn (ppm)	-	-	1.16	-	6.532
Ni (ppm)	-	-	-	163.11	43.28
Fe(ppm)	-	-	6.19	44.78	64.06
Al (ppm)	-	-	-	-	8.84
Si (ppm)	0.2	19.238	0.71	-	-
Ba (ppb)	0.1	-	1056	-	9.74
Cu (ppm)	-	4.45	0.02	-	-
Cr (ppm)	-	-	-	0.0085	13.46
Co (ppm)	-	-	-	1.71	8.86
Ce (ppm)	-	-	-	-	0.114
Zn (ppm)	-	0.185	222	29.78	30.11
Pb (ppm)	-	0.023	53.2	-	-
Mo (ppm)	-	0.043	-	-	-
Sc (ppb)	-	-	-	1.67	32
V (ppm)	-	-	-	-	1.85
Sn(ppm)	-	0.84	-	-	-
Se (ppm)	-	-	-	0.53	33.24
Cd (ppm)	-	-	0.83	-	-
Ag (ppb)	-	6	-	-	-
Au (ppb)	-	16	-	1.35	-
As (ppb)	-	17	-	2625.6	14
Eu (ppb)	-	-	-	5.03	6
Hg (ppb)	-	-	-	3236.47	-
Hf (ppm)	-	-	-	-	0.038
La (ppm)	-	-	-	-	0.62
U (ppb)	-	-	-	59.57	-
Sb (ppb)	-	0.004	-	55.36	322
Th (ppm)	-	-	-	-	0.008
Cl (ppm)	551.6	613.92	5614.69	-	34
Br (ppm)	0.8	0.45	13.03	-	27.71
F (ppm)	0.1	0	0.04	-	-
B (ppm)	0.4	12.21	8.05	-	-
SO_4 (ppm)	22.4	410.37	0.19	-	-
H_2S (ppm)	-	-	-	-	-
S (ppm)	-	-	-	-	25400
HCO_3 (ppm)	2.9	48.261	-	-	-

1.11 Carbon Nanostructures: Reactions and Applications

Inorganic compounds (such as uraninite) and organic compounds (such as light hydrocarbons) do not bond easily, thus making experiments considerably more complex. Additionally, experimentally precipitated carbonaceous products needed to be highly structured, similar to the Witwatersrand carbonaceous materials. In order to replicate the Au-U-C associations seen in the Witwatersrand Basin, techniques needed to be adapted from other disciplines of science.

Researchers in the field of heterogeneous catalysis have been producing solid carbon nanostructures (CNSs) on metallic surfaces for a number of years (Dupuis, 2005; Coville *et al*., 2011). CNSs in the form of light-weight single and multi-walled nanotubes, nanospheres, nanofibers and other nanoscale structures have been shown to display some extra-ordinary physical properties, including their: super-strength, variable electrical conductivity, thermal conductivity, etc. (Thostenson *et al*., 2001; Magrez *et al*., 2005). The ability of CNSs to impart exceptional properties in composites has made them very interesting to chemists and material scientists (Thostenson *et al*., 2001; Coleman *et al*., 2006; Coville *et al*., 2011; Shaikjee and Coville, 2012).

However, it is the organometallic association that is of importance in this investigation. CNSs have been grown in a reducing environment from a gaseous phase to a solid phase, on the surfaces of nano-dispersed copper, cobalt, nickel and gold (Dupuis, 2005; Zhou *et al*., 2006; Durbach *et al*., 2009; Li *et al*., 2009). Therefore, experiments that use a fluid/gaseous carbon source and create solid structured carbonaceous matter can be adapted to simulate the process of hydrothermal fluids precipitating hydrocarbons onto uraninite grains. The catalytic growth of CNSs onto a uranium-bearing powder is a novel idea. To date it is known that carbon and uranium can bond, however the process requires strong catalysts and high reaction energies (Cramer *et al*., 1984). The interaction between radiation and carbonaceous matter has also been researched. Previous studies showed the effects of ionising radiation, where energised particles were shown to disrupt the growth of CNSs by creating junctions as well as welding CNSs together (Krasheninnikov and Nordlund, 2004; Dupuis, 2005).

1.12 Publications and format of Chapters 2 - 8

This thesis presents the findings that were compiled as chapters and, in certain instances, as manuscripts for publication (Appendix A). The findings of the chapters for publication are in various stages of assessment i.e. in preparation, submitted or under review. Additionally, findings that were supplementary or unpublished are also presented in the thesis and in the Appendices. For this reason the chapters differ from the published/or about to be published materials and have been altered so that they are more suitable for the format of a thesis. Chapter 2 outlines the numerous techniques, methodologies and analytical conditions used in the research. Chapter 3 presents the detailed petrographic study of the Au-U-C associations that were examined. The results from this Chapter guided the remainder of the research by providing samples (for elemental mapping and tomography), features that were further investigated and insights that instructed experimental design. Chapter 4 presents the results of *in-situ* elemental mapping of carbon seams and nodules using PIXE. Chapter 5 presents the results of the CCVD experiments and the characteristics of the experimental products that were compared to that of Witwatersrand carbonaceous materials. Chapter 6 presents the results from the computed tomography scans of the Carbon Leader Reef (CLR) that were compared with the mineralogy of the sample using electron microscopy and traditional petrography.

The results found from the more traditional techniques (Chapter 3, 4 & 6) were used to design a set of experiments that addressed crucial conditions needed to reproduce the Witwatersrand Au-U-C associations. Chapter 7 details the results of the solvothermal experiments and pressure studies on CNS growth. The most striking results that were found from introducing gold into the experimental solutions are also presented in Chapter 7. Each chapter contains a discussion outlining the main findings of the research presented. Finally, in Chapter 8, all of the results are discussed in entirety, where possible implications/future studies are also presented as well as the conclusions of this research.

2 Methodology and Experiment Set Up

2.1 Sampling and Sample Preparation

In order to examine the Au-U-C associations in the Witwatersrand Basin a number of sources were used. Samples were obtained from multiple historical collections as well as gold mines from the Klerksdorp and Carletonville gold field. Table 2.1 shows the locality, number of samples and reefs that samples were obtained from for this study. The gold fields are distributed through the Basin as shown in Figure 1.1.

Table 2.1 Reefs sampled and the locality of the reefs in the Witwatersrand Basin

Reef	**Number of samples**	**Gold Field**
Basal Reef	8 H.S. and 6 T.S.	Welkom
Beisa Reef	2 H.S., 1 T.S. and 4 O.B.	Welkom
"C" Reef	11 H.S., 7 T.S. and 4 O.B.	Carletonville
CLR Reef	10 H.S., 4 T.S. and 1 O.B.	Carletonville
Dominion Reef	2 H.S. and 1 T.S.	Central Rand
Elsburg Reef	1 H.S.	Klerksdorp
Kimberley Reef	1 H.S. and 1 T.S.	East Rand
Main Reef Leader	6 H.S. and 5 T.S.	Central Rand
May Reef	1 H.S. and 1 T.S.	East Rand
Middevlei Reef	2 H.S	West Rand
Rose Reef	2 H.S	East Rand
South Reef	1 H.S. and 1 T.S.	East Rand
Steyn Reef	2 H.S. and 2 T.S.	Welkom
Vaal Reef	10 H.S., 5 T.S. and 3 O.B.	Klerksdorp
VCR	2 H.S. and 2 T.S.	Carletonville

* H.S. – Hand Samples, T.S. – Thin Sections, O.B. – Ore Blocks

From the available samples in the collections detailed in Appendix B, 61 hand samples were examined further and 39 thin sections and 12 polished ore blocks were prepared for the various petrographic studies (Chapters3, 4 and 6). Samples focussed specifically of the reef portion of the economic horizons throughout the CRG where gold mineralisation was more prominent. Samples with the following features were selected:

1. Excellent examples of carbon seams, both thick and thin discontinuous seams
2. Nodular carbon in reefs
3. Samples that lack obvious carbon but have good gold grades

4. Samples with sulphide mineralisation in the reef
5. Samples in contact with faults or veins.

Additional samples were selected for exceptional features that provided insights into the processes that formed them. The complete list of samples and the features of each is shown in Appendix A. The samples obtained for this study are quite unique in that many come from historical collections and would otherwise not be obtainable. Therefore, many of the features seen in these samples have not been properly investigated.

Representative samples were prepared as polished sections and ore blocks. Preparation of these used a hardener containing triethylenetetramine, which was mixed in a 2 to 15 ratio with a resin containing bisphenol-A, epoxy resin, oxirane and mono derivatives. These may contain traces of elements that could be detected by PIXE and EPMA. Additionally, the glass slide onto which the samples are adhered could also contain traces of Cl, As and Cr. This was taken into account during the current investigations.

2.2 Petrographic Microscopy

Thin sections and ore blocks were examined using reflected and transmitted light microscopy on the Olympus BX63 and BX41 optical microscopes. The Olympus BX41 is a typical petrographic microscope with a rotating stage. The BX41 was used to characterise and identify the mineral and textural components, relative concentrations and associations thereof (Chapter 3). The Olympus BX63, housed in the Microscopy and Microanalysis Unit (MMU) at the University of the Witwatersrand is slightly different in that the stage does not rotate, however it is fully mechanised. The BX63 was used to obtain stitched images of each of the prepared samples using Multiple Image Alignment (MIA). With MIA an automated program shifts the stage and each of the images obtained are stitched together to give one complete image of the sample. MIA on the BX63 using 4X magnification, allowed for better and more consistent petrographic studies, while higher magnification images were obtained using the more easily accessible BX41. This method

using the Olympus BX63 and BX41 in conjunction proved highly effective and allowed for a digitised version of each section to be kept.

2.3 Chemical Analyses

Powdered catalyst/uraniferous samples used in Chapter 5 were analysed using X-ray fluorescence (XRF) spectroscopy at the Earth Sciences Laboratory at the University of the Witwatersrand. Major elements were detected by using a fused disk methodology. Each sample powder was heated to 1000°C and loss on ignition (LOI) was calculated, following this the powder was mixed with a chemical flux and heated to 1000°C once more and then finally pressed into a fused disk. The data was collected using a PANalytical PW2404 XRF spectrometer. The trace element analysis was based on a pressed pellet method. A small amount of sample was mixed with polyvinyl alcohol and pressed into a mould; the sample was left to dry out for 24 h. The pressed pellet was then analysed for trace elements using a PANalytical PW2404 XRF spectrometer.

XRF was not used to analyse the reefs sampled for thin sections/ore blocks. In order for whole rock geochemical analyses to be useful the Au data would be required. Gold data is only reliable when obtained from fire assay analysis, however this technique was too expensive for this study. Instead qualitative values were obtained using petrographic methods.

Additional chemical analyses were required to determine the chemical composition of solutions to be determined (Chapters 5 and 7). In order to achieve this Inductively Coupled Plasma Optical Emission Spectroscopy (ICP-OES) was undertaken. The analyses were conducted using a Spectro Genesis Spectrometer with an operator specified method designed to detect As, Sr, Mo, Cu and U. All methods were calibrated using a set of standard solutions before each set of analyses were completed. The quality of the ICP-OES results were compared by using microwave digestion of HILG19 sample. Microwave digestion used a portion of solid material and completely digested it into deionised water. The total amount of U, Sr, Mo, Cu, Au and As was then measured in solution. These values are compared to the XRF data in Appendix H.

2.4 Proton Induced X-ray Emission Analysis

Proton induced X-ray emission (PIXE) micro-mapping of elements found *in-situ* within their host minerals is an underutilised technique in the study of sediment-hosted mineralisation. PIXE is a non-destructive, well-understood and dependable method and should be used to determine the distribution of mobile and immobile elements as they occur in the Witwatersrand Basin.

PIXE has previously been used to map elements within carbon nodules from veins (Drennan and Robb, 2006) and carbon material from the Carbon Leader Reef from the Witwatersrand Supergroup and Black Reef from the Transvaal Supergroup (Fuchs *et al*., 2016a; Fuchs *et al*., 2016b), and has proved useful in these studies. Multiple samples of well-developed seam and nodular carbon were analysed using PIXE. Areas of interest within the samples were those that included Carbon, Uranium and Gold in various proportions in seam carbon, nodular carbon, veinlets cutting through carbon seams, fractured or displaced grains and silicate minerals between carbon spindles. The thin sections and ore blocks that contained features of interest for the PIXE analyses were prepared with a 60 nm layer of carbon coating to prevent charging (Chapter 4).

The analyses were performed using the nuclear microprobe at the Materials Research Department of iThemba LABS, Somerset West, South Africa. The facility used a 6 MV single-ended Van de Graff accelerator and Oxford magnetic quadrupole triplet for beam focusing (Prozesky *et al*., 1995). A proton beam of 3.0 MeV energy and ~500-800 pA current was focused to a 5 x 5 μm^2 spot and raster scanned over selected areas of samples with either a square or rectangular scan pattern of variable sizes (up to 2.5 mm x 2.5 mm scan sizes were possible) and a variable number of pixels (up to 128 x 128). PIXE spectra were registered with a Si (Li) detector (30 mm^2 active area, working distance 24 mm), positioned at a take-off angle of 135°. The effective energy resolution of the PIXE system (for the Mn Kα line) was 155-160 eV, measured for individual spectra. The X-ray energy range was set between 1 and 40 keV. Proton elastic backscattering (EBS) spectra were recorded with an annular Si surface barrier detector (100 µm thick) positioned at an average angle of 176°. Data were acquired in the event-by-event mode. Results were normalised using the integrated beam charge collected from the insulated specimen holder.

Each selected area was measured twice, using two different X-ray absorbers interposed between the sample and PIXE detector. Application of the thicker absorber (100 µm Al) restricted the practical X-ray energy range to above 4 keV (X-rays from the lighter elements were filtered out, and the detection of heavy elements was relatively enhanced). Additional measurements of low-energy X-rays (between 1-4 keV) were made using a 125 µm thick Be absorber. The proton current in this case was ~200-400 pA in order to reduce the number of pileups in the PIXE spectra.

Quantitative results were obtained using a method employing GeoPIXE II software (Ryan, 2000). The calibration of the analytical system was tested by measurements of reference materials - pure elements, pure minerals and USGS (United States Geological Service) standards BIR-1 and BCR-2. Elemental mapping was performed using the Dynamic Analysis method (Ryan and Jamieson, 1993; Ryan *et al.*, 1995; Ryan, 2000), which generates elemental images using series of X-ray lines (in this case K, L or M lines). The maps are (i) overlap-resolved, (ii) with subtracted background and (iii) quantitative, i.e. reported in ppm or wt. % units. Maps were constructed from the 7 analysed areas in the selected 7 samples (Table 2.2) using bitumen matrix compositions from scanned areas.

Table 2.2 Samples selected for PIXE micro-maps

Sample	**Reef**	**Locality**	**Figure**	**PIXE Map**
CREEF01	"C" - Reef	Blyvooruitzicht Gold Mine	Figure 4.1	Figure 4.2
DFN10	CLR	Doornfontein Gold Mine	Figure 4.3	Figure 4.4
LGM3	Basal Reef	Loraine Gold Mine	Figure 4.5	Figure 4.6
MGS6513	Vaal Reef	Hartebeesfontein Gold Mine	Figure 4.7	Figure 4.8
PSGM	Steyn Reef	President Steyn Gold Mine	Figure 4.9	Figure 4.10
VCR	VCR	Western Deeps Gold Mine	Figure 4.11	Figure 4.12
CREEF EM2	"C" – Reef	Blyvooruitzicht Gold Mine	Figure 4.13	Figure 4.14

The EBS maps of carbon distribution were constructed using energy "gates" with background subtraction. In addition, PIXE and EBS spectra were extracted from smaller regions of arbitrarily selected shapes within maps. This selection was made on the basis of element distributions from PIXE maps. PIXE spectra from these regions were fitted using a full nonlinear deconvolution procedure (Ryan *et al*., 1990).

2.5 Electron Probe Micro-Analysis

PIXE micro-maps were supplemented with Electron Probe Micro-Analyses (EPMA). Wavelength-Dispersive Spectrometry (WDS) provided maps of selected elements and their concentrations within Witwatersrand samples. Only a few maps were required, however the different detector types and ability to validate the presence of elements proved useful in supplementing PIXE data (Chapter 4, EPMA data presented in Appendix G).

EPMA was performed using a Cameca SX-5FE electron microprobe equipped with 5 WDS spectrometers housed at the MMU. Analytical conditions used 15 keV acceleration voltage and a beam current of 20 nA. Natural and synthetic standards were used to calibrate the microprobe. A focused electron beam with a 50 ms dwell time was used during quantitative WDS analyses.

2.6 Laser Raman Spectroscopy

Laser Raman spectroscopy (LRS) was used to acquire the spectral signatures of experimental products and of Witwatersrand Carbon materials for comparison (Chapters 5 & 7). Spectra were acquired using the 514.5 nm line of an argon ion laser on a Horiba Jobin-Yvon LabRAM HR Raman spectrometer housed in the MMU at the University of the Witwatersrand. The laser was focused onto the sample via a microscope objective and the backscattered light was dispersed onto a liquid nitrogen cooled CCD detector via a grating with 600 lines/mm. Spectra were processed by removing the background interference.

2.7 Micro-CT scanning

High resolution µCT scans of Witwatersrand Carbon seams have not previously been published even though µCT has successfully been applied in geological investigations of sulphide minerals in ultramafic rocks (Godel *et al*., 2006) and in gold grains in porphyry deposits (Kyle and Ketcham, 2003). Computed tomography uses X-rays passing through a sample that is rotated through 360 degrees to visualise material differences. Materials within the sample attenuate X-rays to

different extents such that dense materials attenuate more than less dense materials. Table 2.3 shows relative densities of a number of materials commonly seen in Witwatersrand Reefs. The notable difference is the specific gravity of hydrocarbons (<2) compared to gold (19.3), which creates sufficient material contrast in the image stack generated by µCT to permit digital separation of the two materials (i.e., segmentation) using VGStudio Max 2.2 (Volume Graphics GmbH).

Table 2.3 Specific gravity of minerals commonly found in Witwatersrand Carbon seams

Mineral	**Specific Gravity** (Cairncross, 2004)
Hydrocarbon	<2
Gold	19.3
Phyllosilicates	2.5 – 3.0
Quartz	2.66
Uraninite	7.5 – 10
Pyrite	5

A high resolution image stack (voxel size = 29 µm) of the CLR sample was generated using a Nikon Metrology XTH 225/320 LC dual source industrial µCT system. The sample was placed on a rotating pedestal, while the X-ray source was fixed. The system is located in the Paleosciences Centre of the University of the Witwatersrand. Scan parameters include: 210 kV, 100 µA, 2000 projections, and 3.6 µm of copper filtration.

Acquired image data were processed using VGStudio Max 2.2 (Volume Graphics, GmbH). Using thresholding, gold was filtered out of the image stack, which was subsequently compared to the petrographic images. A volume of interest representing the 3D distribution of the gold was orientated at various positions in order to examine the 3D form and distribution of the gold (Chapter 6).

2.8 Scanning Electron Microscopy (SEM) and Auto-SEM

After non-destructive µCT analysis (outlined above) the CLR sample was then cut and mounted as a polished ore block in order to correlate the density data of the µCT scan with mineralogical data. The gold distribution from the 3D rendered µCT data was complimented using 2D mineral

mapping Auto-SEM-EDS (scanning electron microscopy with energy dispersive X-ray spectroscopy) technology. For this the sample was coated in 100nm of carbon. A Carl Zeiss Mineralogic® system, comprising an Evo LS15 tungsten filament SEM platform, combined with multiple (in this instance 2) Bruker XFlash® 6|30 EDS detectors, was used throughout analysis. The system is located at the Zeiss offices in Johannesburg. Scans were conducted at 25kV for maximum energy resolution of most elements (up to and including uranium) and a beam current of ~1.3 nA. X-ray mapping was conducted at 8 µm beam stepping intervals across the polished surface. X-ray count rates were calibrated to 500 000 counts per second to a gold standard which was also used as an X-ray identification elemental standard (L-Alpha lines were used). The EDS data was combined into a false-colour mineralogical map, that stitched together 28 fields to create the final map. The system processed and classified the data using the "Mineral Recipe" protocols of Mineralogic® from the Mineralogic Explorer® program, following the protocols of Tonžetić (2015). For the purposes of classifying gold, uranium minerals, pyrite and phyllosilicates in ore blocks and thin sections, SEM-EDS was used to identify minerals (Appendix D), provide textural information and to broadly image experimental products.

2.9 Transmission Electron Microscopy

Transmission Electron Microscopy (TEM) was used to photograph the experimental products that are reported in Chapters 5 and 7, as well as seam carbon material from the Witwatersrand Basin. The FEI Tecnai™ 120kV T12 TEM was used to image the materials. Powdered materials were used for the experimental products, and a small portion of carbon from the Witwatersrand Basin was ground into a powder for comparison. The powdered samples were suspended in methanol and disaggregated using a sonicating bath. A drop or two of the methanol-powder mixture was then placed onto a lacy-carbon, copper TEM grid. Samples were placed into the vacuum chamber of the FEI Tecnai™ TEM and imaged.

2.10 Thermal Analysis

Thermogravimetric analysis (TGA) was used to analyse the products of the CCVD and solvothermal reactions (Chapters 5 and 7). TGA analysis was performed by a Perkin Elmer STA 6000 thermogravimetric analyser. Approximately 10 mg of each sample was placed in a ceramic pan and then placed in the instrument furnace. The temperature of the sample was increased from room temperature to 900°C at 10°C/min under an oxidative atmosphere (air, 50 mL/min).

2.11 Experimental Growth of Carbon Nanostructures (CNSs)

In this study, the catalytic chemical vapour deposition (CCVD) technique was adapted in an attempt to grow carbonaceous materials onto uranium-bearing phases. The uraniferous materials were found in granitic and meta-sedimentary powders were used as the substrate in order to simulate the C-U associations that have been seen in the Witwatersrand Basin. The CCVD process was selected as it provided a cost effective, simple, open-system reaction that is well-known (Section 1.11) and easily repeatable with high levels of accuracy. Although it is obvious that these experiments initially represent different conditions to those in geological settings, the experiments are vital in order to determine whether uranium-bearing minerals are a suitable substrate for hydrocarbon precipitation. Acetylene was selected as the hydrocarbon source as it is very reactive in even slightly reducing conditions, very pure (no other hydrocarbon components) and represents a light gas hydrocarbon that can be derived from the decomposition of Type I kerogens (Section 1.9). The conditions, time, gas flowrates and analytical techniques were selected to minimise the amount of variables involved in the reactions. The objective was to obtain a data set that satisfied good chemical experimental methods and that were applicable within the broadest geological constraints for the Witwatersrand Basin.

Approximately 100 mg of either granitic or meta-sedimentary powders, with U concentrations varying from 420-7900 µg/g (see Table 5.1, Chapters 5), were placed under CCVD conditions, equipment set up is shown in Figure 2.1. Although the chemical composition of each was somewhat similar, the granite powder represented a relatively unaltered source that was similar

to that postulated for the provenance of the Witwatersrand Basin. Due to health and safety concerns, the powders selected were also constrained by the maximum uranium content that was safely allowed for use in the experiments.

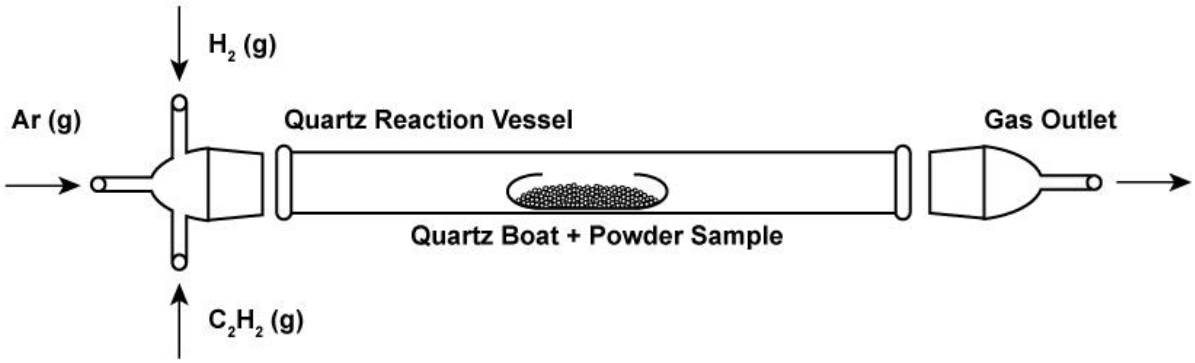


Figure 2.1 CCVD experimental set-up.
The experimental set up in a quartz reaction tube with gas inlets for: H_2, C_2H_2 and Ar and a gas outlet. A quartz boat with 100 mg of powder is loaded into the tube which is sealed and placed into a temperature controlled furnace.

Additionally, the meta-sediment powder represented sediments that were exposed to surface processes, been deposited and then metamorphosed to a low grade. Both source rocks were from Hildenhof Uranium prospect and the Swakop Uranium Mine in Namibia. The powders were sieved into two different size fractions: <32 µm and 32 µm - 75 µm, to establish if the powder size played any role in these reactions.

The CCVD technique used a quartz boat loaded with either meta-sedimentary or granitic powder. The loaded boat was placed into a quartz tube, into which hydrogen (H_2 - a reducing gas), acetylene (C_2H_2 – a carbon source) and argon (the inert carrier gas) were passed. The quartz tube was sealed and heated in a temperature-controlled furnace from room temperature up to reaction temperatures of: 300°C, 450°C and 600°C at 10°C/min for various experiments. During the heating procedure argon was continually passed over the sample. Once the reaction temperature was achieved, hydrogen and then acetylene were introduced and the reaction was run for 2 h for all experiments.

In order to establish if uranium had played any role in these CCVD experiments, powders of both size fractions (i.e. <32 µm and 32 - 75 µm) of HILG19 were used where the uranium had been leeched from them. The aim of leeching the Uranium was to provide a comparative sample with "zero" uranium to determine whether other catalysts play a role in structured nanocarbon growth. A mass of 1 g of each powder size fraction of HILG19 was mixed with 20 mL of a 0.1 M solution of sodium bicarbonate ($NaHCO_3$) and agitated on a shake-table for 6 hours. After leaching each mixture was centrifuged and the resulting powder separated off and dried at 50°C for 12 h. The concentration of U that was leached in each case was quantified using inductively coupled plasma optical emission spectroscopy (ICP-OES). The leached powder was loaded into the quartz reactor and reacted using the same technique as outlined above.

2.12 Solvothermal Experiment Setup

Solvothermal synthesis of carbon is a relatively new technique in material sciences. Solvothermal techniques can produce nanostructured carbon at much lower temperatures than CCVD techniques (Kuang *et al*., 2004). The solvothermal technique was adapted in order to produce materials at lower temperatures and higher pressures in a closed-system with a limited hydrocarbon source to provide a better proxy to conditions postulated for the Witwatersrand Basin at peak metamorphism. Solvothermal experiments come with a unique set of challenges. Although they are able to attain higher pressures than those in the CCVD experiments, pressures are still much lower than those postulated for the Witwatersrand Basin. Solvothermal techniques are not as well-understood and therefore not as widely reported on compared to CCVD techniques, especially with respect to the effects of various carbon and hydrocarbon sources (Deshmukh *et al*., 2010). Therefore, the solvothermal experiments had to be designed to utilise previous research and the data obtained from the CCVD experiments. Research shows that many hydrocarbon sources used in solvothermal reactions are either chemically prepared (and don't represent likely compounds derived from kerogen degradation) or require impossibly high reaction temperatures (e.g. polyethylene at 650°C in Deshmukh *et al*., 2010). Ideally, experiments should use a mixture of hydrocarbons that roughly represent the composition of an oil derived

from type I kerogens. However, experimentally it would not be practical to use a wide variety of hydrocarbons in a solvothermal reaction. Therefore, sucrose was selected as the carbon source. Sucrose is pure, previously researched and requires low temperatures for reactions to take place (Kuang *et al*., 2004). The objective of the solvothermal experiments was to provide details on the effects of pressure, a limited fluid hydrocarbon source and the effects of gold in solution in the formation of experimental Au-U-C materials. In order to apply this technique a custom built autoclave was required. The autoclave, shown in Figure 2.2, was manufactured from solid stainless steel and holes were drilled for valves.

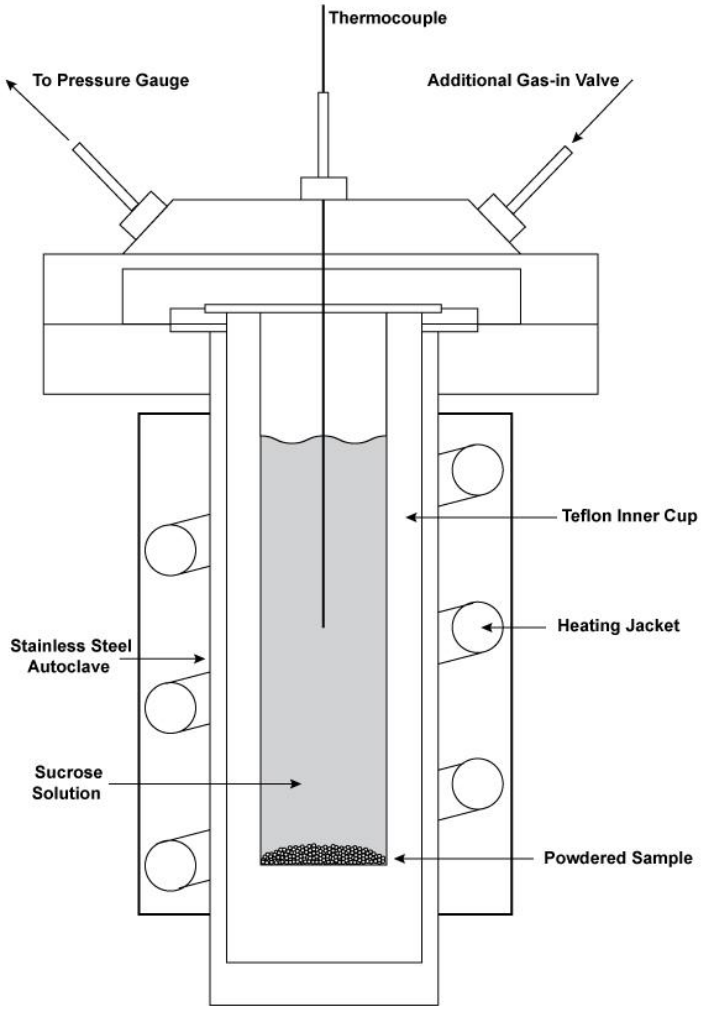


Figure 2.2 Schematic diagram of a solvothermal experimental set-up
Section through the cylindrical autoclave that was purpose built for solvothermal reactions. The body is made from stainless steel, the lid is bolted on to seal the vessel and then heated using a heating jacket.

The valve fittings were welded on and the entire pressure cell was certified up to 300 000 Pa. While this proved useful, it should be noted that welding could provide weak points. Therefore, maximum pressures were limited. However, the manufacturer did suggest that future equipment use Swagelok® fittings which could be fitted without welding them. The valves allowed for a thermocouple, pressure gauge and release/gas input valve on the top of the autoclave. The top of the autoclave contained a small groove for a Teflon ring, this provided the airtight seal that allowed the autoclave to be pressurised to higher pressures than the CCVD equipment. Inside the autoclave a Teflon inner cup was machined with a volume capacity of 100 mL. Experiments involved the use of 100 mg of granitic powders, stirred into an 80 mL solution of 0.05 M sucrose ($C_{12}H_{22}O_{11}$). The solution was prepared with >99.5% sucrose grains dissolved in deionised water at room temperature. The solution was loaded into the Teflon inner cup and the pressure cell was sealed and placed into the heating jacket. The autoclave was heated to reaction temperature 180°C, over 3 h and run for 18 h. After the vessel cooled to room temperature the resulting liquid was drained through filter paper in a Büchner funnel, and any solid product on the walls of the Teflon inner cup was scraped onto the filter paper.

The mass of solid product extracted from the liquid was measured. The filtered liquid was reserved for analysis. Figure 2.2 shows the experiment set up; the autoclave was placed within a fume hood for safety. The temperature, particle size and sucrose concentration were all constant for the solvothermal experiments. Only two uraniferous powder samples were used: <32 µm HILG19 and <32 µm HILG19 granite. The pressure was varied by pumping either 400 or 800 kPa of N_2 gas into the sealed pressure cell at room temperature. Finally, one additional set of experiments were conducted in which a 20 mL solution ~0.1 M aurichloric acid ($HAuCl_4$) was combined with 60 mL of 0.05 M sucrose solution and run at standard temperatures and pressures. The resulting solid products were analysed using TEM, LRS and TGA. The liquid solution filtered off from the product was analysed using ICP-OES, as described previously.

3 Petrographic Study

3.1 Petrography and Variation of Au-U-C Features of Various Witwatersrand Reefs

The 39 thin sections and 12 ore bock samples selected from across the Witwatersrand Basin (see Section 2.1, and Appendix B) display a wide variety of features. These features, and more specifically the Au-U-C associations, are listed in detail for all samples in Appendix C. The results presented in this chapter are a summary of the most important features and textures observed in the full petrographic study shown in Appendix C. Additionally relict uranium minerals and a carbon nodule sample from a vug in a quartz vein required confirmation using SEM and EDS, the results of the analyses are shown in Appendix D. This Chapter supplemented and guided the overall investigation of this thesis. However, this Chapter is not intended for publication at the time that this thesis was submitted as many of the features discussed are already published (e.g. Feather and Koen, 1975; Minter *et al*., 1988), albeit not for all of the reefs sampled in this study. In this section the details and features of the variations in Au-U-C and, to a lesser extent, sulphide minerals are examined.

3.1.1 Uranium-Bearing Phases

Occurrences of uraninite within the samples studied are dominantly rounded and occurred at the base of the reefs. The primary uraninite grains generally range from 20 µm to 200 µm, and can contain brighter specks of galena (Figure 3.2). Many samples do not contain optically identifiable uranium minerals (e.g. MGS4071). Uranium-bearing phases are also seen in samples as brannerite and coffinite, these are certainly secondary phases forming a fine grained interstitial mineral phase between grains of quartz, sulphides and phyllosilicates (Figure 3.1).

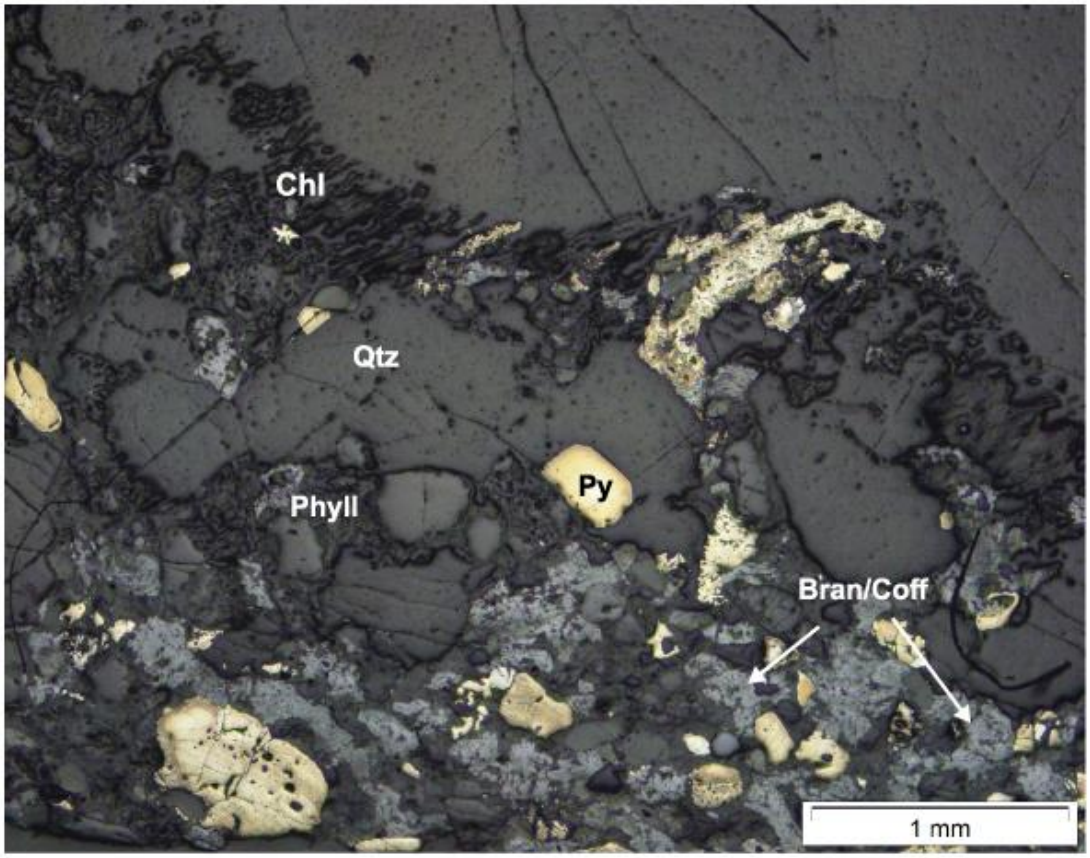


Figure 3.1 Reflected light image of secondary phases of brannerite and coffinite minerals in BDN2
Sample from the Dominion Reef showing secondary uranium phases (Bran/Coff) within a quartz pebble conglomerate (Qtz), the sample contains abundant alteration minerals as a phyllosilicate matrix (Phyll), pyrite grains (Py) and laths of chlorite/chloritoid (Chl) along the edges of a large quartz pebble.

Interestingly, where secondary uranium phases are observed there is not always abundant carbon nodules or seams present (Figure 3.1). However, where carbon is present it tended to be in close proximity to the secondary uranium minerals. Relict grains of uraninite are also common. In relict grains, boundaries of a previously rounded uraninite grain are identified, however the centres are partially replaced by fine grained phyllosilicate minerals (Figure 3.3). The composition of these grains is confirmed using EDS and backscatter SEM images (Appendix D). Both the uraninite and secondary brannerite/coffinite do not contain visible gold within them. Where gold is present, especially in association with brannerite/coffinite, it is invariably associated with pyrite/carbon/phyllosilicates and merely in contact with the uranium-bearing phase. Uraninite in well-developed carbon seams always occurs as rounded grains that are fractured within carbon spindles. Uraninite in these well-developed seams has a “blown-up” or fragmented

configuration, where carbon filled in the fractures and displaced various parts of the grains (Figure 3.2).

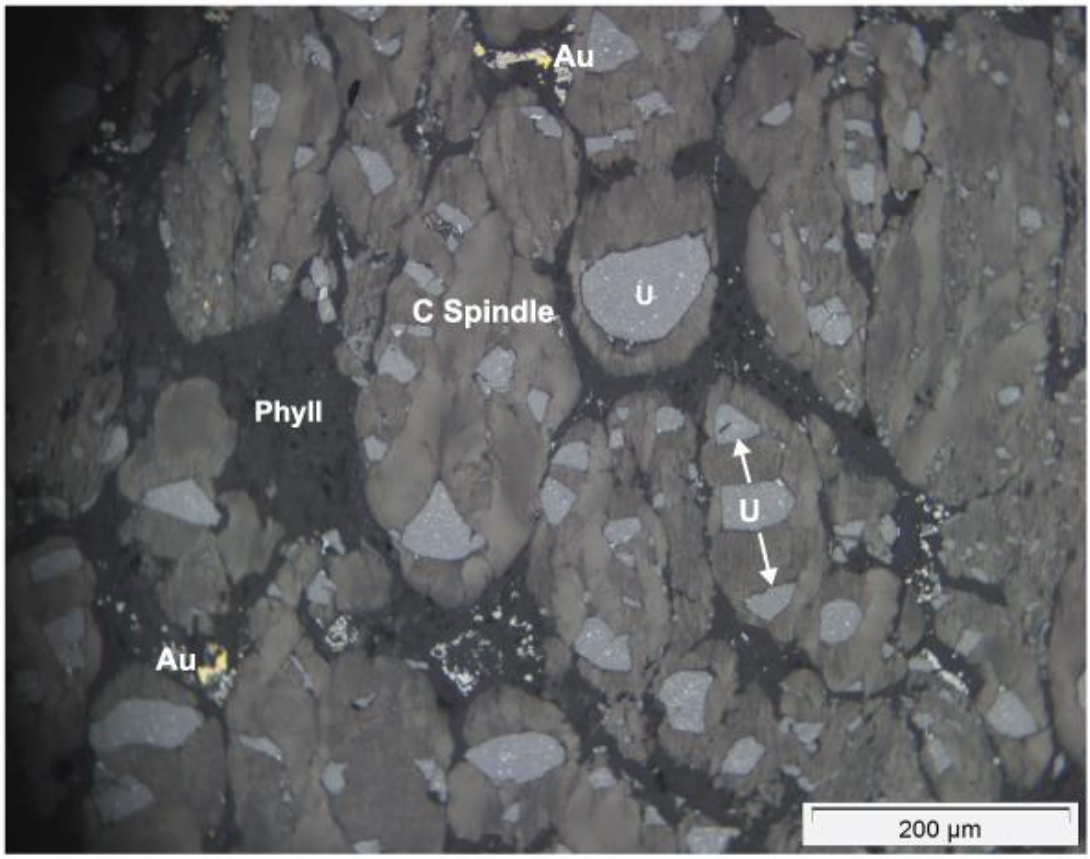


Figure 3.2 Reflected light image of carbon seam spindles containing "blown-up" uraninite in CREEF EM1
Carbon seam sample from the "C" – Reef. Section taken perpendicular to the long axis of the hydrocarbon spindles (C Spindle). Spindles contain uraninite grains (U) displaced by the hydrocarbon with phyllosilicate minerals (Phyll), gold (Au) and silicate between the spindles. The bright white "specks" within the uraninite are galena, and radiogenic halos around uraninite are seen within the hydrocarbon material.

Uraninite grains also has halos around them in the carbon where the radiogenic nature of uraninite caused apparent bleaching of the carbon, but this is not seen to have an effect on any other minerals. Finally, nodular carbon has very little visible uraninite within it, only at a micron-scale can small amounts of uraninite grains be seen. Even though gold is not always directly associated with uranium minerals, gold is always in close proximity to the features that hosted uranium phases.

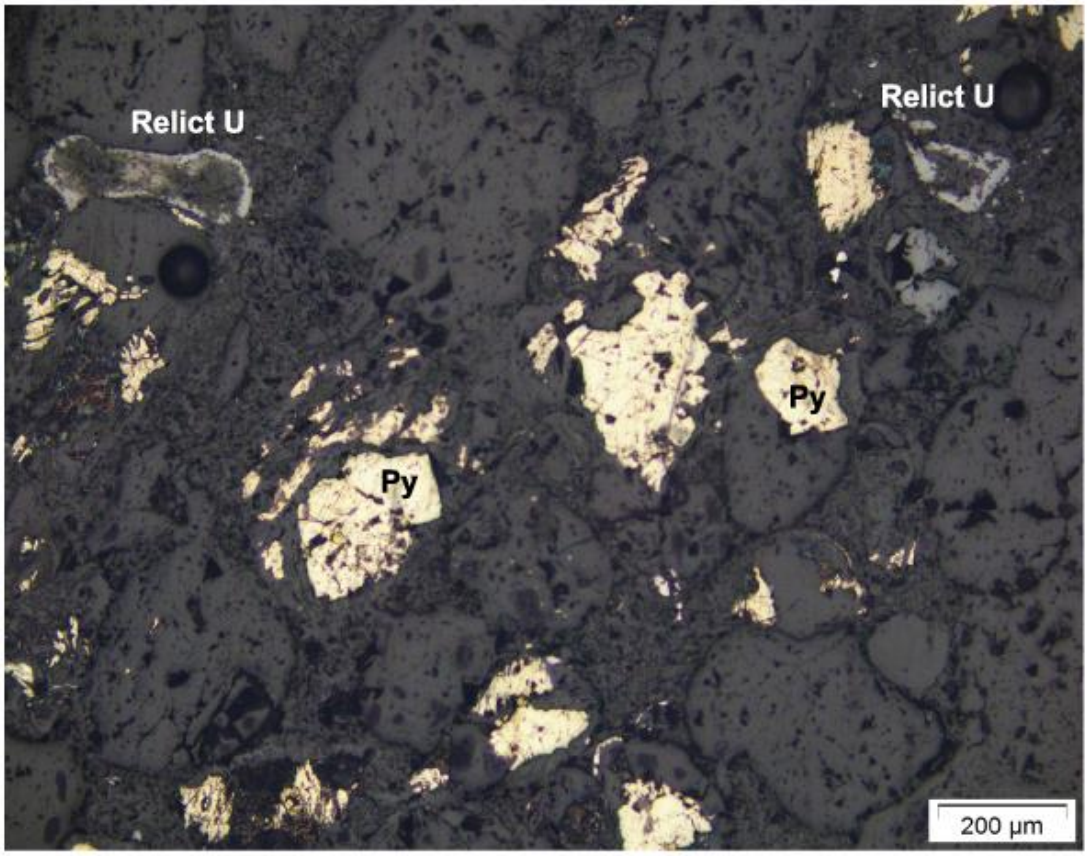


Figure 3.3 Reflected light image of relict uraninite grains in MGS4063
Sample from the Main Reef Leader showing uraninite grain outlines (relict U) with the quartzite. The centres of the grains are replaced by fine grained phyllosilicate minerals. The pyrite (Py) in this sample is also extensively affected by fine-grained secondary quartz and phyllosilicate minerals.

3.1.2 Gold

Gold within the samples ranges from barely visible and less than 10 µm particles to visible nuggets and stringers between carbon spindles of 2 mm length. Gold within the samples tends to fill in spaces in fractures and veins as well as the interstices between grains. In general, gold is shaped as rounded micro-nuggets or interstitial masses of gold, conforming to the boundaries of the surrounding minerals (Figure 3.4).

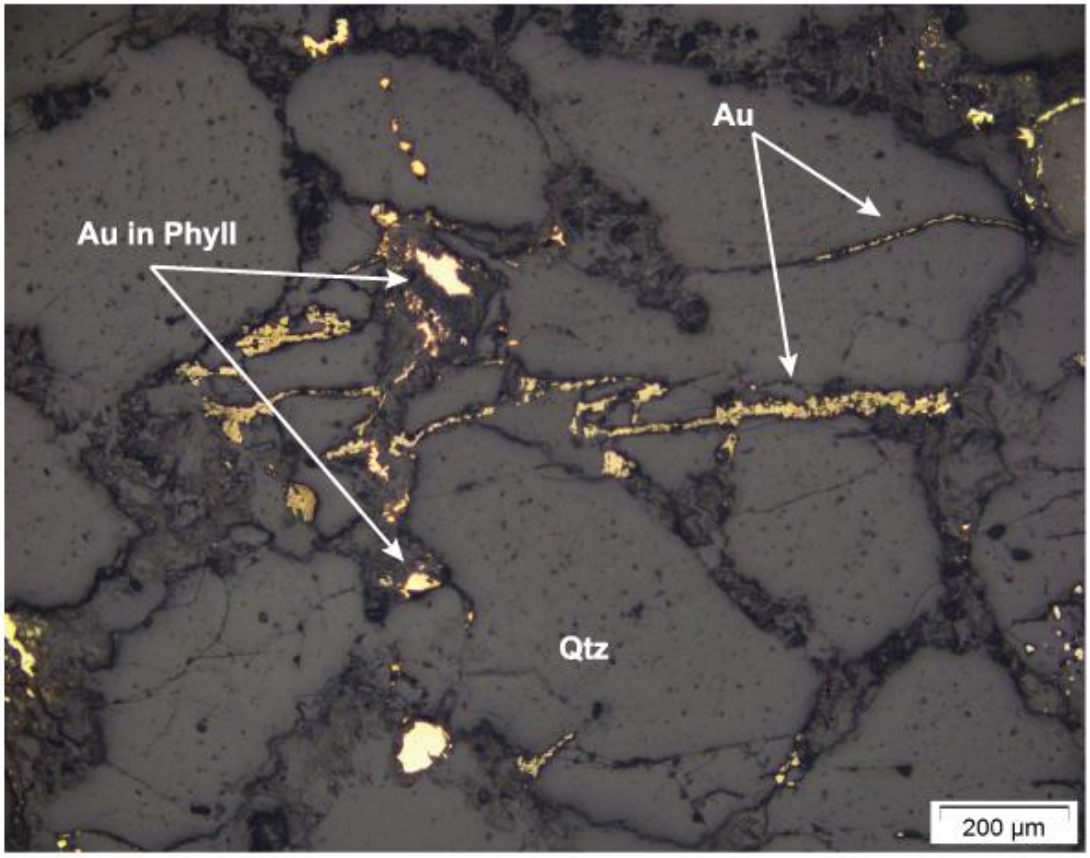


Figure 3.4 Reflected light image of gold in veinlets and phyllosilicate matrix minerals in MGS4071
Main Reef Leader sample showing a number of gold features in a sample with no visible uranium minerals or carbon. Gold is seen here as veinlets (Au) in fractured quartz clasts, and interstitially between quartz grains in the phyllosilicate matrix (Au in Phyll).

In many samples, even though the sedimentary features seem to be the dominant texture, gold particles are found within alteration/secondary minerals and small-scale secondary features. Gold in some samples is not visible, and in other samples is abundant and easily identifiable. Many variations of gold distribution, size and textures between are noted in the sampled reefs. For instance in MGS6514 gold occurs within the pyrite grains, and almost nowhere else within the samples (Figure 3.5).

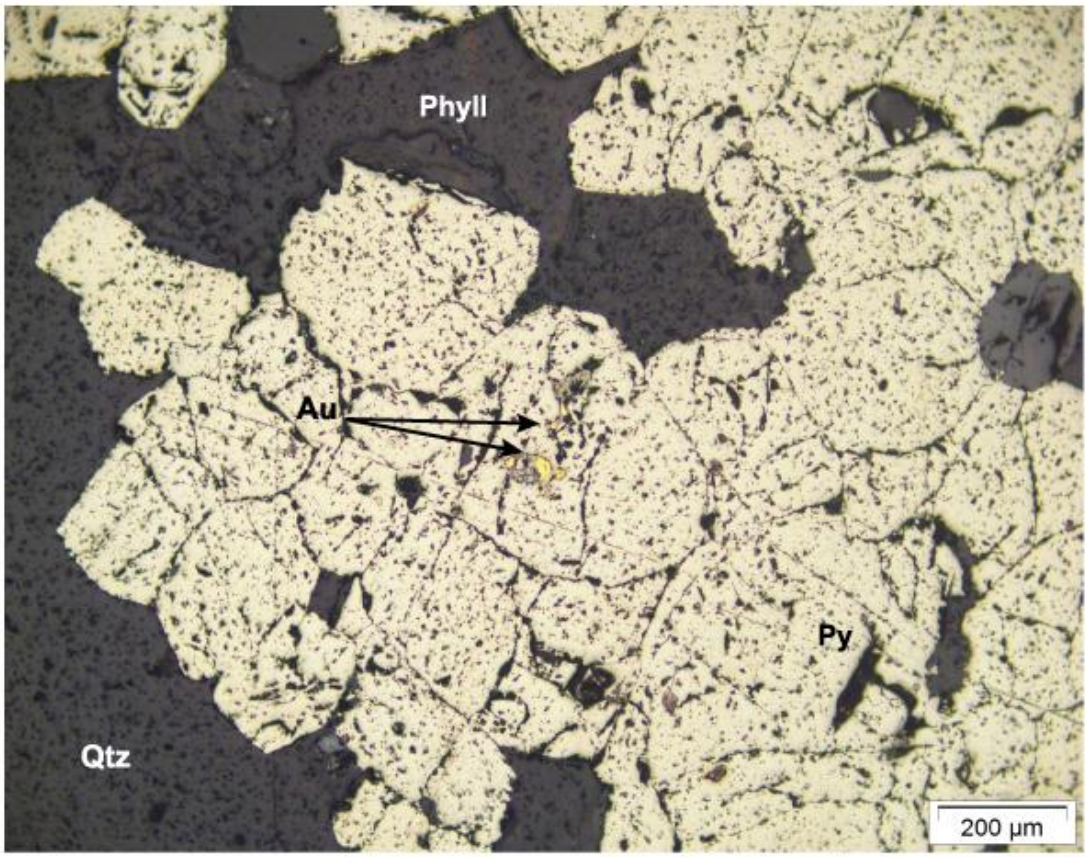


Figure 3.5 Reflected light image of gold within euhedral pyrite in MGS6514
Sample from the Vaal Reef with euhedral to subhedral authigenic pyrite grains (Py) that are closely packed together in quartz (Qtz). There is a small portion of phyllosilicates (Phyll) adhered to the face of some pyrites.

In contrast, in many other samples gold occurs in close proximity to sulphides but only as rims or separate grains. Carbon displays variations in gold occurrence as well. In well-developed seams with spindles, gold occurs between the spindles of carbon. Inter-spindle gold is skeletal and quite large, see Section 3.1.3. However, where the carbon does not have well-defined spindles, gold occurs as minute inclusions that tended to occur randomly throughout the carbonaceous material. Gold is also noted within phyllosilicate matrix material that includes sericite, phlogopite, pyrophyllite, muscovite, sericite and quartz. In the phyllosilicate matrix gold is skeletal and infills the interstices between larger phyllosilicate grains, within the matrix (Figure 3.6).

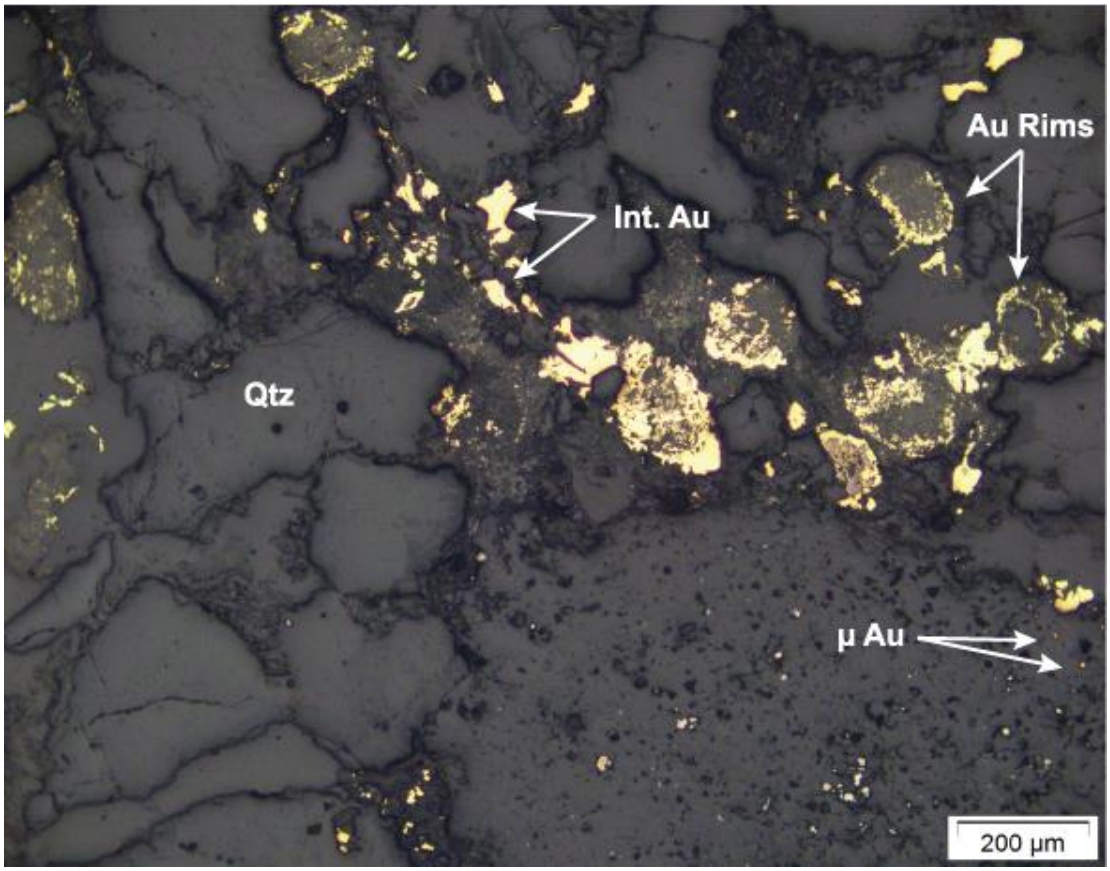


Figure 3.6 Reflected light image of various gold forms in MGS4071
Main Reef Leader sample showing various forms of gold. Gold occurs as: rims on rounded oxide grains (Au Rims), as interstitial forms between quartz grains (Int. Au) and as micron-scale Au in porous spaces in silicate minerals (µ Au).

In sample MGS4071, gold is exceptionally abundant and is not associated with sulphides or carbon. Instead gold is contained within silicates as inclusions in porous spaces, as veinlets, as rims, as rounded grains and interstitial to silicate grains (Figure 3.6). However, sample MGS4071 is an exceptional sample. In general the most common and abundant mineral forms associated with gold are carbon nodules and seams

3.1.3 Carbon Forms

Carbonaceous material content in the samples ranges from less than 1% of tiny nodules (~1 mm) up to 3 cm thick seams with well-developed spindles and gold mineralisation (comprising 35% or more of the reef). One Beisa Reef sample contains a 25 cm thick carbon seam with multiple

centimetre thick visible phases of gold. However a standard polished section of the Beisa Reef sample could not be made that would reflect all of these thick carbon phases. The nodules in all samples tends to be rounded or globular. Nodular carbon is also abundant throughout reef samples.

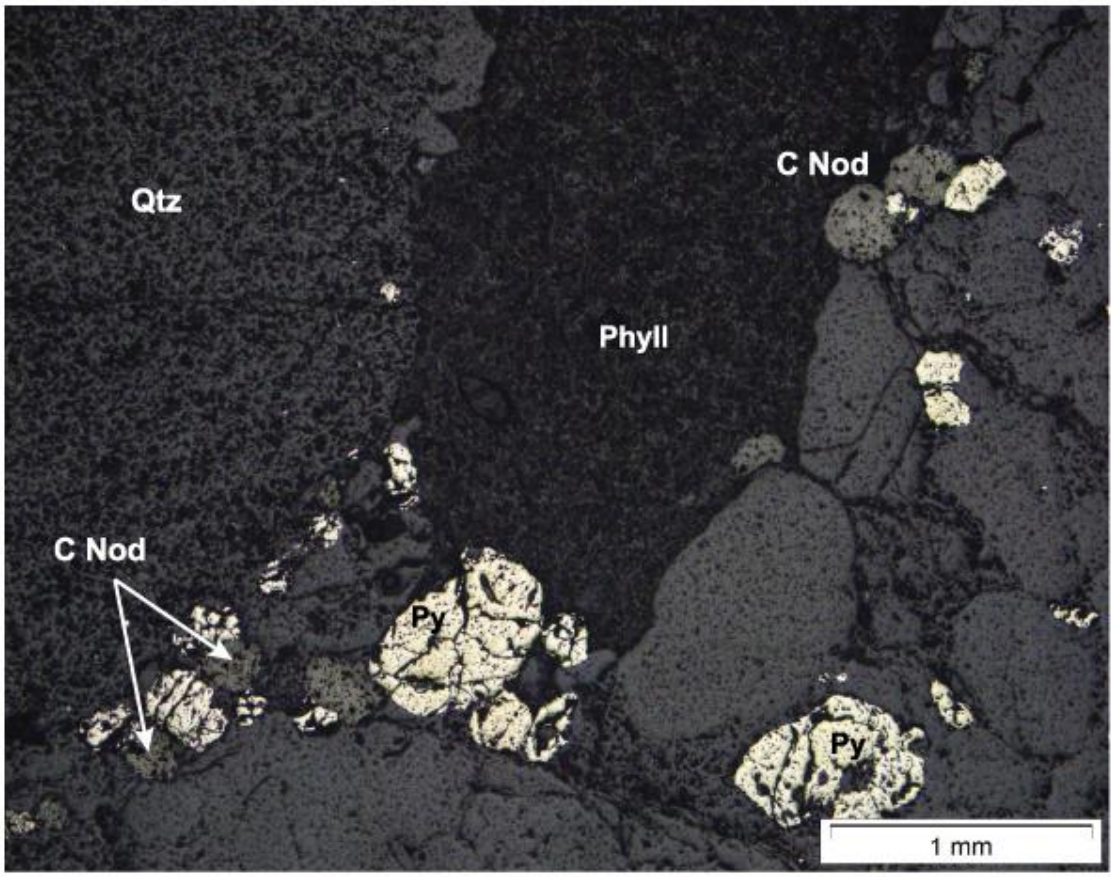


Figure 3.7 Reflected light image of rounded carbon nodules in CREEF07
"C" – Reef sample showing rounded carbon nodules (or "flyspeck" carbon) in a conglomerate. Carbon nodules (C Nod) are associated with phyllosilicates and secondary quartz (Qtz). The nodules also form near pyrite grains (Py), but they form in association with the pyrite grains

Although the nodules appeared rounded in hand sample when viewed under the microscope it is clear that for the most part nodules filled up interstitial spaces, giving them an irregular appearance (Figure 3.7). Carbonaceous materials were secondary to the sedimentary clasts. Although the carbonaceous materials are also cut by secondary features e.g. chlorite infilling the carbon nodule in Figure 3.8.

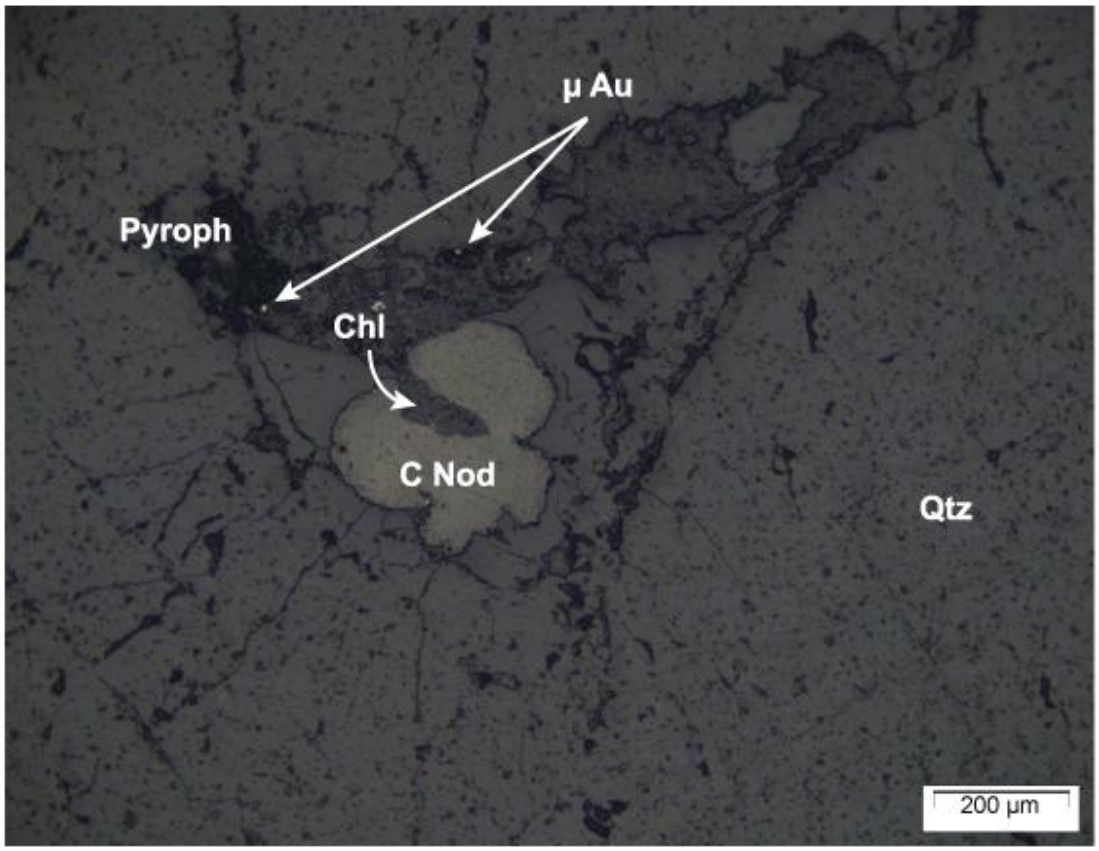


Figure 3.8 Reflected light image of an irregular carbon nodule in VCR1
Carbon nodule from the Ventersdorp Contact Reef (VCR). The carbon nodule (C Nod) has an irregular shape as it infills the interstitial space between quartz grains (Qtz) in a large pebble conglomerate. A small amount of phyllosilicate minerals surround one side of the nodule, with a small portion of chlorite (Chl) partially infilling the nodule. The phyllosilicate material includes some micro-scale Au (µ Au) and fine grained pyrophyllite (Pyroph.)

Nodular carbon contained some minor pyrite and uraninite micron-scale grains that occurs sporadically (<0.05mm). Carbon seams range from small clusters (1 mm thick) of nodular material with no spindle forms (Figure 3.9), to seam 3 mm and greater with visible spindles. Carbon seams include fibrous spindles of carbon that with gold, quartz, pyrite and minor sericite between the spindles (Figure 3.10). This material was investigated further in Chapter 6. Seam carbon can also include rounded forms of nodular carbon within the elongated carbon spindles; LGM3 displays a good example of these multiple carbon forms (Section 4.2.3), with a nodule surrounded by spindles of a later carbon seam.

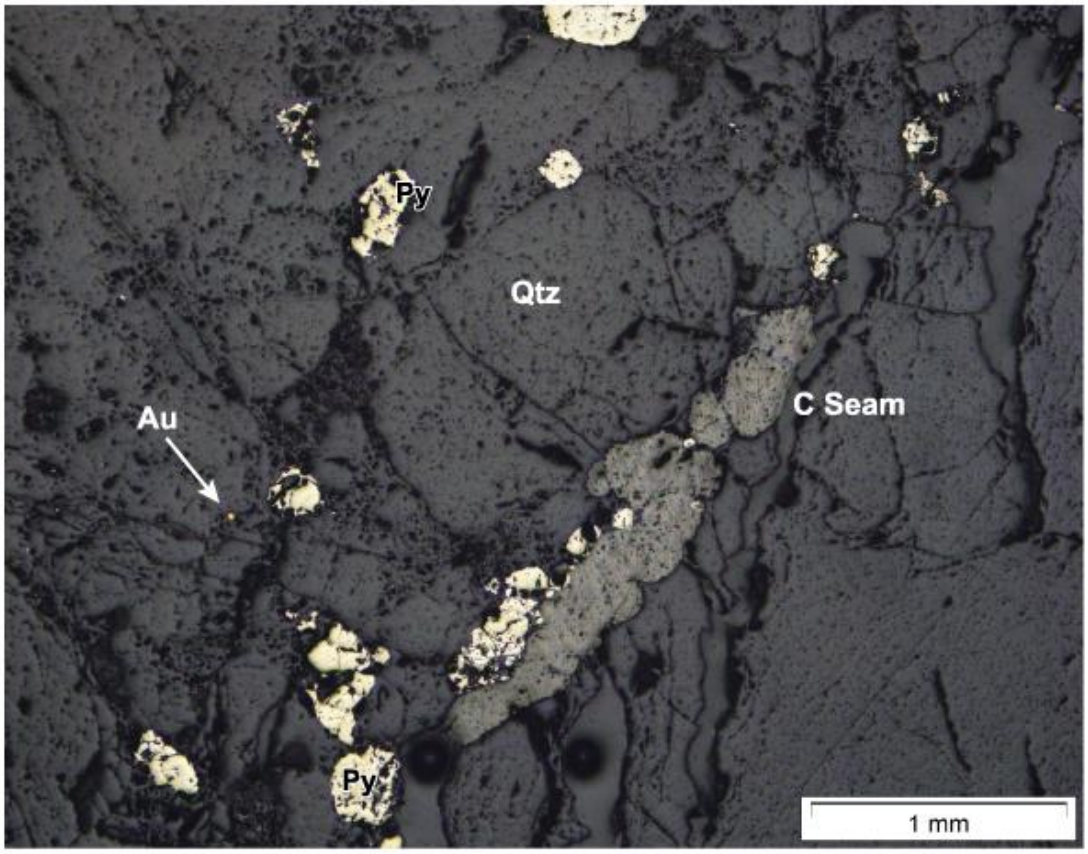


Figure 3.9 Reflected light image of a thin discontinuous carbon seam in CREEF07
"C" – Reef sample showing a thin carbon seam (C seam) here is a number of smaller nodular materials that has agglomerated to form a seam. There is a small amount of gold in the quartz material (Qtz) as well as on the boundary between the carbon seam and a pyrite grain (Py).

Carbon seams tend to be discontinuous and contained portions of secondary quartz grains or quartz pebbles between them. The quartz contained in seam carbon is invariably fractured and infilled with sericite and minor pyrophyllite, although these infilled fractures do not continue into the seam material. In the case of sample DFN10 from the CLR, calcite veins cut through the thinner carbon seam material and fractured quartz-phyllosilicate material (Figure 3.11).

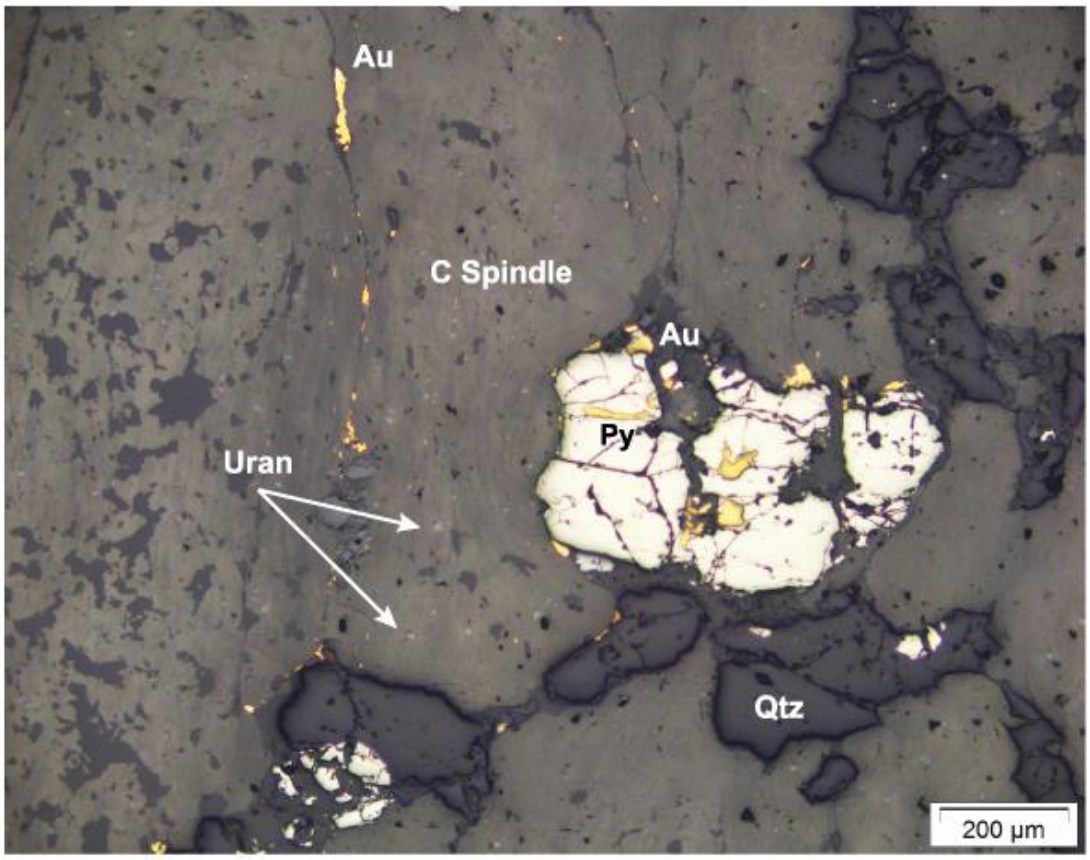


Figure 3.10 Reflected light image of carbon spindles with gold between the filaments in WD20
Carbon Leader Reef sample showing a carbon seam that has well-developed spindle structures (C Spindle) seen from the variations in reflectance within the carbon. Gold (Au) is found both between the spindles and within the fractured pyrite grain (Py). There are also a number of smaller secondary quartz inclusions in the seam (Qtz) and micro-particles of uraninite (Uran).

However, in the same sample there is a thicker carbon seam portion that was not cut by the calcite veinlets, this portion of the seam also contained significantly greater concentrations of gold (Figure 3.12). The orientation of this seam appeared to be different from the thinner discontinuous seam, with rounded spindles presented in this section. The second thicker seam region also displays areas with little or no uraninite grains. Carbon seam bases occur along quartz pebbles beds (in the footwall) and the tops abut against quartzite (in the hanging wall). The carbon seams include pebble material seemingly from the conglomerate footwall. Carbonaceous materials are also closely associated with pyrite grains.

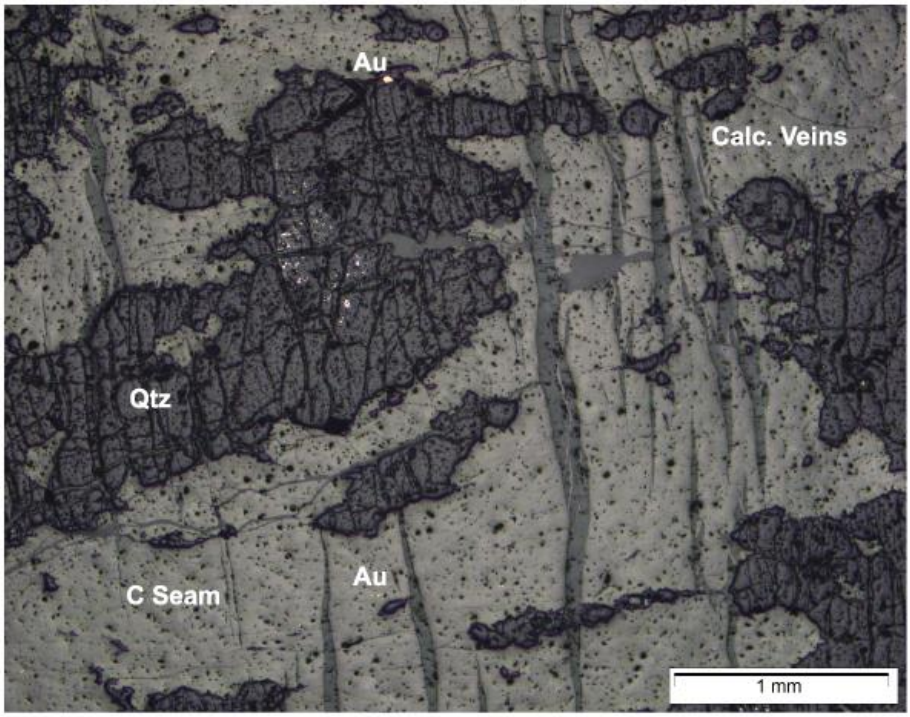


Figure 3.11 Reflected light image of a carbon seam cut by calcite veins in DFN10
Sample from the carbon leader reef Calcite veins (Calc. Veins) cutting through a carbon seam (C Seam) as well as the secondary quartz inclusions. Gold (Au) is located within the quartz portion as well as within the carbon seam

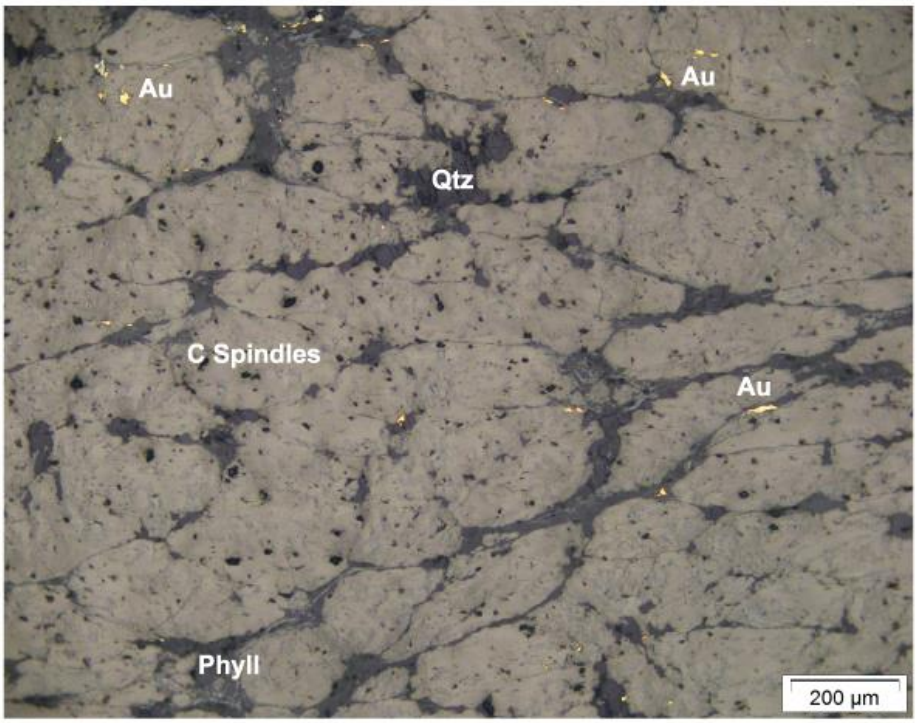


Figure 3.12 Reflected light image of carbon seam spindles with less U and no calcite veins in DFN10
Same CLR same sample as Figure 3.11, although the seam here is not cut by the calcite veins and the carbon seam shows rounded forms characteristic of a section taken perpendicular to the long axis of the spindles (C Spindles). Gold (Au) as well as secondary quartz (Qtz) and phyllosilicate minerals (Phyll) between the rounded forms of the spindles

The best example of carbonaceous materials associated with pyrite is seen in Figure 3.13 - Figure 3.15. The sample was taken from a vug in a dyke that cross cuts the Witwatersrand Reefs. The sample displays multiple cubic pyrite forms that enclose a carbon nodule (Figure 3.13). Striations are observed on the surfaces of the euhedral pyrite grains (Figure 3.13).

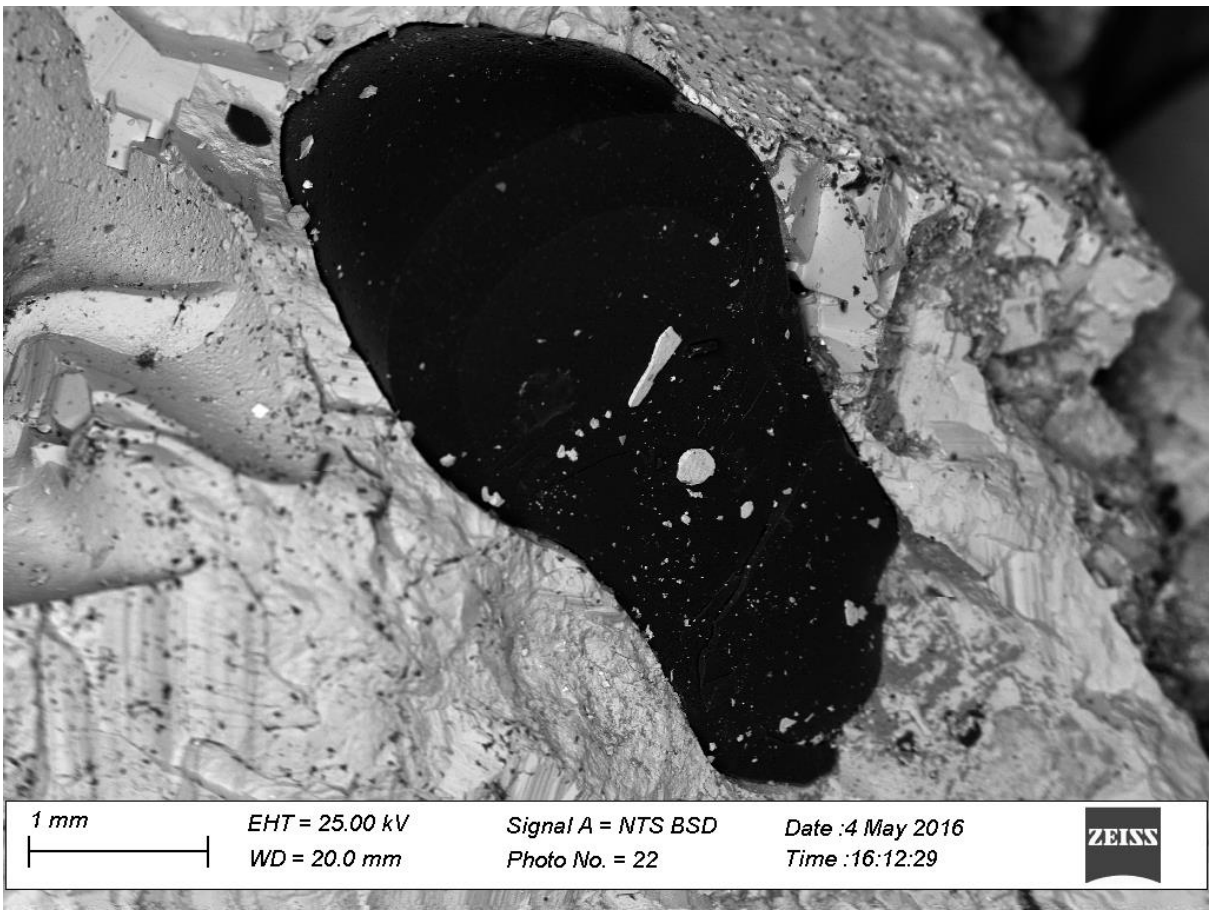


Figure 3.13 Electron Microscope Image of the Carbon Nodule in Recrystallised Pyrite
BSE image of carbon nodule encapsulated in cubic pyrite from a vug sampled in a dyke that cross-cuts the Beisa Reef. The nodule contains a number of other mineral phases within it. Also seen are micron-scale inclusions of carbon throughout the recrystallised pyrite.

The carbon nodule contained a number of minerals that required electron microscopy in order to more closely examine the mineral contents. Back scattered electron (BSE) images show the carbon nodule is rounded and narrows towards the centre (Figure 3.13). The carbon nodule contains globules of pyrite both on the exposed surface and inside the nodule. Interestingly, the pyrite crystals also contain globular micron-scale carbonaceous materials. These micron-scale inclusions are dispersed throughout the pyrite crystals, especially closest to the large nodule.

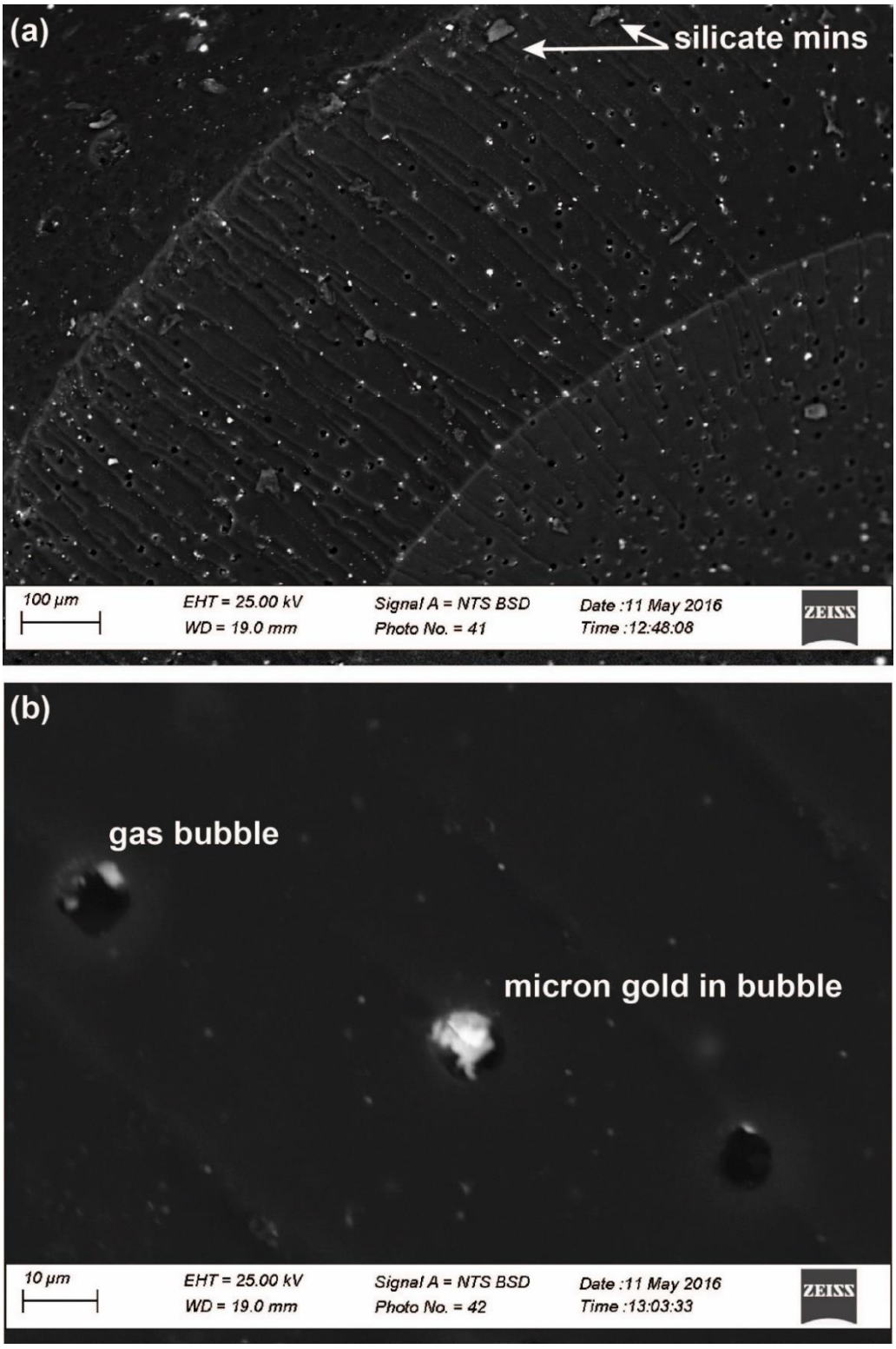


Figure 3.14 Electron Microscope Image showing the micron-scale inclusions of minerals
BSE image of (a) growth structure of carbon on the exposed interior surface of the nodule containing micron-scale gold, pyrite and silicate minerals. Additionally, the nodule contains gas bubbles within its structure, (b) an enlarged view of these gas bubbles shows micron-scale skeletal gold within the gas bubbles.

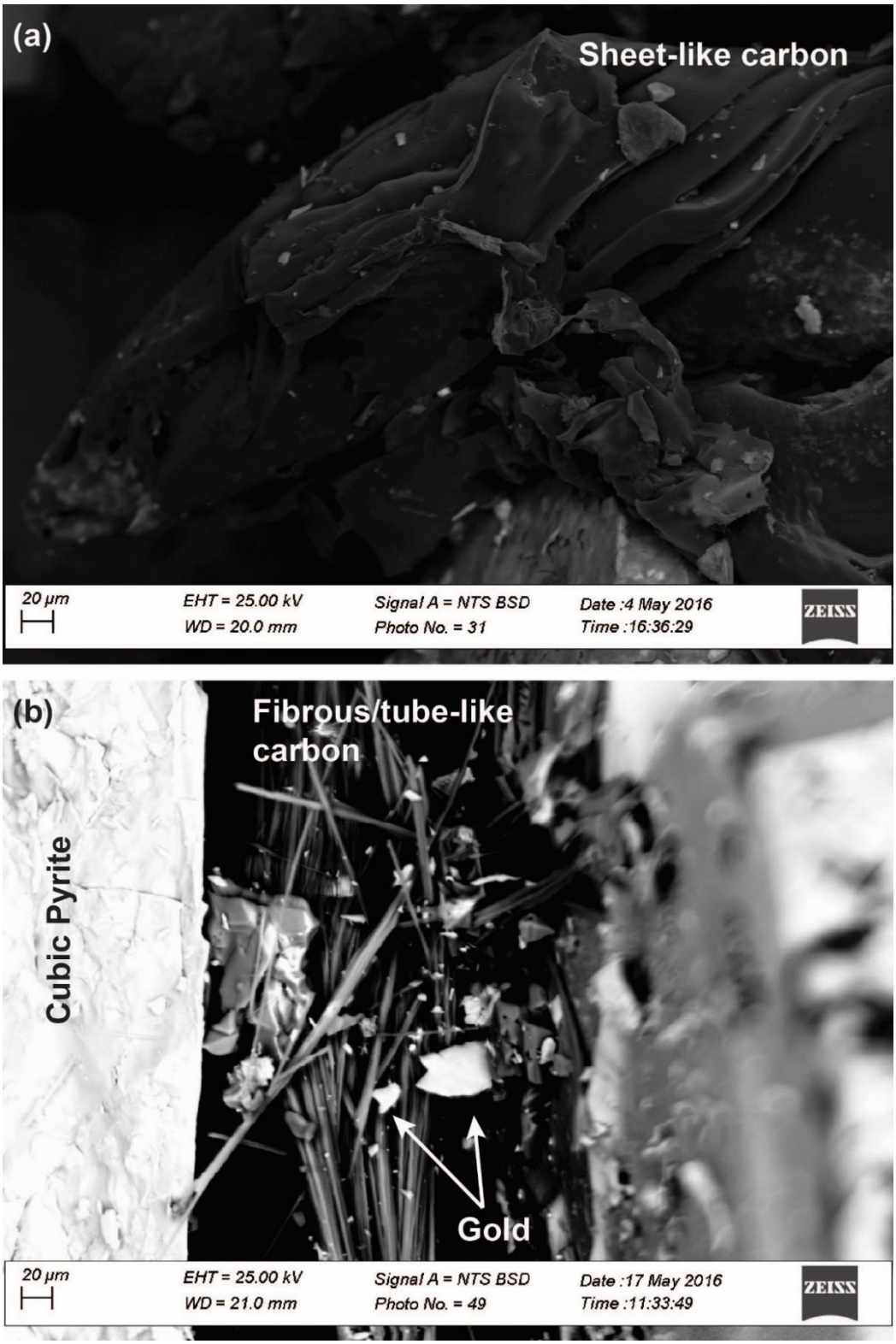


Figure 3.15 Electron Microscope Image showing the micron forms of carbonaceous materials
BSE image of other carbon forms from the vug sample show (a) a fractured carbon nodule where the sheet-like nature of the carbon is evident and, (b) a bundle of fibrous/tube-like carbon contained in the space between cubic pyrite grains. Additionally, gold and pyrite is seen adhered to the surfaces of the fibrous carbon bundle.

Closer inspection of the largest carbon nodule reveals a number of lineaments, described as growth structures, radiating outwards from the centre of the carbon nodule (Figure 3.14a). The nodule also contains remnant gas bubbles (Figure 3.14a & b). These bubbles contain micron-scale to nano-scale crystals of skeletal gold (Figure 3.14b). The carbon nodule contains carbonaceous materials exhibiting a closely packed structure. With the exception of the gas bubbles, there are no gaps in the form of the large nodule (Figure 3.14b). However, the sample also contains a less structured carbon nodule (Figure 3.15a). The less structured nodule displays the sheet-like structure of carbonaceous materials at the micron-scale. Additionally, in one of the gaps between euhedral pyrite grains there is a bundle of fibrous/tube-like carbon materials, confirmed by EDS spectra (Figure 3.15b). These fibrous carbon forms appear to have formed in a space between the pyrite grains that is noticeably less restricted than the closely packed arrangement of carbon and pyrite in Figure 3.13. The fibrous/tube-like carbon bundle also contains gold and pyrite crystals ranging from <1 µm – 30 µm in size, these crystals adhered to the surfaces of the bundle. As with previous nodular samples no uraninite was observed in this sample.

3.1.4 Sulphides and Pyrite

The second most abundant mineral after the dominant quartz in the suite of samples examined is pyrite. Pyrite, as the literature describes (see Section 1.7.2) occurs in a number of forms: rounded grains, euhedral grains or as spongy rounded forms (these may be concentrically laminated as well). Most common pyrite grains are rounded to sub-rounded grains with solid textures or spongy/porous textures that include other sulphides and silicate minerals (Figure 3.16). Replacement textures are also common in the pyrite grains with skeletal or globular textures within the grains where secondary silicate minerals were seen, as in sample MGS4355 (Appendix C).

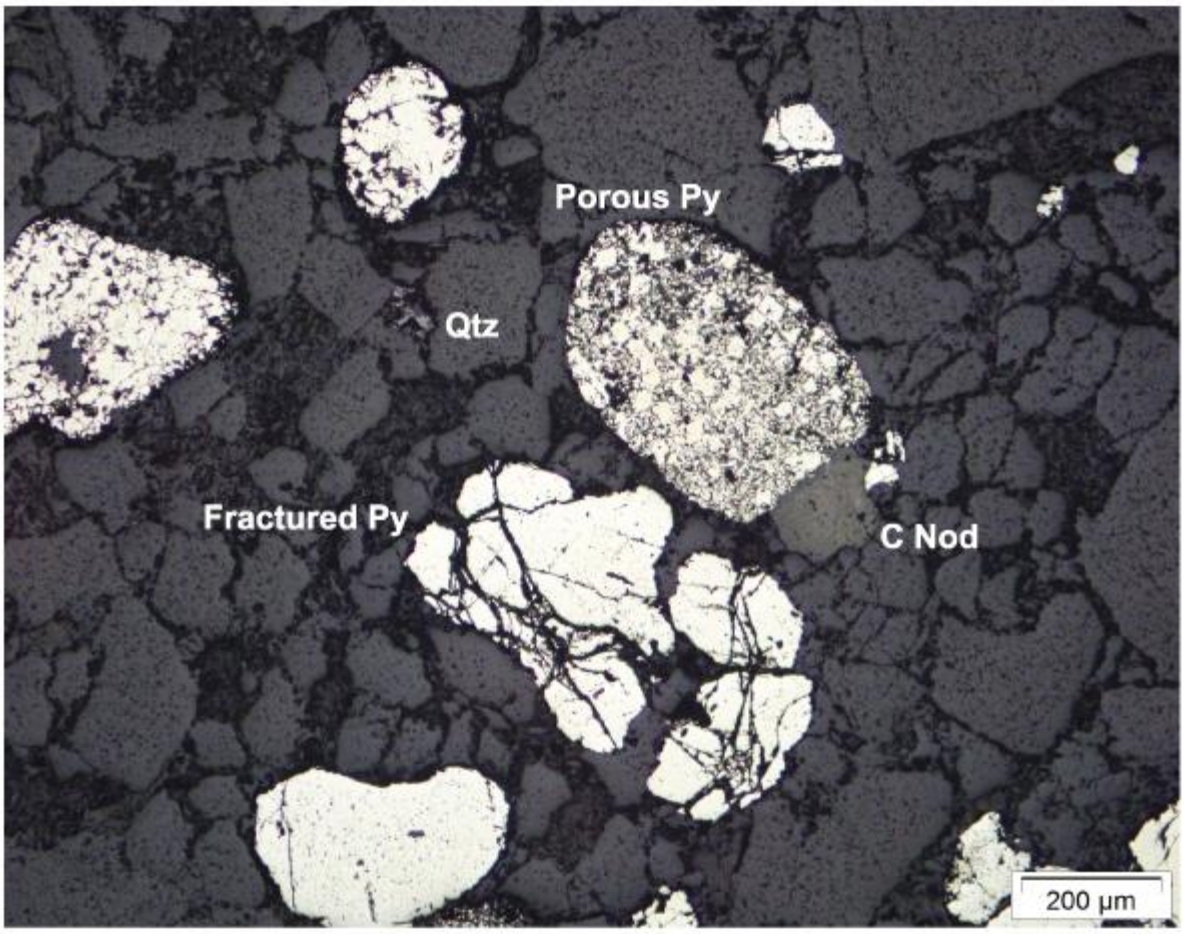


Figure 3.16 Reflected light image of typical rounded pyrite textures in LGM6
Sample from the Basal Reef showing rounded to sub-rounded forms of pyrite including a porous or spongy pyrite, a relatively unfractured grains and a severely fractured pyrite grain (Fractured Py). Additionally there is a carbon nodule adhered to the surface of the porous pyrite grain (Porous Py). The sample is dominated by quartz (Qtz) with very few phyllosilicate minerals.

Euhedral pyrite grains occur less regularly than rounded grains, but grains with well-defined cubic and hexagonal crystal faces are common (Figure 3.17). These are also the most common grains that hosted visible gold inclusions. Secondary fractures were present in all forms of pyrite and these fractures are often infilled with gold, secondary quartz, phyllosilicates and other sulphide minerals (Figure 3.17). Other sulphide minerals that occur interstitially or as solid-solutions with pyrite include: chalcopyrite, pyrrhotite, pentlandite, gersdorffite, cobaltite and sphalerite (e.g. MGS6513, BND2 in Appendix C).

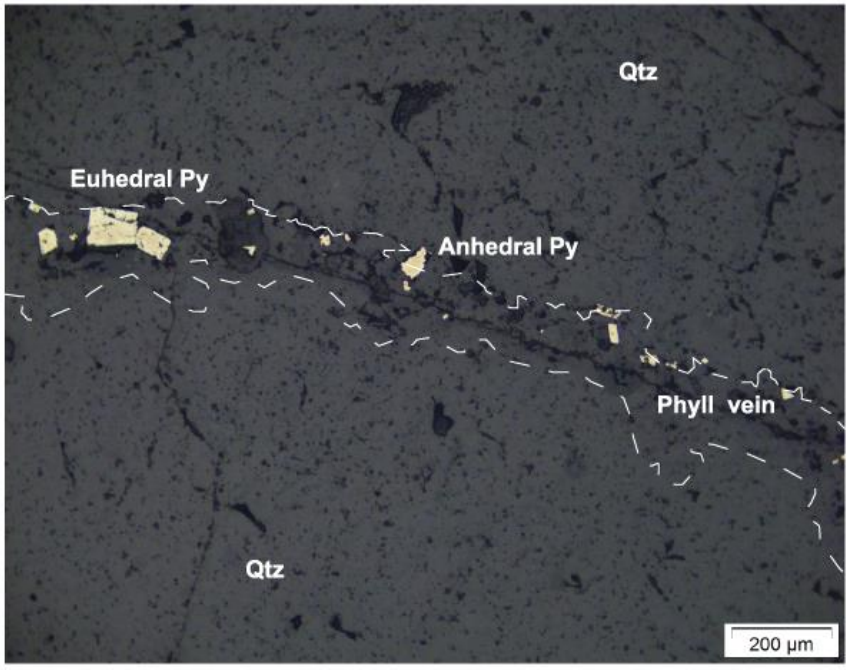


Figure 3.17 Reflected light image of euhedral pyrite within a phyllosilicate veinlet in LGM16
Basal Reef sample showing a phyllosilicate veinlet. The dotted white line shows the extent of the phyllosilicate veinlet within the sample (as seen from transmitted light). Within the veinlet are a number of euhedral pyrites (Euhedral Py) and some anhedral forms (Anhedral Py). The veinlet cuts through a quartz-rich (Qtz) pebble conglomerate.

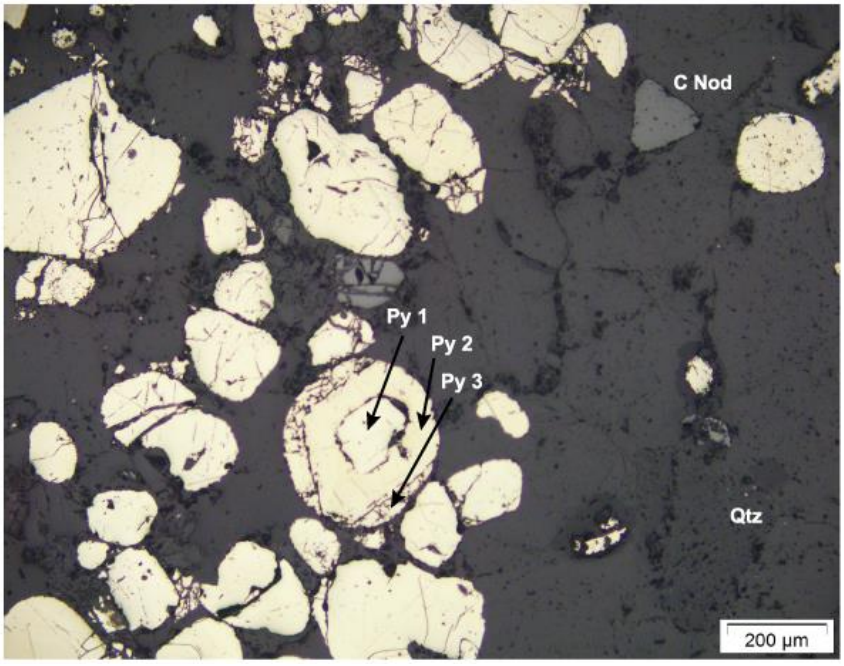


Figure 3.18 Reflected light image of multiple pyrite forms in a single grain in MGS6513
Vaal Reef sample containing allogenic pyrite grains from the Vaal Reef. In this sample it is clear that multiple pyrite forms occurred in a single grain. Pyrite 1 is a subhedral grain with a small amount of silicate material surrounding it. Pyrite (Py 2) encloses Py. 1 and is more euhedral. Py. 3 has overgrown both earlier pyrite phases (Py 1 and Py 2) and the composite grain has undergone rounding

Sulphides also occur sporadically throughout the reefs or as alignments with bedding planes. In sample MGS6513, a sub-rounded pyrite is surrounded by a more euhedral pyrite phase, which is in turn surrounded by a final phase and the whole grain was rounded and clearly allogenic (Figure 3.18). This sample showcases the numerous processes that affect pyrite grains. Secondary mineral phases are abundant not only within pyrite, but in Au-U-C associations as well.

3.1.5 Alteration and Other Minerals

Altered minerals and secondary phases of metamorphic minerals are common in every sample. In general the minerals formed occur as a small (<0.2 mm) ground-mass between quartz, pyrite and carbonaceous materials. Appendix C highlights the variations in proportions of phyllosilicate materials. The fine-grained alteration minerals include: sericite, pyrophyllite, phlogopite, muscovite, secondary quartz, chlorite/chloritoid and other minor mineral phases (Figure 3.19).

Larger grains of alteration and/or metamorphic minerals are common, for instance large metamorphic chlorite grains, laths of chlorite/chloritoid near pebble boundaries (Figure 3.20), large grains replaced by pyrophyllite/sericite and flakes of phlogopite. These grains range from 3 mm to 20 mm in size (see alteration in Appendix C). The alteration minerals are most often associated with the quartz as a matrix. However, gold, primary and secondary uranium-bearing minerals and pyrite are also located within this groundmass. Accessory minerals seen in the samples are noted, these included: zircon, hematite, chromite and rutile, among others. The associations between the variety of minerals examined here and the distribution of Au-U-C associations demonstrates the complexity of the various mineral phases.

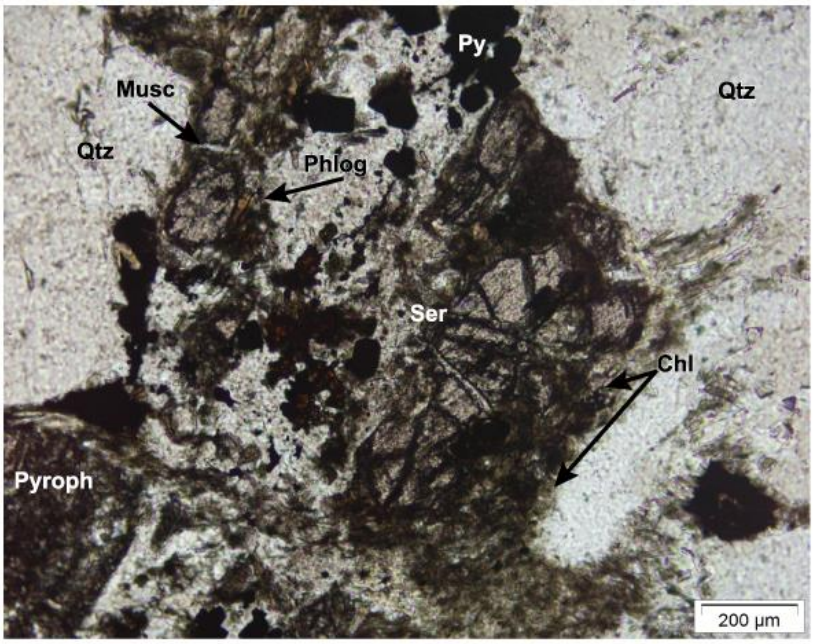


Figure 3.19 Transmitted, plane-polarised light image of alteration minerals in BDN2
Dominion reef sample showing fine-grained alteration mineral matrix. The phyllosilicate minerals in the matrix include sericite (Ser) closely associated with secondary quartz. Chlorite/chloritoid (Chl) laths fill the space around quartz grains (Qtz) muscovite (Musc) also occurs in these areas. There is also a small amount of fine grained pyrophyllite (Pyroph). All of these phases are fairly amorphous except for the opaque secondary pyrite grains (Py).

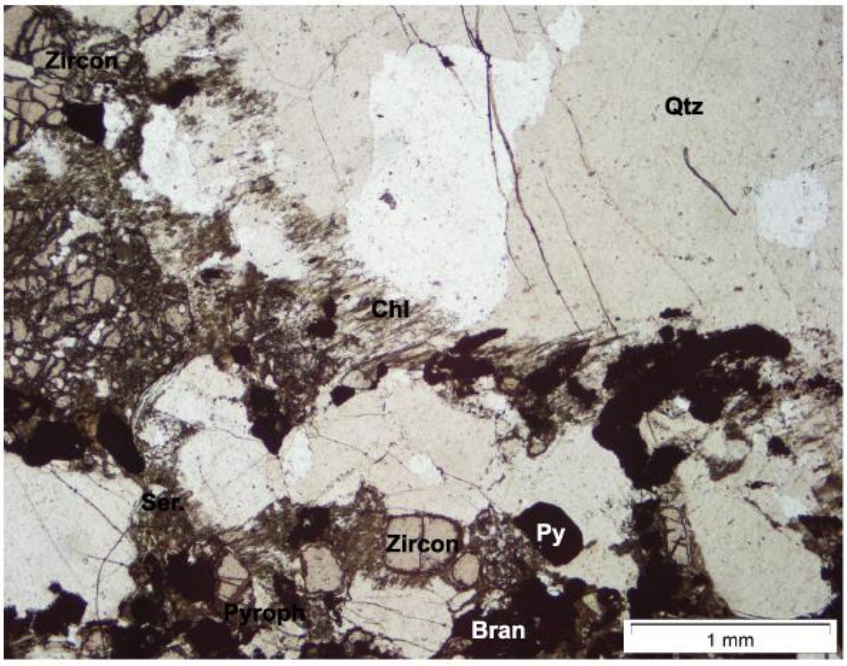


Figure 3.20 Transmitted light image of alteration minerals within matrix of BDN2
Dominion Reef sample showing replacement of a large quartz grain. Fine-grained alteration mineral in the matrix include sericite (Ser.) closely associated with secondary quartz. Chlorite/chloritoid (Chl) laths fill the space around the large quartz grain (Qtz). There is also a small amount of fine grained pyrophyllite (Pyroph.). All of these phases are fairly amorphous except for the opaque pyrite grains (Py), zircon and secondary brannerite/coffinite (Bran)

3.2 Petrography Discussion

Mineralisation in the Witwatersrand Basin has been attributed to initial sedimentary deposition and then later components of remobilisation (Robb and Meyer, 1995; Robb and Robb, 1998). The extent and resultant textures are indicative of remobilisation varies for gold, uranium minerals, carbon, pyrite and phyllosilicate minerals. For example certain researchers have provided evidence for sedimentary control of mineralisation (e.g. Minter *et al*., 1993), whereas other research provides evidence of remobilised gold and hydrocarbons (e.g. Drennan and Robb, 2006; Phillips and Powell, 2011). Clearly there is an abundance of textural and mineralogical information for the Witwatersrand Basin, and it would be difficult to present any new findings in this regard. Although many of these features have been described in past studies, the samples for this study reflect undescribed material made available for this research from previously inaccessible collections. The features examined in this chapter provide renewed evidence for the extent of hydrothermal/alteration features with regards to gold and hydrocarbons. Thus, focus was given to the gold and carbon in the samples and the processes represented by the form and textures observed. Gold in the samples occurs as veinlets, rims on oxide grains, as micro-particles in phyllosilicates and secondary quartz, as inclusions in secondary pyrite grains and as inclusions in carbon seams and nodules. All of these features indicate that gold in these instances was formed by remobilisation. This contradicts the view that only 25% of the gold is hydrothermal in nature (Minter *et al.*, 1993). In fact the distribution and morphology of gold in this sample suite suggests that most of the gold associated with carbonaceous reefs has a strong component of remobilisation. This supports a modified placer model for the Au-U-C associations, as suggested by Robb *et al. (*1997) and Drennan and Robb (2006).

The carbonaceous materials in the samples contained gold inclusions in between the spindles as well as smaller particles within the spindles indicated that remobilised gold was present at the time of the formation of the carbon seams. Carbon seams also include quartz clasts and pyrite clasts in between spindles. Additionally micro-particles of uraninite are contained within carbon seams, and these particles are fragmented and displaced by the carbonaceous matter between the grains. It is difficult to reconcile these features with a syndepositional model of formation. In order for organic matter to trap dense minerals such as pyrite, gold and uraninite; high velocity

water would be required. However, this would remove low density carbonaceous materials at the time of deposition. Also it does not explain why carbonaceous materials are associated with secondary phyllosilicates and skeletal gold between the spindles.

Instead the features examined in the carbon seams supports the view of migrating oils (England *et al.*, 2002) and radiolytic polymerisation around uraninite grains (Schidlowski, 1981). Additionally, multiple phases of carbon were noted in this study as well as other studies of carbon remobilised in quartz veins (Drennan and Robb, 2006). Therefore, most of the carbonaceous products and gold do not appear as inherently primary minerals. This is further supported by the electron microscope images of the sample from a vug in a cross-cutting dyke, clearly a secondary mineral feature. The presence of carbon from the vug supports the view that carbon was secondary. In addition, the secondary carbon contained in the vug sample displays fibrous/tube-like forms. These complex structures are viewed at the sub-micron-scale, and clearly cannot be the fossilised remains of Archean life-forms as suggested by other researchers (Hallbauer, 1975). Instead, the complex fibrous carbon bundles must be the result of ordered carbon structures produced by hydrothermal precipitation.

Pyrite in the sample suite occurs as both rounded forms and euhedral forms in the phyllosilicate matrix and veins. Therefore, it appears that the rounded pyrite was deposited by fluvial processes as suggested by Maclean and Fleet (1989) and Kirk *et al.* (2001). However, euhedral pyrite and pyrite found in phyllosilicate veins was clearly remobilised. Thus pyrite in these samples is indicative of multiple concentration processes as proposed by *(Agangi et al., 2013; Large et al.*, 2013). Pyrite is contained gold inclusions that appear to be secondary phases filling in around pyrite and within euhedral pyrite grains. Importantly, phases of chalcopyrite, galena and pyrrhotite are been attributed to later generations of sulphides (Agangi *et al*., 2013) and intrabasinal scavenging fluids (Large *et al*., 2013).

Phyllosilicates in the samples contain sericite, pyrophyllite, phlogopite, muscovite, secondary quartz and chlorite/chloritoid. These minerals have been characterised as metamorphic (see Section 1.4). These alteration minerals contain micro-particles of gold, and occur between the spindles of carbon seams. As such it would appear that the metamorphosed phyllosilicates have

interacted with the gold and carbonaceous materials. Due to the fine-grained nature of the phyllosilicates it is difficult to determine what this effect is with petrography alone. The fine-grained nature also makes it difficult to ascertain what percentage of alteration minerals were present before gold and hydrocarbon formation.

Therefore, while an initial sedimentary component is important for distributing gold, uraninite and pyrite, a secondary fluid component for mineralisation needs to be considered. Fluid inclusion studies provide evidence of both gold and hydrocarbon remobilisation (see Section 1.9). Consequently, it is desirable to know the elemental distributions within mineral phases in carbonaceous materials in order to understand the possible chemical mechanisms with respect to remobilised hydrocarbon fluids.

3.3 Conclusions

- Petrographic samples show variations of Au-U-C minerals and pyrite across the sampled reefs, samples contain sedimentary features including, rounding and bedding.
- However, sedimentary features were overprinted by hydrothermal features, including secondary gold and pyrite infilling fractures and occurring as overgrowths on rounded primary grains, and secondary uranium phases such as brannerite etc.
- Hydrocarbons display features that include fibrous/tube-like forms, sheet-like materials, cross-cutting features and multiple hydrocarbon phases.
- Numerous phyllosilicate and pyrite minerals are intimately, but variably, associated with the secondary mineral phases, especially within the matrix of the conglomeratic horizons.
- Hydrocarbon and gold textures are not consistent with synsedimentary deposition, therefore fluid remobilisation should be considered as a crucial process in the formation of Au-U-C associations in the Witwatersrand Basin.

4 PIXE Study of Element Distribution within Carbon Forms

4.1 Introduction

In order to determine what elements are associated with Au-U-C in the Witwatersrand Basin, PIXE micro-mapping was undertaken. Results of the petrographic study (Chapter 3) indicated that hydrothermal fluids had affected mineralisation needed to be considered. Both nodular and seam carbon forms were investigated to establish to determine the effect that they had on mineralisation within the Basin. Furthermore, PIXE data was used in an attempt to establish possible mechanisms associated with carbon precipitation.

The results of the carbon seam materials in this Chapter were submitted for publication as:

Woods, T.H., Drennan, G.R., and Przybylowicz, W.J., 2016b, Elemental Micro-maps of Au-U-C associations in Carbon Seams from the Witwatersrand Basin: Evidence for Multi-Component, Multi-Fluid Remobilisation of Mineralisation: Ore Geology Reviews, Submitted.

The result for the carbon nodules will form part of a second paper.

The PIXE micro-maps were performed by the author of this thesis under the supervision of Dr. W. Przybylowicz at iThemba LABS, the nuclear microprobe facility in Somerset West, South Africa. The data from the "C" – Reef sample was obtained in conjunction with Ms. E. Mbungana. The publication and main ideas were synthesised by the author. Additional technical corrections were made by Dr. W. Przybylowicz, and ideas on fluid components were provided by Prof. J. Kinnaird and Prof. G. R. Drennan.

4.2 PIXE Elemental Maps of Seam Carbon

From the carbon seams examined in Chapter 3, 14 sites were selected for PIXE elemental mapping. Samples that represented average seam carbon forms as well as seams exhibiting unique features that included gold, uraninite and pyrite were examined for elemental variations. Guided by the petrography (Chapter 3 and Appendix C) 4 suitable PIXE maps of carbon seams

were further examined. The four maps in this section, therefore, represent typical elemental distributions and variations within carbon seams. Additional PIXE data obtained for seam carbon samples are shown in Appendix E.

4.2.1 "C" Reef carbon seam in contact with quartz vein

The "C" Reef sample (CREEF01) was taken from a carbon seam that was in contact with a bedding parallel quartz vein. The seam carbon in Figure 4.1 was cut perpendicular to the long axis of the spindles i.e. parallel to strike. Rounded spindles are evident enveloping uraninite grains that exhibit varying degrees of fragmentation. It is clear, however, that these fragments comprise particles that would have originally formed a rounded composite grain. The highly fragmented and angular uraninite particles have carbonaceous material separating them, apparently displacing the fragments of uraninite.

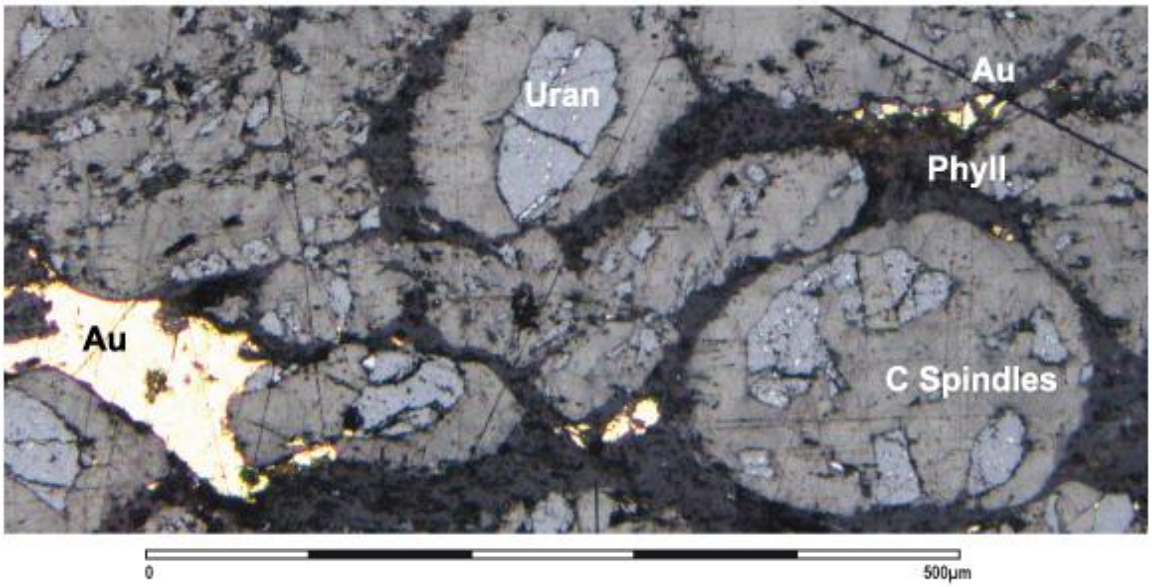


Figure 4.1 Reflected light image of carbon spindles and gold analysed in CREEF01
Scanned region of a carbon seam in contact with a quartz vein from the "C"- Reef from Blyvooruitzicht Gold Mine in Carletonville. The rounded spindles (C Spindles) contain fragmented uraninite grains, between the spindles is a phyllosilicate matrix (Phyll) and interstitial gold (Au).

The sample also contains abundant gold in between the spindles. There is also abundant silicate minerals between the carbon spindles - these fine grained minerals included sericite/muscovite, chlorite, chloritoid and pyrophyllite. The PIXE micro-maps (Figure 4.2) shows the distribution of

elements throughout the seam carbon and inter-spindle material. The silicate material between the spindles contains Al, Si, Fe and K associated with phyllosilicate minerals. The concentrations of Cr indicate muscovite with Cr inclusions. Interestingly, there are small areas enriched in Ni and Y. However, there is little S associated with other elements in the minerals between the carbon spindles. The presence of Y indicates the possible presence of micro-xenotime crystals in the phyllosilicate matrix.

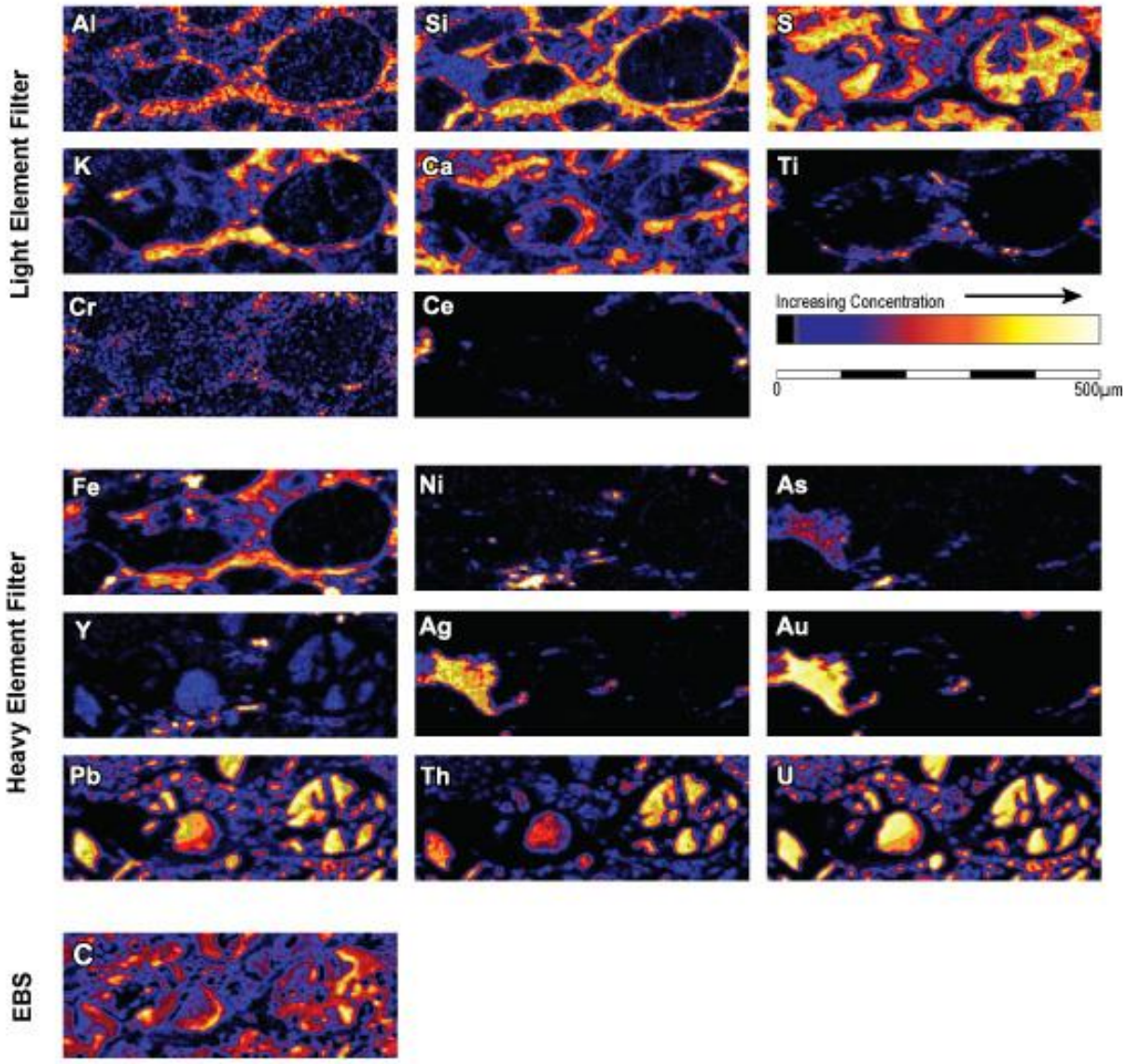


Figure 4.2 PIXE elemental micro-maps of CREEF01
PIXE micro-maps of elements within CREEF01 sample, detected using GeoPIXE and the DA methods. The carbon map was obtained using EBS method.

Sulphur is strongly concentrated and disseminated throughout the carbonaceous material, which cannot be seen in petrographic images. The EBS micro-map of "C" – Reef confirmed the occurrence of dispersed S in the C. Gold in the sample was strongly concentrated in between the spindles and occurs with As and Ag. Notably, S was absent in the areas containing Au. Some carbon spindles displays rims enriched in Ce. Ti also occurs in these Ce-rich regions, these regions were also enriched in uranium, which indicated brannerite was possibly dispersed around the carbon spindles. The uraninite fragments exhibited a strong association with U, Pb and Th occurrences.

4.2.2 CLR carbon seam cross-cut by calcite veinlets

Maps showing carbon spindles in section (Figure 4.3) with calcite veinlets cross-cutting the spindles.

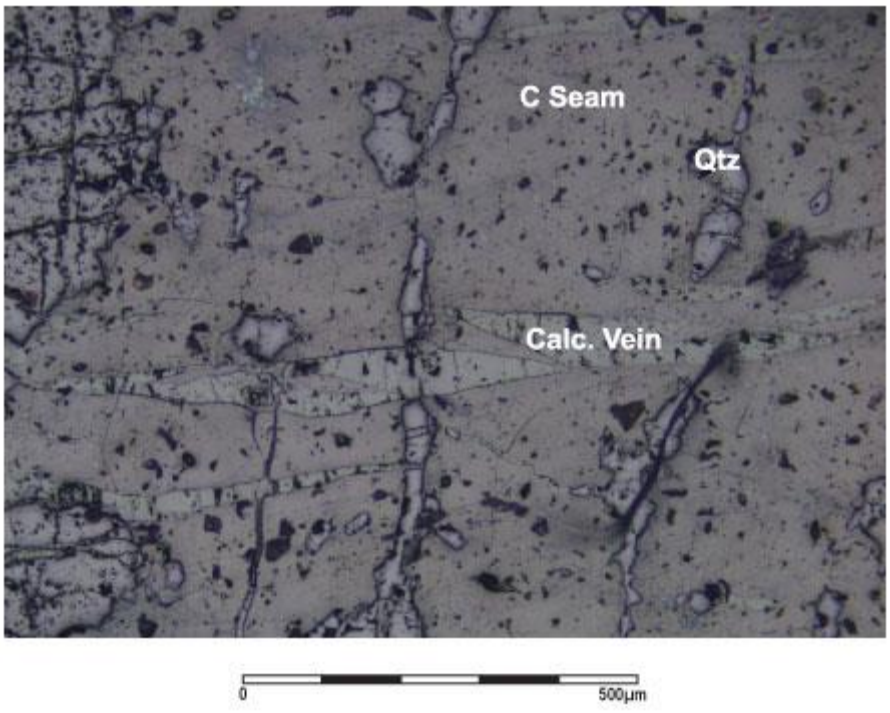


Figure 4.3 Reflected light image of carbon seam cut by calcite veinlets in DFN10
Calcite veins cutting through the C Seam and quartz inclusions in the CLR from Doornfontein Gold Mine in Carletonville. There are small inclusions of micron-scale phyllosilicate minerals between the fractures in the quartz on the left of the image.

The carbon spindles contain small concentrations of S, Cl and K disseminated throughout the carbon seam (Figure 4.4). There are also significant concentrations of Ti and V in lineaments along the spindles of the carbon and there are no particulate minerals associated with these concentrations. Between the spindles Si concentrations are associated with quartz and minor phyllosilicates.

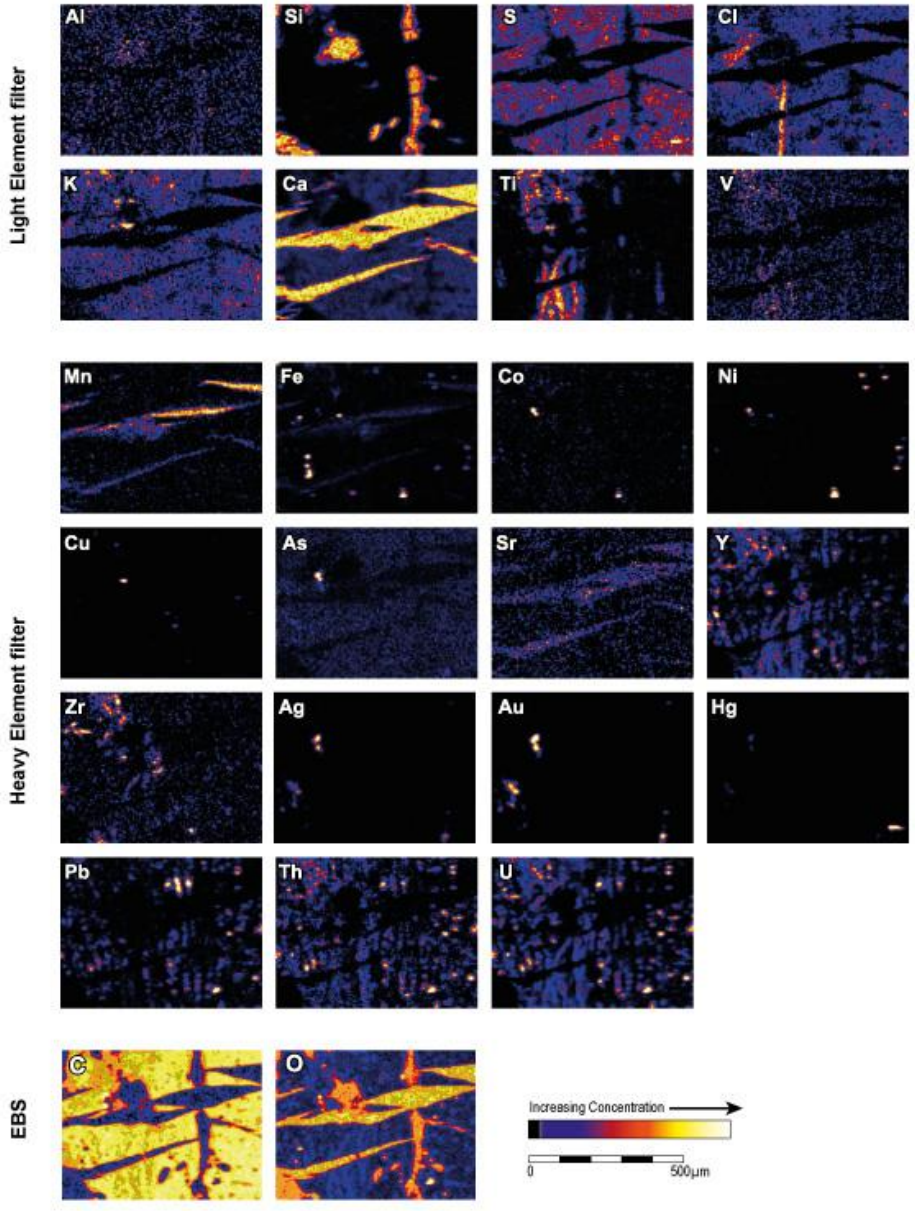


Figure 4.4 PIXE elemental micro-maps of DFN10
PIXE micro-maps of elements within the DFN10 sample, obtained using GeoPIXE and the DA method. The carbon and oxygen maps were obtained using EBS method.

The most prominent feature of the sample is the carbonate veinlets that cross-cut the sample. The veinlets contain very high concentrations of Ca, and small concentrations of Mn, Fe and Sr. The sample contains small rounded concentrations of Pb associated with galena, and Y, Pb, Th and U associated with fragmented uraninite. There are a few rounded concentrations of Co, Ni, Cu, and As associated with cobaltite/gersdorffite. Small concentrations of Au are associated with Ag and Hg. Additionally, strong concentrations of Zr are dispersed to the left of the sample, and these are likely associated with zircons that are not identifiable in petrography.

4.2.3 Basal Reef carbon spindles

Sample LGM3 was taken parallel to the spindles of a carbon seam (Figure 4.5). The sample displayed multiple carbon forms – small nodules were enclosed by spindles of the carbon seam.

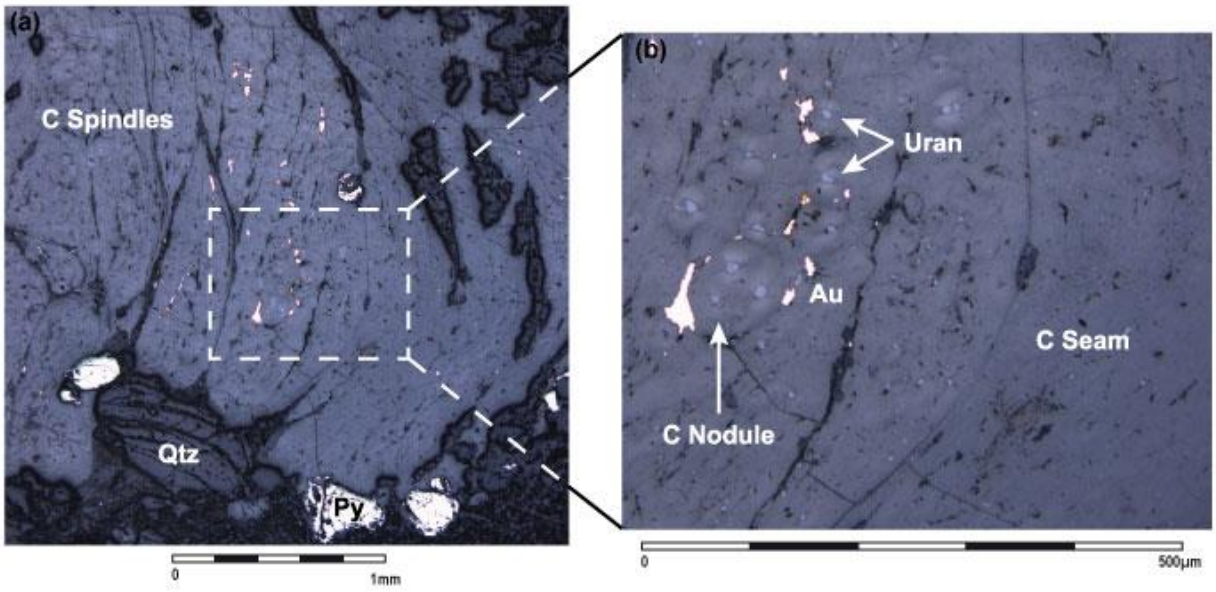


Figure 4.5 Reflected light image of elongated carbon spindles in LGM3
Reflected light optical microscope image of the Basal Reef sample from Lorraine Gold Mine in Welkom. (a) The sample was taken parallel to the elongated axis of the spindles in the carbon seam, with quartz (Qtz) and pyrite (Py) grains at the base of the seam. (b) A zoomed in view of one of the spindles revealed rounded carbon nodules enveloped by the spindle. There was a number of uraninite grains (Uran) and gold (Au) within the enclosed nodules and the spindles.

As with previous carbon seams, PIXE micro-maps (Figure 4.6) carbon seams exhibits high concentrations of disseminated S. Within the seam high concentrations of Cl between the carbon spindles are associated with phyllosilicate minerals. There are diffuse concentrations of K within the carbonaceous materials seemingly not associated with a mineral. There are a number of Ca concentrations associated with a particulate mineral that is not identifiable from petrography.

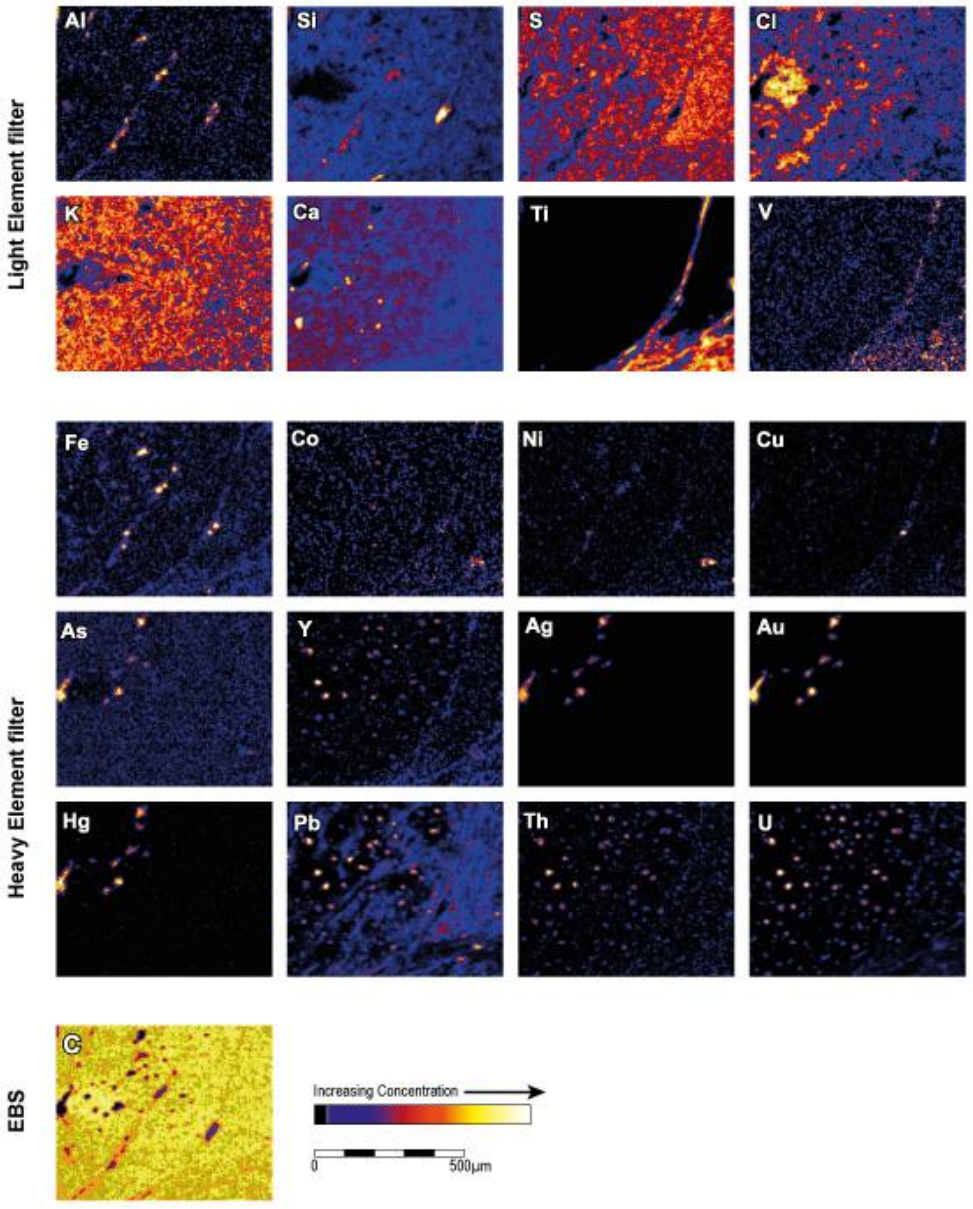


Figure 4.6 PIXE elemental micro-maps of LGM3
PIXE micro-maps of elements within the LGM3 sample obtained using GeoPIXE and the DA method. Carbon map obtained using EBS method.

The most prominent elemental feature of this sample is the thin, intense Ti lineaments, best seen in the between two adjacent carbon spindles. Strongly concentrated along with the Ti in-between the spindles is V and Fe with some minor Cu. While the Fe and Cu is likely concentrated in micron-scale sulphide minerals, petrographically it is unclear what phase is associated with the Ti and V. Gold in this sample was associated with As, Ag and Hg, and is aligned parallel to the adjacent carbon spindles. Gold mineralisation does not, however, occur in the same space between the spindles as the concentrated Ti and V. Additionally, gold is completely surrounded by hydrocarbon. This is in contrast to the "C" Reef sample (Figure 4.2) where gold is strongly concentrated between the spindles. The small, rounded Pb, Th and U concentrations are associated with the uraninite grains in the carbon seam. In this sample the uraninite grains occur as small fragments with relatively angular edges, which is very different from the larger fragmented rounded uraninite in the "C" Reef sample (Figure 4.1).

4.2.4 Vaal Reef carbon spindles and fractured pyrite

Sample MGS6512, from the Vaal Reef, contains a carbon seam less than 1 mm thick from the Vaal Reef. The area analysed using PIXE encompasses a perpendicular section through an oblong carbon spindle (Figure 4.7). The area analysed using PIXE encompasses a perpendicular section through an oblong carbon spindle. The analysed area only contains a small amount of Si (associated with quartz and phyllosilicates) in between the carbon spindle (Figure 4.8). The distribution of the silicate minerals show that the larger carbon spindle is made up of a number of smaller spindles. The carbon spindles contain high concentrations of disseminated P, S (especially towards the edges of the spindles). Ca is associated with the fractured irregular grains of uraninite are associated with strong concentrations of Y, Pb, Th and U. These elements are also dispersed at low concentrations throughout the carbon seam. The carbon spindle also contains minor concentrations of dispersed Mn, Ni and Y (again these concentrations do not appear to coincide with a mineral phase).

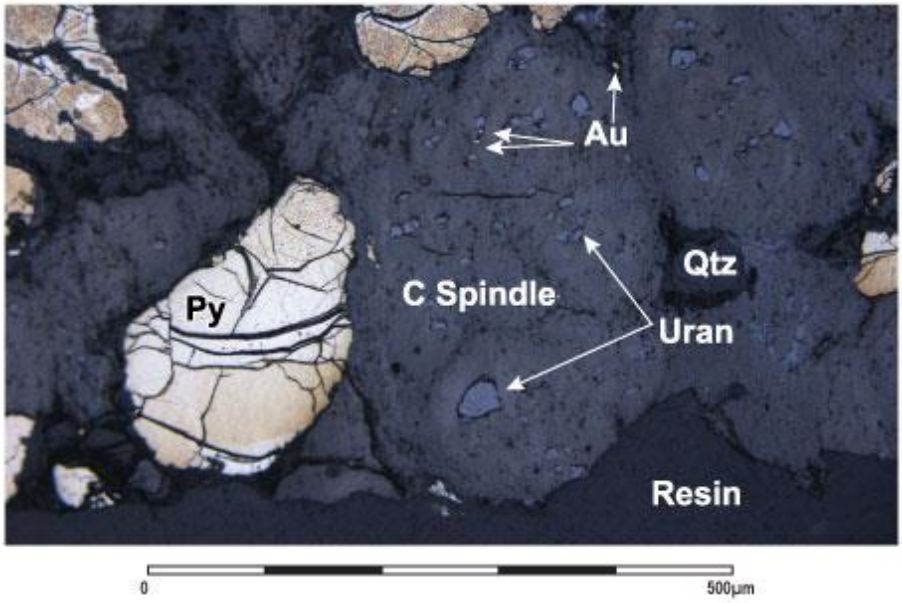


Figure 4.7 Reflected light image of rounded carbon spindles formed around pyrite in MGS6513
Reflected light optical microscope image of the Vaal Reef sample from Hartebeesfontein Gold Mine in Klerksdorp. This ore block sample contains rounded spindles cut perpendicular to the long axis of the spindles. The hydrocarbon surrounds large pyrite grains (Py) and quartz (Qtz) between the spindles. There is a small amount of resin from the preparation of the ore block. Within the carbon spindles (C Spindle) are abundant uraninite grains (Uran) and small amounts of gold (Au).

There are isolated high concentrations Cu and Zn, likely associated with sulphide minerals. A single gold grain illustrated by the high Ag and Au concentrations occurs within the carbon seams. Once again there are very low grade disseminated occurrences of Au and Ag throughout the carbonaceous material. The carbon spindle has a rim enriched in Ti and V, although from the petrographic image it is unclear whether these indicate the presence of rutile or the elements are disseminated within the carbonaceous matter.

Rare Earth Elements (REE) are confirmed within this sample and occur within the Y-rich regions. It is possible that the REE are associated with micro-xenotime crystals. However, it is difficult to identify exactly which REE are present, due to the sub-micron and disseminated occurrences, PIXE spectra do not always resolve the presence of REE completely. Region analyses, presented in Appendix E, provide positive identification of a number of REE including: Ce, Pr, Nd, Pm, Gd, Dy and Er.

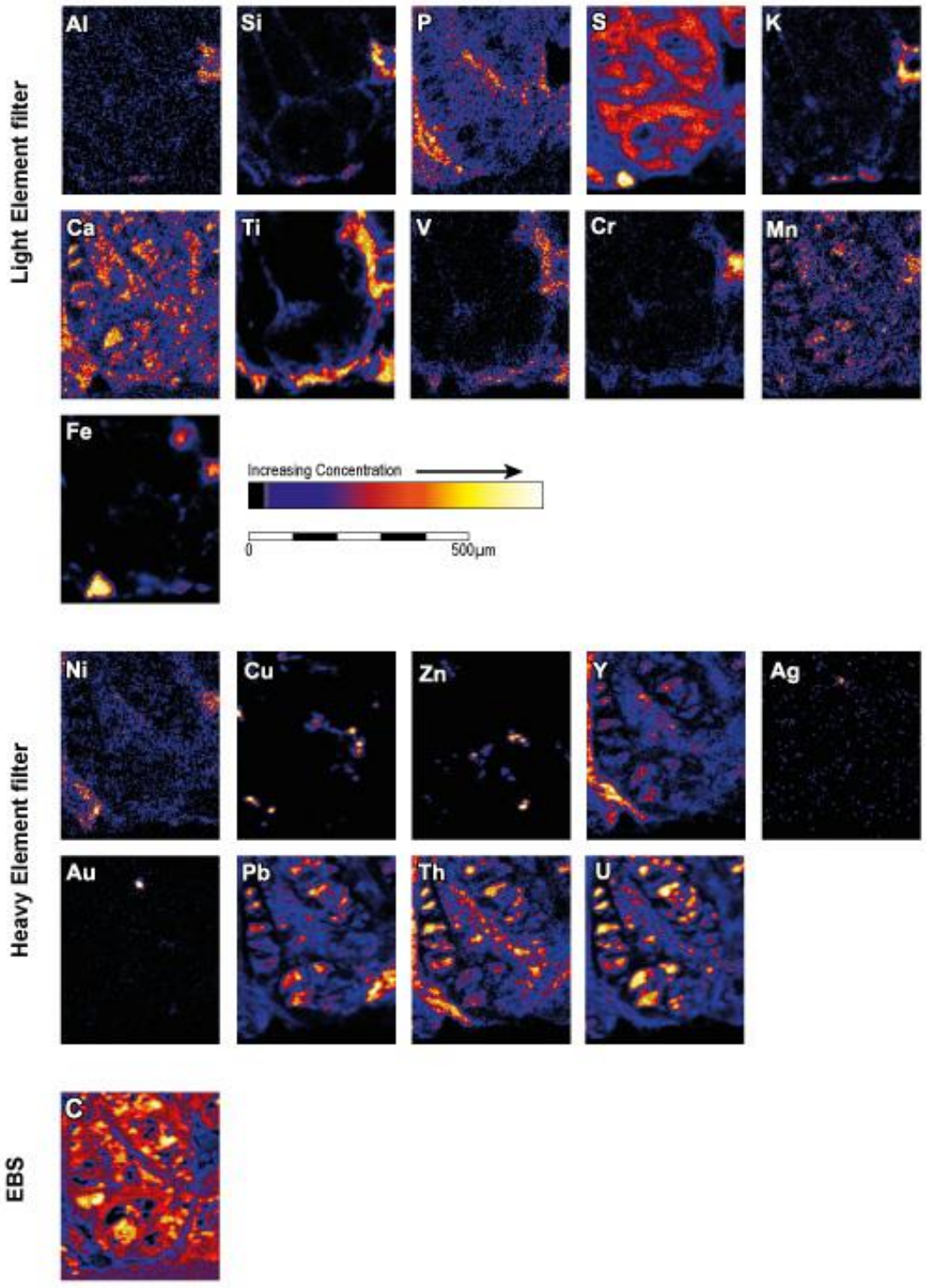


Figure 4.8 PIXE elemental micro-maps of MGS6513

PIXE micro-maps of elements within the MGS6513 sample, obtained using GeoPIXE and the DA method. Carbon map obtained using EBS method.

4.3 PIXE Study of Elemental Distribution within Carbon Nodules

Nodular carbon has a different form to seam carbon, and it is of interest to determine whether element distribution in carbon nodules is significantly different from seam carbon. Nodules can be irregular or rounded and in general contain far less visible gold, pyrite and uraninite. In order to ascertain the reason for these differences three nodular samples (see Section 2.4) were examined using PIXE micro-maps.

4.3.1 Steyn Reef carbon nodules with uraninite grains

The nodular carbon sample (PSGM) occurs around a rounded uraninite grain in the Steyn Reef from the Welkom Gold field. The sample is comprised of multiple rounded and elliptical carbon nodules agglomerated together (Figure 4.9).

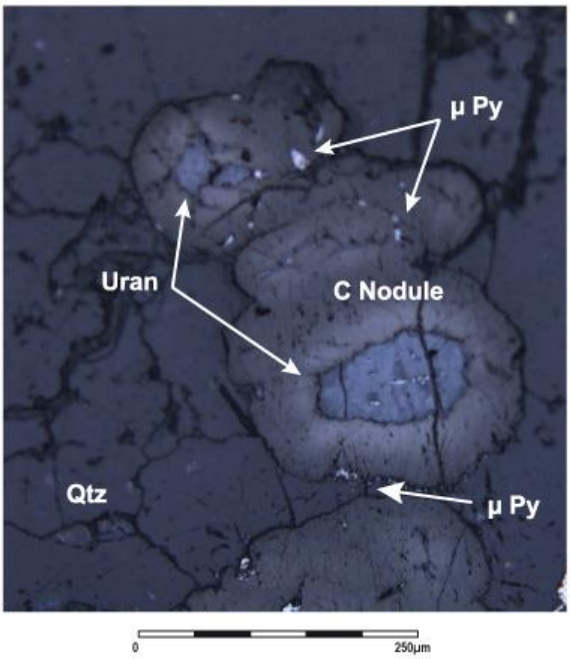


Figure 4.9 Reflected light image of carbon nodules encapsulating rounded uraninite in PSGM
Reflected light optical microscope image of the Steyn Reef sample from President Steyn Gold Mine in Welkom. Rounded carbon nodules (C Nodule) with rounded uraninite grains (Uran.) within them. The nodules occur within interlocking quartz grains (Qtz); there are also a number of micron-scale pyrite inclusions both within and around the rims of nodules.

There is a distinct lack of visible gold in this sample, and there are very small amounts of micron-scale pyrite within the nodules as well as in the rims of the nodules. The largest uraninite grain also contains inclusions of brighter galena, additionally the carbon nodule around the uraninite is “bleached” by radiation, forming a halo of paler carbonaceous material. The micro-maps in Figure 4.10 shows the distribution of elements in the nodules.

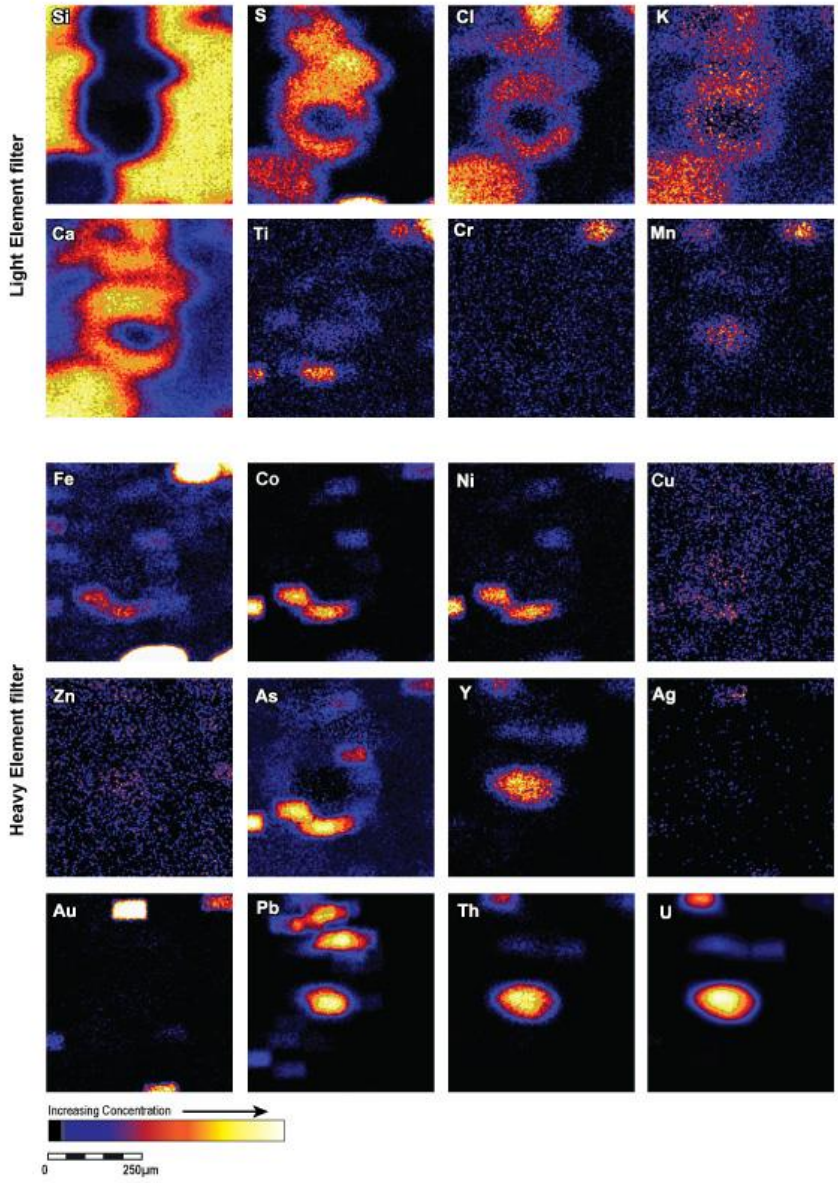


Figure 4.10 PIXE elemental micro-maps of PSGM
PIXE micro-maps of elements within the PSGM sample, obtained using GeoPIXE and the DA method. Carbon map obtained using EBS method.

The nodules contain significant concentrations of S, Cl, K and Ca within the carbonaceous material. The Ca concentration in Figure 4.10 is much higher than previous samples. These nodules are surrounded almost entirely by Si in quartz with no notable phyllosilicate phases are present. There is a small concentration of Cr and Fe associated with small chromite crystals. There are a number of Fe, Co, As and Ni concentrations within the nodules associated with cobaltite, gersdorffite and pyrite inclusions (seen from petrographic image, Figure 4.9). The prominent uraninite, as well as the smaller fragments within the nodules, contain strong concentrations of U, Pb and Th. Additionally, Y and minor Mn are concentrated within the uraninite grains. Au and Ag are also detected in the sample, although not observed petrographically, at the top of the section. The carbon material also contains trace amounts of Cu and Zn dispersed throughout.

4.3.2 VCR carbon nodule

The carbon nodule from the VCR show in Figure 4.11 is unique as it contains very few uranium-bearing minerals compared to typical carbonaceous samples examined.

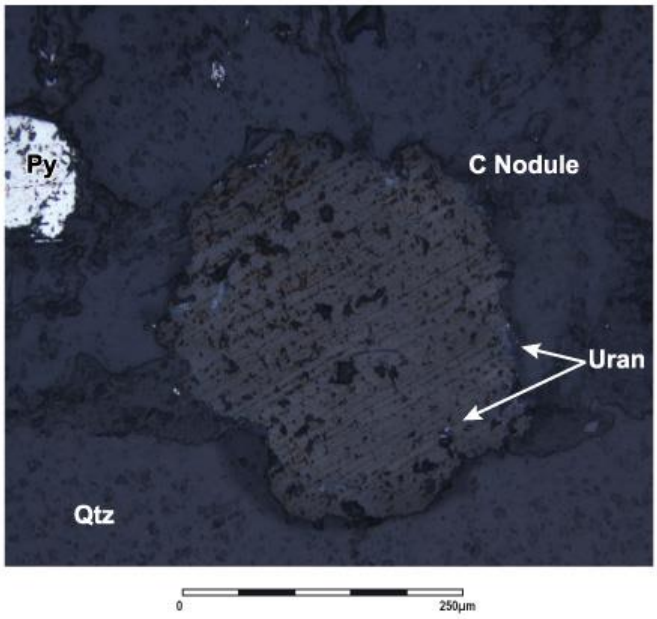


Figure 4.11 Reflected light image of carbon nodule in the VCR1
Reflected light optical microscope image of a carbon nodule in large pebble conglomerate of the VCR from Western Deeps Gold Mine in the Carletonville Gold field. There is a small rounded pyrite grain (Py.) near the nodule, but very little else associated with the nodule. Only small amounts of uranium-bearing phases (U) are visible within the carbon nodule.

The nodule is contained within a large pebble conglomerate with only a small rounded pyrite grain in close proximity to the nodule. The PIXE micro-maps of the VCR carbon nodule, in Figure 4.12, highlight the complexity of the small nodule.

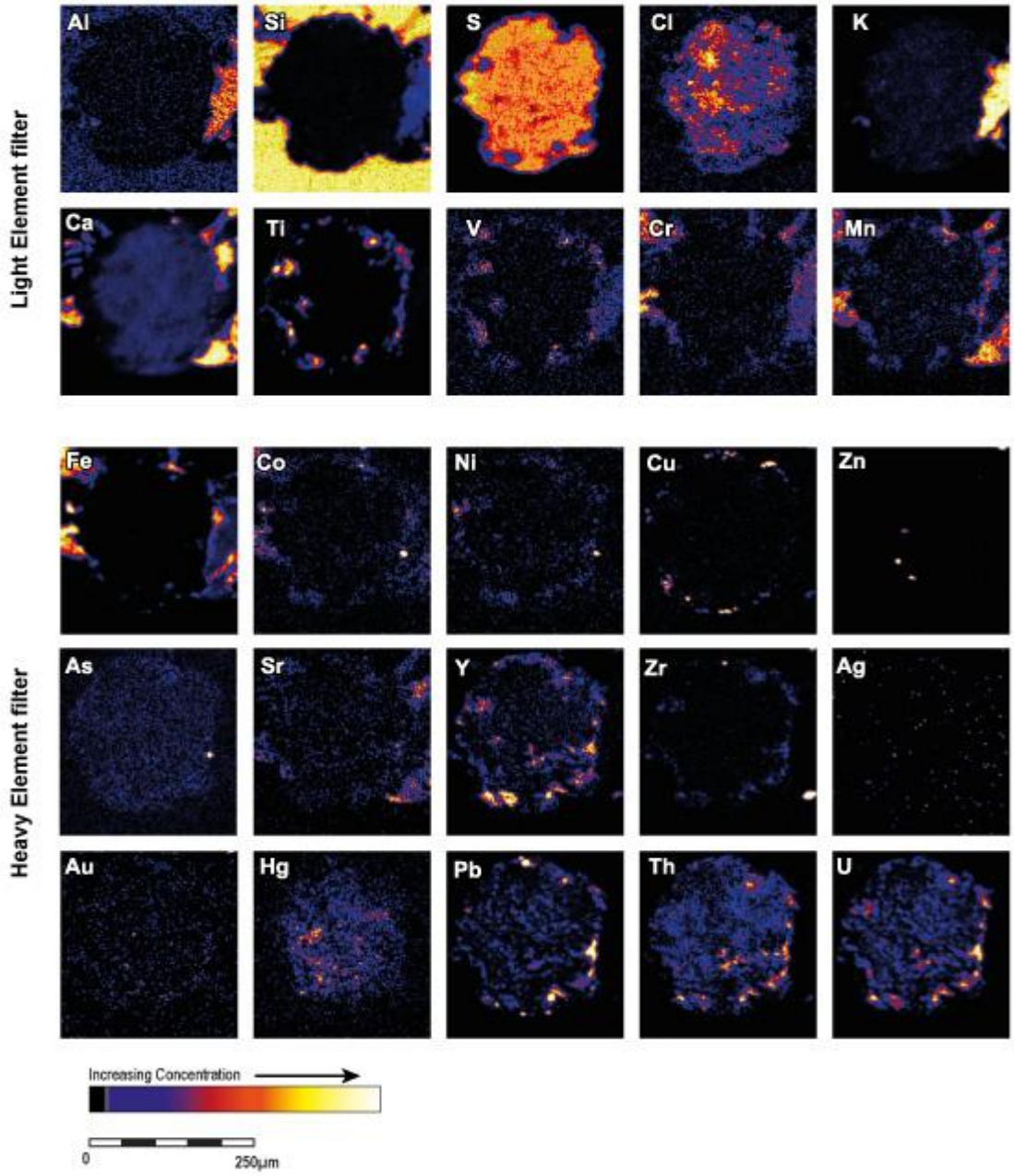


Figure 4.12 PIXE elemental micro-maps of a carbon nodule from the VCR
PIXE micro-maps of elements within the VCR1 sample, obtained using GeoPIXE and the DA method. Carbon map obtained using EBS method.

The carbon nodule is surrounded by quartz, as shown by the strong concentrations of Si. Concentrations of Al, K, Ca and Mn are associated with discrete phases of phyllosilicates adjacent to the nodule. Additionally, Sr is concentrated within the calcite minerals. Within the nodule there are significant concentrations of S, Cl, and Ca disseminated throughout. The rim of the nodule has low concentrations of Ti, V and minor Zr. On the border of the carbon nodule rim there are also significant concentrations of Cr, Mn, Fe, Co, Ni, and Cu, the most intense concentrations are likely in micron-scale sulphide minerals with lower concentrations disseminated in the carbon nodule. There is an abundance of Y, U, Pb and Th around the rim of the nodule as well, some of these elements are concentrated within the micron-scale uranium-bearing phases but most are dispersed within the nodule. The nodule also contains fine and evenly dispersed As, Ag and Au, and a few micron-scale intense concentrations of Zn. Finally, dispersed throughout the nodule are As, Ag and Au.

4.3.3 "C" – Reef porous nodule

The nodule taken from the "C" – Reef is peculiar, in that it has the shape of other nodular forms such as carbon nodules (Figure 4.11), relict uraninite (Figure 3.3) or porous pyrite (Figure 3.16) but it does not have a clear main phase of these minerals. The nodule has a porous form, with a cubic chromite grain further away from it (Figure 4.13). The porous grain contains silicate minerals, brannerite, and pyrite within a quartz matrix. However, it is not clear if this is one mineral (such as a uraninite) replaced numerous secondary phases, or just an amalgamation of numerous fine grained phases. PIXE micro-maps were used to determine the elements concentrated within the nodule (Figure 4.14). Similar to other nodules, the "C" – Reef nodule contains numerous mobile elements. The elements are distributed as both low concentration disseminations and in high concentrations as a rim and a linear feature through the centre of the nodule. Al, Ca and Cl are dispersed throughout the nodule. The linear centre feature contains high concentrations of P, Ca and Sr. Just below the linear feature, there are increased concentrations of Fe and S, associated with pyrite. The rim of the nodule has some concentric

occurrences of increased element concentrations. Ti, Ca and Sr form the inner most rim. The increased Ti content in the rim suggests a phase of rutile or leucoxene within the nodule.

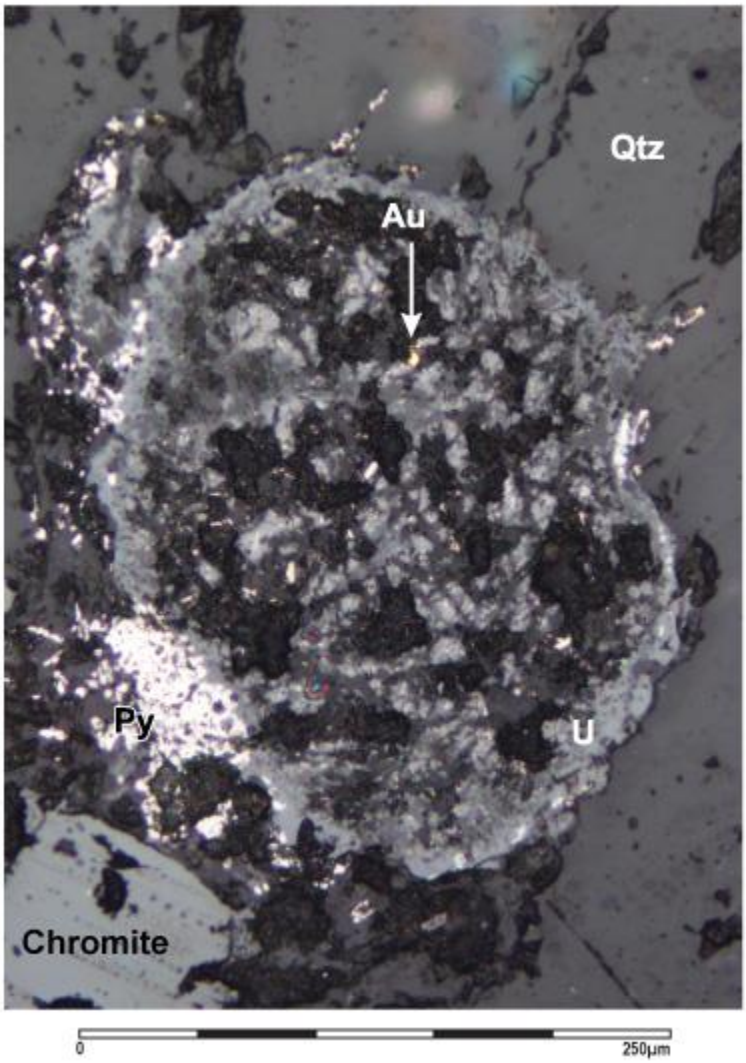


Figure 4.13 Reflected light image of a porous nodule from the "C' = Reef
Porous nodule from containing various fine grained minerals from the "C"- Reef from Blyvooruitzicht Gold Mine in Carletonville. These include brannerite (U), pyrite (Py) and silicate minerals. There is a cubic chromite mineral just next to the nodule, which is contained within a fine-grained quartz matrix.

Surrounding this is a rim of S, Fe, Co, Ni and As, with a very high concentration of the elements in the bottom-left associated with cobaltite/gersdorffite. The two rims are then surrounded with al, Si and Cl, associated with the silicate matrix. Throughout the inner nodule, Ba, Ce, La and Nd are also prominent. The nodule contains an incipient fracture filled with Ca and Sr that could indicate the presence of a carbonate veinlet.

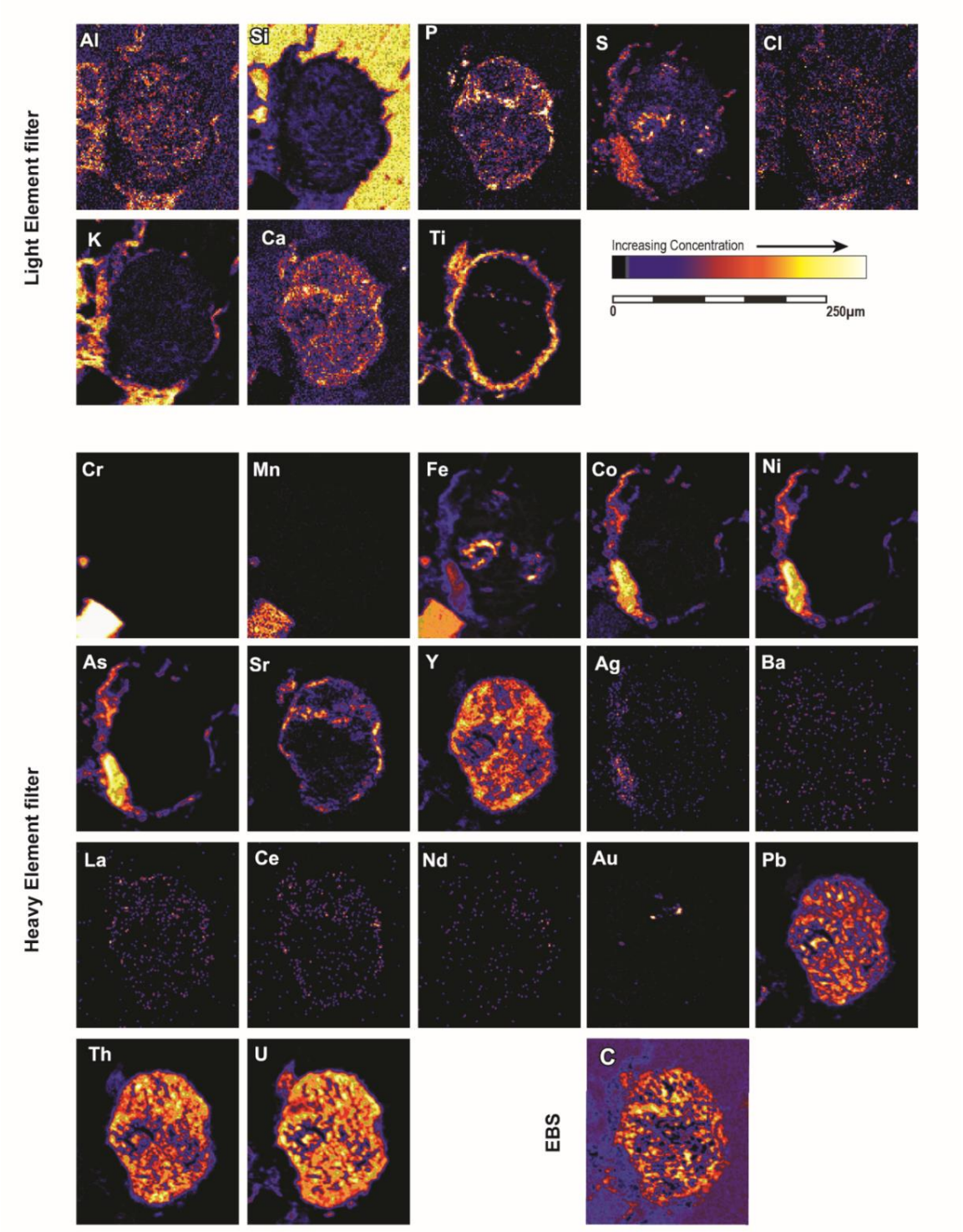


Figure 4.14 PIXE elemental micro-maps of "C" – Reef nodule

PIXE micro-maps of elements within the "C" –Reef porous nodule sample, obtained using GeoPIXE and the DA method. Carbon map obtained using EBS method.

This is in contrast to the seam materials, REE concentrations were much lower (see Region Analysis Appendix E). This nodule confirms relatively high concentrations of REE compared to

carbon seam maps (see above). In contrast to other samples though the porous nodule contains intense concentrations of Y, U, Pb and Th as the dominant concentrations.

These radiogenic elements are surrounded in the petrographic image (Figure 4.13) by another grey mineral phase, which in the EBS image correlates to C. Again the form of C is quite different to the previous nodules analysed. Finally, small concentrations of Ag are dispersed throughout the nodule (with increased concentrations in the gersdorffite portion). Drastically different from the seam carbon micro-maps, Ag is seemingly decoupled from the intense Au concentrations in the centre of the nodule.

4.4 PIXE Discussion

Due to the complex distributions of elements in both seam and nodule carbon, more detailed analyses were carried out on regions of high concentration to verify the elemental distributions of small areas. PIXE spectra from these regional analyses were fitted using a full nonlinear deconvolution procedure (see Appendix E & F). This provided quantitative data on elemental concentrations in these regions. It should be noted that attention was principally given to the distribution patterns of elements and supplemented by the quantitative results. This was in order to characterise the elements that have associations and interactions with the carbonaceous matter examined. The qualitative data does also provide some indication of the concentrations of elements within carbon, which confirms the data published from other reefs (Reimold *et al*., 1999; Fuchs *et al*., 2016a). Additional confirmation of PIXE micro-maps was attempted using WDS from EPMA. However, this technique proved inefficient compared to the PIXE technique that was confirmed using the region analyses described above (see Appendix G).

The most notable feature of the carbon seam material analysed is the variability in elemental distribution between localities within a sample as well as between samples from different stratigraphic horizons within the Basin. What is observed on the PIXE micro-scale is reflected the macro-scale where researchers have noted that gold grades, uranium content and pyrite

concentrations vary considerably within any given reef (Feather and Koen, 1975; Smith and Minter, 1980). Carbon seams themselves are discontinuous over a larger area (Gray *et al*., 1998).

Uranium within the carbonaceous materials is associated with (I) rounded uraninite grains that appear fragmented due to carbonaceous materials between fragments, as (II) secondary brannerite and coffinite contained within the silicate material and (III) as micro-scale inclusions in the seam and nodular materials. Pb within the uraninite is likely due to the radiogenic decay of U into Pb, but also occurs as inclusions of galena (seen as brighter specks in uraninite). It is therefore argued that detrital uraninite grains formed the precursor onto which the gold-bearing carbon seams were deposited.

Gold is most concentrated between carbon spindles but also occurs as micro-particles within the carbonaceous matter. The shape of the gold and the occurrence between spindles indicate remobilisation. Gold between spindles exhibits a single interstitial form with angular edges that indicates recrystallisation of gold.

The carbon seams and nodules have low concentrations of K, Cl, Ca and P, elements which are highly mobile elements and capable of complexing with a variety of metals (Rollinson, 2014). However, the most significant elemental association with C is S. Invariably wherever the carbonaceous matter occurs S occurs disseminated throughout but not as particulate sulphide minerals (seen as pyrite grains separate from carbonaceous materials). Research has found that sulphur is found in abundance in hydrocarbon liquids such as oils (Damste *et al.*, 1987). The inclusion of sulphur in hydrocarbon compounds is theorised to enhance the interactions between hydrocarbons and metals (Damste *et al.*, 1987; Damste and De Leeuw, 1990). This is vital as analyses of crude oils (a product of hydrocarbon degradation and maturation) shows that some metals and REEs are not as soluble in hydrocarbons as other metals are (Section 1.11)

Therefore, it is argued that the forms of carbonaceous materials (seen in Chapter 3), the association of C with S (seen from the micro-maps above) and the dispersed K, Al, Ca and P concentrations indicate that the carbonaceous materials were remobilised as hydrocarbon fluids and precipitated as seam and nodular carbon forms in the presence of detrital uraninite.

Evidence for remobilisation of hydrocarbons (see Sections 1.7.4 & 1.9) supports the view of hydrocarbon migration carrying metals (possibly as an oil). However, the association with S indicates another component. The presence of S and C in a single fluid does provide a potential mechanism for remobilisation wherein the sulphur-containing hydrocarbon in solution is capable of enhancing the solubility of certain elements (Fe, Cu, Ni, Co and other metals). These elements are abundant in higher concentrations in the PIXE micromaps compared to modern crude oils which are depleted in S. It is already known that Au, U, Cr, V, Mn, Ba, Hg, Ag and Ti are present in modern day crude oils (Section 1.10) and that Au , Hg and Ag are also slightly soluble in oils (Williams-Jones *et al*., 2009). Furthermore, the association of S with hydrocarbons can be explained by organic sulphur compounds found in hydrocarbon fluids derived from kerogens (Damste *et al.*, 1987; Damste and De Leeuw, 1990). The effect of the organic sulphur compounds in hydrocarbon fluids is interpreted to have enhanced the ability of hydrocarbons complexing with metals. Thus the effect of hydrocarbons is to transport and deposit metals (with the assistance of organic sulphur compounds) resulting in the unique metal concentrations seen in the Witwatersrand Basin carbonaceous materials.

In addition, multiple mineralisation events are known for the Witwatersrand Basin (see Section 1.9). The carbon nodules enclosed within larger carbon spindles (Figure 4.5) as well as the calcite veins cutting the CLR (Figure 4.3) also demonstrates multiple mineralisation events. In sample DFN10, CO_3-rich fluids concentrated Ca, Mn, Fe and Sr in calcite veins cross-cutting some carbon seams. This concept of multiple fluids was proposed from fluid inclusion studies and was thought to reflect fluid pulses associated with multiple tectonic processes in the Witwatersrand Basin (Stanistreet and McCarthy, 1991; Robb *et al.*, 1997). There is an excellent correlation in the current study with the elements previously documented in PIXE maps of carbon nodules from faults and veins within the Witwatersrand Basin (Drennan and Robb, 2006; Drennan and Robb, 2015). The fluids in the quartz veins contained multiple phases of carbon including carbon in solution/hydrocarbon capable of remobilising elements that can be seen in quartz veins which cross-cut the reefs. Remobilised hydrocarbon precipitated out as rounded nodules containing disseminated and particulate elemental concentrations (Drennan and Robb, 2006; Drennan and Robb, 2015) similar to those described above.

The nodular carbon in this study provides insight to the variable nature of mineralising hydrocarbon fluids from the samples examined. Nodules provide a more detailed view of just how effective these fluids were at remobilising a number of elements, especially as the nodules tend to be isolated from the larger carbon seams (e.g. VCR nodule and "C" – Reef nodule). The nodules contain much higher concentrations of REE than the seam carbons. This is likely to be because REE are more dispersed in the carbon seams compared to the minute carbon nodules. Therefore, the nodules exhibit the ability for a hydrocarbon-rich fluid to remobilise numerous elements, even elements considered to be immobile (Rollinson, 2014). The source of the REE in the hydrocarbon is therefore likely to be close by, most likely as traces within the uraninite, heavy minerals or platinoids (Cousins, 1973) in the sedimentary package. PIXE data suggests, therefore, that hydrocarbon precipitated within the Witwatersrand Basin originated from hydrothermal fluids. A possible source of the hydrocarbon-rich fluid may be the carbon-bearing shales in the lower Witwatersrand sediments - West Rand Group (Fuchs *et al*., 2016a) which themselves indicate a biogenic origin (Mossman *et al*., 2008).

4.5 Conclusions

- PIXE micromaps revealed the association of mobile elements Al, K, P and Ca with hydrocarbons which indicates remobilisation within a hydrocarbon fluid
- Additionally, S was disseminated throughout the hydrocarbons which is indicative of OSC in fluids derived from sedimentary organic materials.
- Gold in carbonaceous reefs was remobilised by hydrocarbon-rich fluids and deposited together with concentrations of As, Ag, Hg
- Dispersed and particulate concentrations of U in carbonaceous seams and nodules that precipitated in the presence of abundant or isolated uraninite grains
- Therefore it is suggested that hydrocarbons transported and deposited metals and elements (such as Au, U, Cr, V, Mn, Ba, Hg, Ag and Ti as well as REE). Further enhancing the model of remobilisation as evidenced in this and other studies, as well as from crude oil data

5 Catalytic chemical vapour deposition of carbon onto uranium-bearing powders to simulate formation of Seam Carbon in Witwatersrand Reefs

5.1 Introduction

Petrography and PIXE provided evidence that complex fluids contained remobilised hydrocarbon and could have precipitated carbonaceous matter onto uraninite grains. However, the precipitation of solid hydrocarbons has previously not been modelled for geological settings such as the Witwatersrand Basin. Limited research shows hydrocarbon precipitation is possible via radiolysis/pyrolysis as demonstrated in the model proposed by Schidlowski (1981). Thus experiments were used in order to simulate carbon vapour depositing onto uranium-bearing phases. This was intended to determine whether it was possible for a gaseous carbon source to precipitate solid carbon onto uranium-bearing mineral grains (See Section 1.9 & 1.7.4). Using the method previously outlined in Section 2.11, uranium-rich granite and meta-sedimentary powder fractions were placed into a quartz boat and heated to various temperatures. The initial experiments were designed in order to determine whether uranium-bearing minerals have the ability to precipitate hydrocarbons.

The results of this Chapter have been submitted for publication as:

Woods, T.H., Drennan, G.R., and Durbach, S.H., 2016a, Simulating U-C Associations: An Experimental Approach to Modelling the Mineralisation Processes in the Witwatersrand Basin, South Africa: Geochimica et Cosmochimica Acta, Submitted.

This Chapter includes data that was not included within the submitted publication due to constraints by the journal. Contributions from the co-authors included the experimental idea, scientific contributions and advice of Prof. S. Durbach and Prof. G.R. Drennan. The experiments detailed in this Chapter, as well as all measurements, were completed by the author of this thesis. Additional assistance was provided by Dr. R. Erasmus with Raman measurements, Mr. N. Pao with TGA analyses, Mr. M. Patchappa with XRF data and Mr. B. Chassoulas and Mr. T. Dzara with

manufacture of the custom-built equipment. Finally, the leaching process and ICP-OES results were provided by Mr. A. Mosai, who had access to the laboratory equipped to safely handle leaching of radioactive materials.

5.2 Product Mass

In order to confirm the composition of the uranium-bearing powders used X-ray fluorescence (XRF) analyses were performed. Two different powder size fractions that represented the average size of uraninite grains (see Section 3.1.1) were used: (i) <32 µm, and (ii) 32-75 µm powders. Table 5.1 shows the uranium concentrations of the powders selected, the powders increase in uranium content with the highest concentration being 7904.27 ppm U for HILG13 <32 µm. Upon closer examination it appeared that the sieving process had affected the concentration of certain trace elements within the powdered fractions (Table 5.1). For instance, powders that were sieved to <32 µm were enriched in uranium as compared to their larger-sized counterparts.

Table 5.1 Powdered substrates placed under CCVD conditions, arranged in increasing uranium concentration per size fraction

<32 µm powders			**32 -75 µm powders**		
Sample	**Source Rock**	**Uranium concentration (µg/g)**	**Sample**	**Source Rock**	**Uranium concentration (µg/g)**
HILG19	Granite	504.77	HILG19	Granite	419.06
DH034	Granite	2445.83	DH034	Granite	1347.55
IDAM10	Meta-sediment	6729.08	HILG13	Granite	3251.84
HILG13	Granite	7904.27	IDAM10	Meta-sediment	5293.85

It was observed that the initial experiments were not always successful. For instance, it was found that powder fractions of 2 mm and greater were only able to precipitate minimal masses of unstructured carbon onto their surfaces. Other issues were also encountered when samples were initially calcined, in order to make sure that all carbon constituents were removed before reactions with the gaseous carbon source were conducted. In some instances it was found that the uraniferous powder samples would produce a loud popping sound after calcination when exposed to gaseous hydrogen and acetylene. This problem was almost completely nullified by

removing the calcination step from the process, after it was determined that the initial carbon content in the uraniferous powder samples was negligible and this process was not required. The most probable reason for the popping sound was likely to have been small explosive reactions between oxygen and hydrogen or oxygen and acetylene. It was suspected that heating uraninite may have forced it to either take up oxygen to become further oxidised or to store it on its surface. Then, after the system was purged with gaseous argon and hydrogen was introduced, it was speculated that this oxygen was released back into the system and reacted with the hydrogen or acetylene. However, after the correct conditions were determined, carbonaceous deposits were successfully deposited onto these powders. This was confirmed both visually (by a colour change i.e. from a grey or red powder to a black one) as well as physically (by a mass increase) as shown in Figure 5.1.

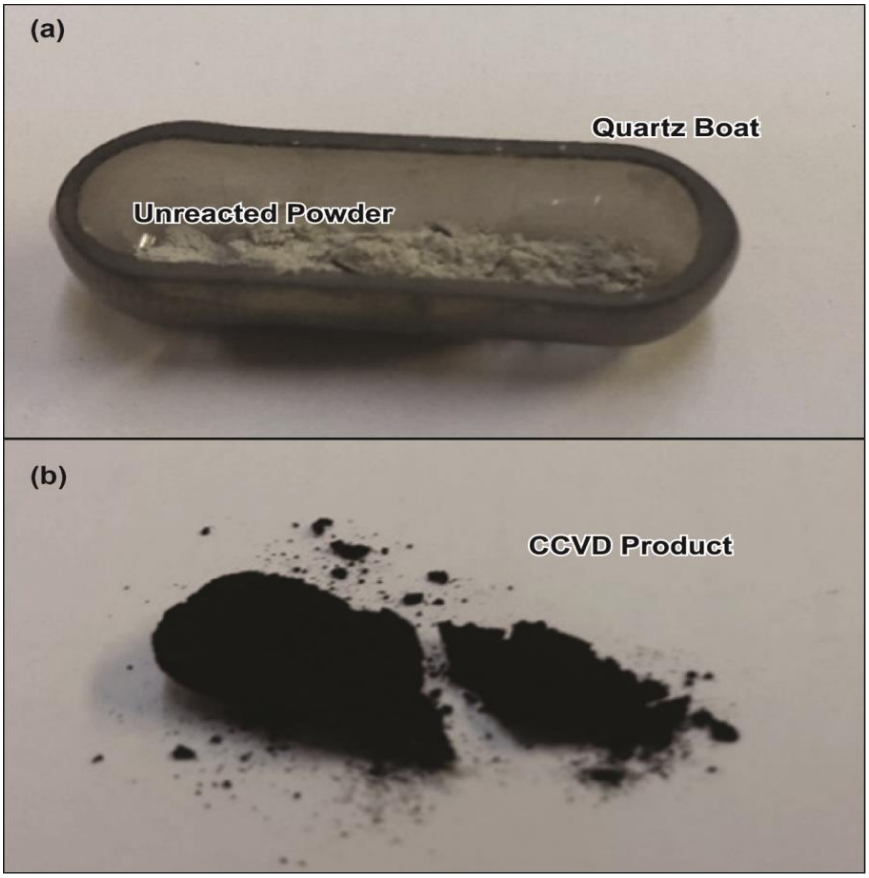


Figure 5.1 Change in appearance of CCVD experimental products
(a) Unreacted grey-coloured unconsolidated uraniferous powder in the quartz boat, (b) After the CCVD reaction at 600°C the uraniferous powder was black-coloured, agglomerated and the mass had increased. The product maintained the rounded form of the quartz boat and was friable.

The quartz boat also shows a discoloration from the deposition of 'soot' onto the surface of the quartz. The amount of carbonaceous materials deposited is negligible (as shown by the consistent weight of the empty boat in Appendix H).

Negligible changes in mass were seen for all uraniferous powders at reaction temperatures of 300°C. When the reaction temperatures were increased to 450°C, the majority of the uraniferous powders changed colour to black and small mass increases were noted. However, the most significant changes occurred at 600°C, where the unconsolidated uraniferous powders became completely agglomerated within a black product and took on the form of the quartz boat at the bottom or became colloform at the unrestricted surface of the boat. Figure 5.1, shows the colour change from the initial unreacted powder to the product that was formed at 600°C. In some cases (e.g. for the HILG 13 powder) the increase in the mass of the black product, formed under CCVD conditions, appeared to have been exponential with respect to the increase in reaction temperature (Figure 5.2).

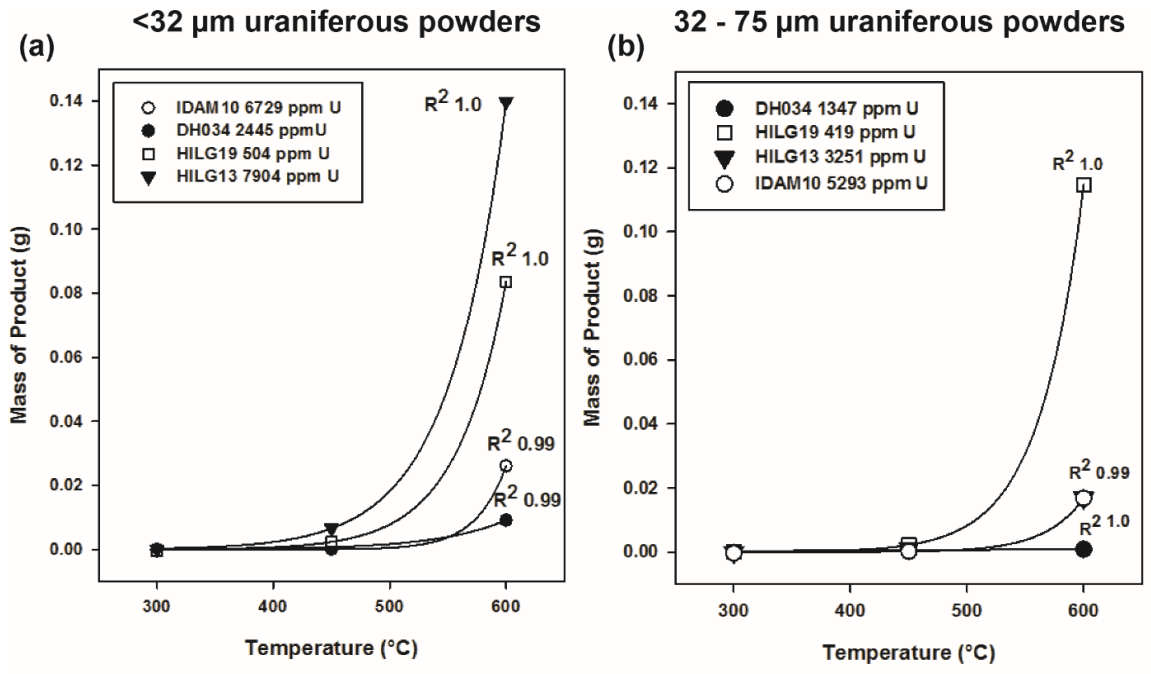


Figure 5.2 The mass of the black product formed during CCVD growth
Mass versus: (a) 32 µm uraniferous powders and (b) 75 µm uraniferous powders, with increasing reaction temperature. Each point on the graph was an average of the three experiments that were carried out for that powder and temperature. Also represented are R^2 values demonstrating the suitability of the curve/line fitted displaying exponential/linear increases.

While reactions with the 32-75 µm uraniferous powders formed substantial masses of the black product, reactions with the <32 µm powders repeatedly resulted in significantly more products and displayed trends that were much more easily differentiated (although not for all samples). Coincidentally, XRF analyses showed that this size range (i.e. <32 µm) had been enriched in uranium by the sieving process (Table 5.1).

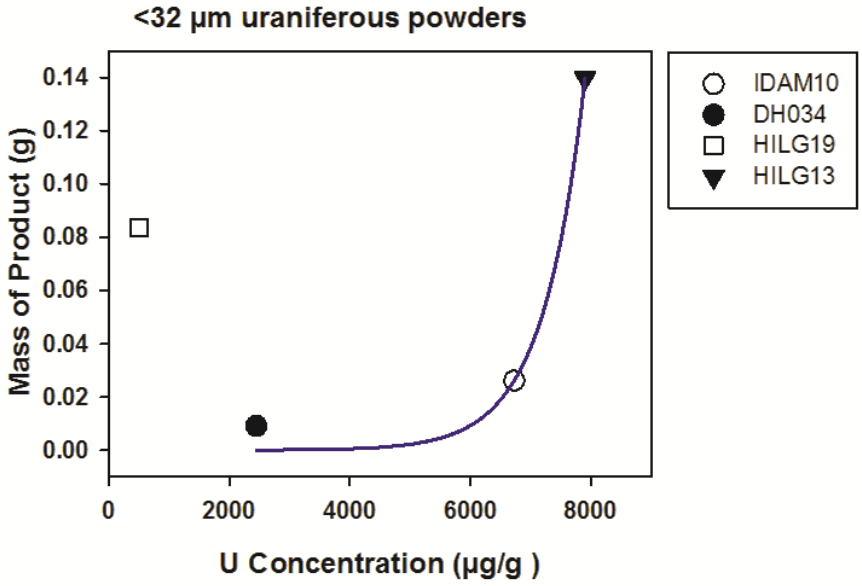


Figure 5.3 The mass of product formed vs Uranium concentration, for <32 µm uraniferous powders from CCVD reactions at 600°C; the line shows the exponential regression for the IDAM10, DH034 and HILG13 data. The HILG19 data is a statistical outlier. Each symbol represents the average of 3 experiments.

Significantly, data obtained at reactions conducted at 600°C suggested that (apart from the HLG19 powder) a positive correlational relationship existed between the concentration of uranium in these powders and the masses of black products that were formed (see regression line on Figure 5.3). Since the HLG19 powder was an outlier (over 3 averaged experiments), an explanation for its variance in the trend was sought at 600°C (lower temperature data shows similar trends in Appendix H). While there were a number of smaller differences in the elemental compositions of the starting uraniferous powders, the most noticeable ones were for the concentrations of: Cu, Mo and Sr (Appendix H). Plots of the mass of black product formed versus the concentrations of: Cu, Mo and Sr can be seen in Figures 5.4 – 5.5 respectively.

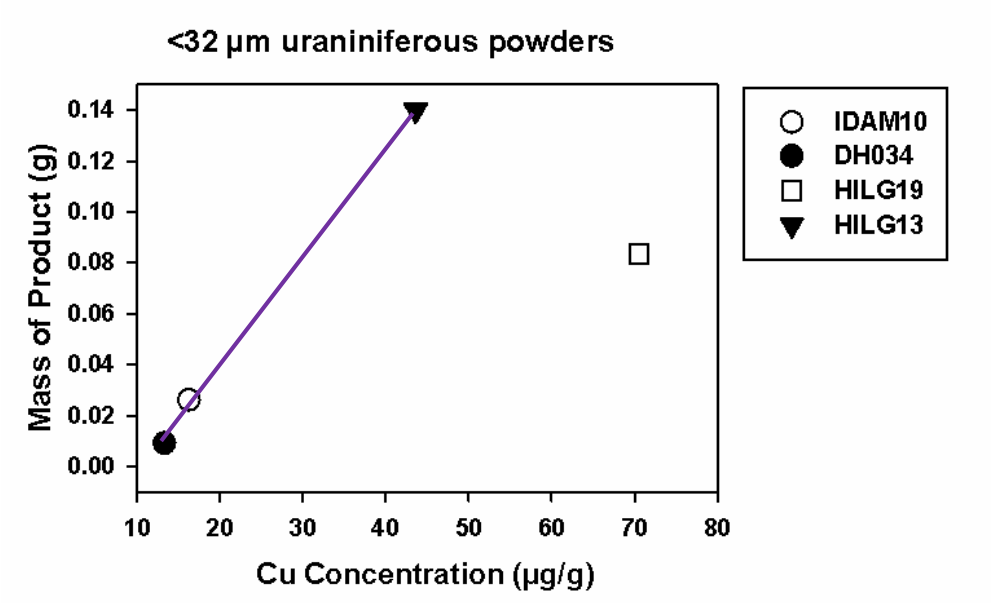


Figure 5.4 The mass of product formed during the CCVD reaction with <32 µm uraniferous powders at 600°C, versus the concentration of Copper. The fitted line demonstrates the observed trend if the HILG19 data, a statistical outlier is considered separately.

It was noted that predominantly positive correlational relationships were observed between the concentrations of Cu, Mo and Sr, and the masses of black product formed for the <32 µm powder fractions at 600°C. Figure 5.4 and Figure 5.5 show that both Cu and Mo were positively correlated and the highest value for each of those graphs was obtained for the HILG19 powder. Figure 5.5 shows a similar case except here the relationship was more linear, with no outliers. Further evidence for this can be seen for the 32 – 75 µm powders versus mass formed seen in Appendix H. Therefore further investigation was required to establish the contribution of uranium towards the formation of the black products. A small portion of the HILG19 <32 µm powder was exposed to conditions where uranium was leached from it and then reacted under CCVD conditions at 600°C. The resulting powders had a similar visual appearance to that of the uranium enriched HILG19 powders. However, for the HILG19 <32 µm leached uranium, where almost 50% of the U had been leached out the mass of black product that formed was about 35% less than the original unleached powders (Table 5.2).

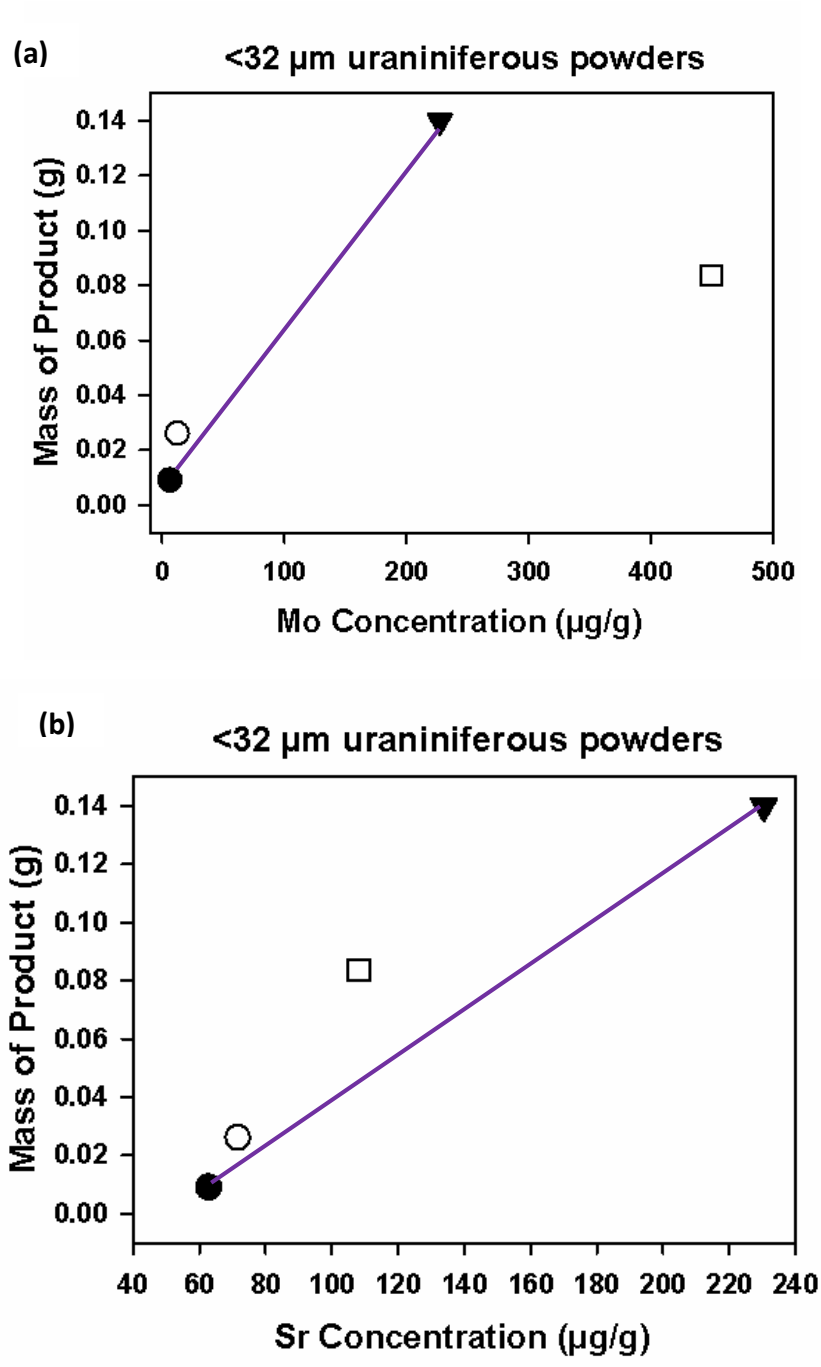


Figure 5.5 The mass of product formed during the CCVD reaction with <32 µm uraniferous powders at 600°C, versus the concentration of (a) Molybdenum and (b) Strontium. The fitted line demonstrates the observed trend if the HILG19 data, a statistical outlier is considered separately.

This strongly suggested that uranium played a key role in the formation of the black products, since the other elements (that might have played a major role in the precipitation of black product) were leached by significantly lower quantities: Cu (0.6%), Mo (2.1%) and Sr (1.1%) (See Appendix H).

Table 5.2 Product masses of standard HILG19 powders compared to those in which U had been leached.

HILG19 <32 µm powder	
U concentration (µg/g)	**Average amount of black product formed**
Original Powder	
831	0.0836 g
After leaching	
429	0.0544 g

5.3 Laser Raman Spectrometry

The significance of the reaction temperature and the nature of the black products formed onto the uraniferous powders were investigated through laser Raman spectroscopy (LRS). Spectra from these black products, in Figure 5.6 displayed the characteristic "D" (1350 cm^{-1}) and "G" (1580 cm^{-1}) peaks, associated with disordered and ordered/graphitic carbon respectively (Ferrari and Robertson, 2000; Reich and Thomsen, 2004).

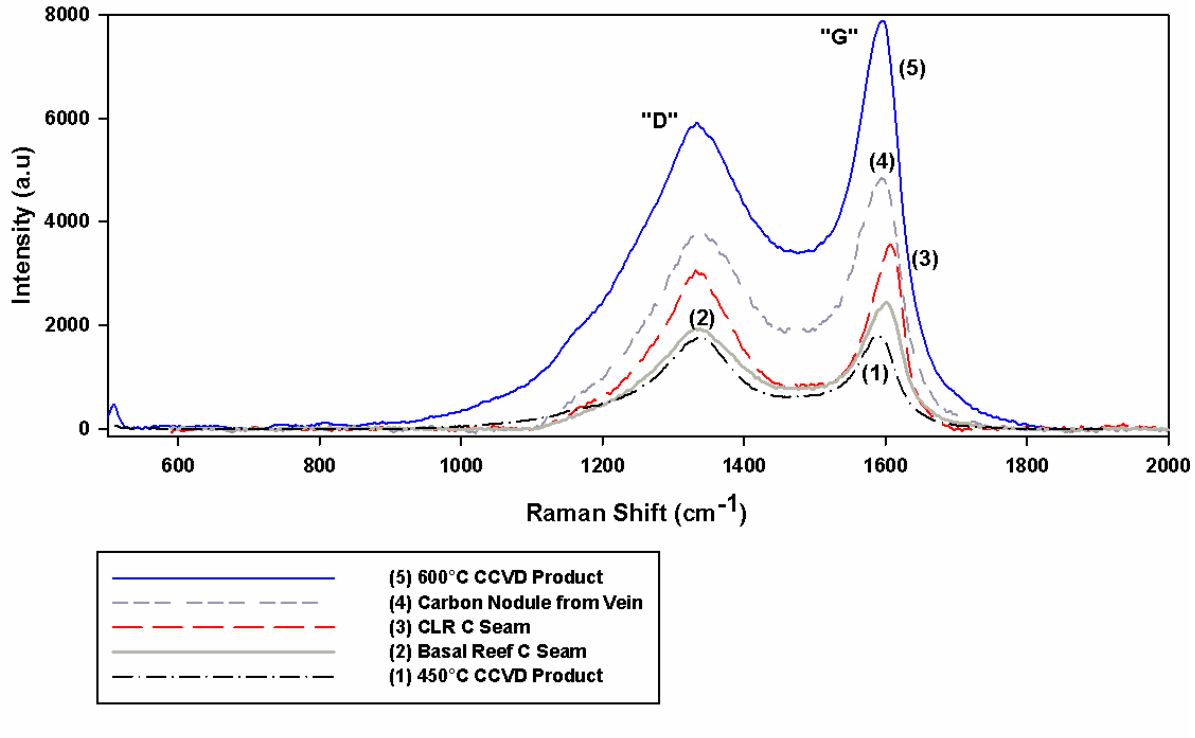


Figure 5.6 Raman spectra of the CCVD experimental products and Witwatersrand Carbon samples
(1) CCVD product from <32 µm HILG19 powder reacted at 450°C; (2) Basal Reef carbon seam powder; (3) CLR carbon seam powder; (4) Carbon nodule from a vug in a quartz vein cross-cutting the Beisa Reef; (5) CCVD product from <32 µm HILG19 powder reacted at 600°C

This confirmed that the black products, which had formed in association with the uraniferous powders, were indeed carbonaceous. These peaks were either too small to clearly differentiate or not present at all at low reaction temperatures i.e. 300°C. This observation was consistent with the negligible mass increases that were found under those conditions. Of interest was the observation that the above-mentioned peaks increased in intensity with reaction temperature and that at 600°C the "G" peaks in these spectra had significantly higher intensities than the "D" peaks. This suggested that the carbonaceous products that were formed under these conditions were more graphitic (and therefore ordered) than those at lower reaction temperatures.

Witwatersrand carbon from the CLR, Basal Reef and a carbon nodule from a vug in a quartz vein cross-cutting the Beisa Reef were also examined using LRS (Drennan *et al*., 1999). Spectra from the CCVD experimental products were compared with those from Witwatersrand Carbon (Drennan and Robb, 2006). It was noted that while the intensities were variable, the peaks were very similar in position to those of the experimental products. The I_D/I_G ratio, which compares the area under the graph for the "D" peak and for the "G" peak, was then compared in Table 5.3.

Table 5.3 Thermal analyses and laser Raman data for the carbonaceous products formed by CCVD at 450°C and 600°C as compared with laser Raman data for Witwatersrand Carbon.

	450°C CCVD Products		**600°C CCVD Products**	
	TGA T°	I_D/I_G	*TGA T°*	I_D/I_G
IDAM10, <32 µm	580	0.85	640	1.04
DH034, <32 µm	N/A	0.77	620	0.90
HILG13, <32 µm	500	0.80	596	0.93
HILG19, <32 µm	504	0.78	611	1.01
IDAM10, 32-75 µm	N/A	0.89	620	0.96
DH034, 32-75 µm	N/A	0.75	598	0.87
HILG13, 32-75 µm	494	0.78	590	0.99
HILG19, 32-75 µm	514	0.78	523	0.97

Witwatersrand Carbon	I_D/I_G
Carbon Nodule from Beisa Reef	0.81
Carbon Seam from CLR	0.87
Carbon Seam from Basal Reef	0.82

The average I_D/I_G ratio for the Witwatersrand Carbon samples was 0.84 and was similar to the average ratio I_D/I_G for the CCVD experimental products that formed at 450°C i.e. 0.80. This suggested a similarity in the types of carbonaceous materials that were present in both sources. The thermal properties of the CCVD products were then investigated.

5.4 Thermogravimetric Analyses

Thermogravimetric analyses (TGA) were performed on the carbonaceous products that were formed on the HILG19 <32 µm sample at 450°C and 600°C to ascertain their thermal stability and hence their graphitic nature. First derivatives of the TGA data for the carbonaceous products formed at 450°C and 600°C provided the temperature maxima where each of these products combusted (Figure 5.8).

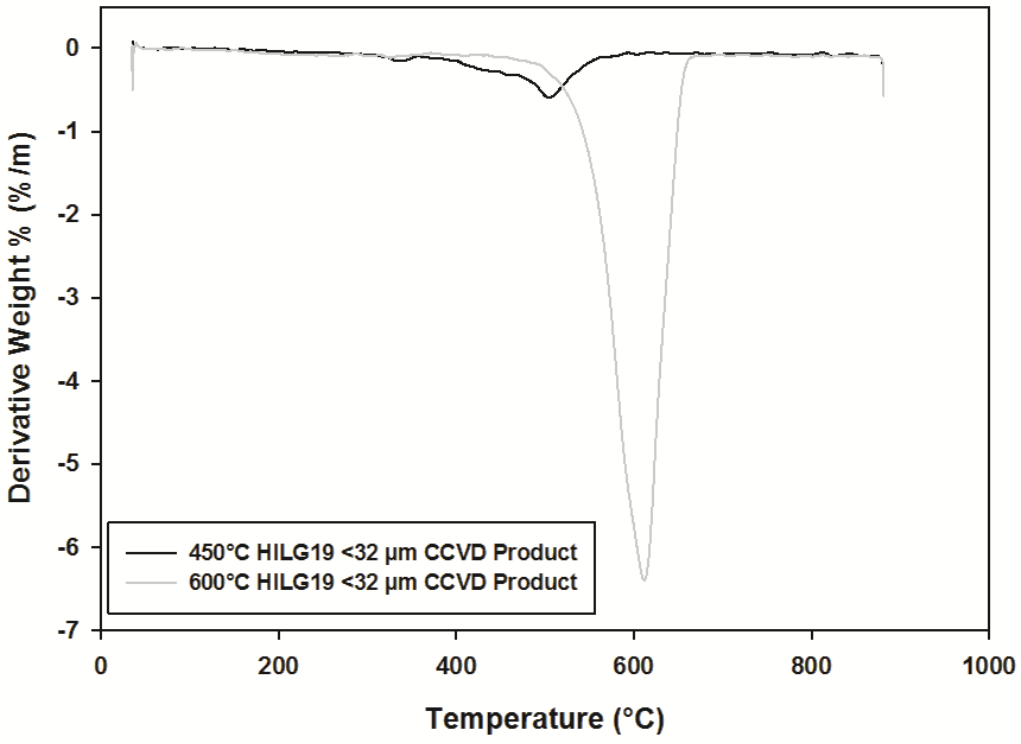


Figure 5.7 The first derivative curve of the TGA analysis of the CCVD products (for HILG19 powders <32 µm) from 450°C and 600°C experiments

Data obtained by the TGA analyses revealed that the temperature maxima of the carbonaceous products formed on the HILG19 powder at 600°C was higher than at 450°C. This suggested that the thermal stability and hence the graphitic (ordered) nature of the products formed from HILG19 <32 μm improved as the reaction temperature was increased. This observation was found to be consistent with that made by LRS and with literature (Ferrari and Robertson, 2000; Ferrari, 2001). Likewise, when the first derivatives of the TGA data as well as the I_D/I_G ratios were compared with one another, this same trend was found for all of the uraniferous powders that were assessed under experimental conditions Table 5.3.

5.5 Transmission Electron Microscopy

Transmission electron microscopy (TEM) was used in order to identify the nature and the quantity of carbonaceous products that were formed during the vapour deposition reactions as compared with the Witwatersrand hydrocarbon materials. Micrographs of the products from: 300°C (Figure 5.8a-b), 450°C (Figure 5.8c) and 600°C experimental products (Figure 5.8d) and Figure 5.9a) revealed that carbon nanostructures (CNSs) had formed on the crystalline particles of the uraniferous powders.

The TEM micrographs revealed that very small quantities of CNSs appeared to have begun to grow from the surface or the subsurface of the uraniferous particles (U) at 300°C (Figure 5.8a & Figure 5.8b). This observation was consistent with the negligible mass increases and poor detections of these materials by Raman spectra under these conditions. CNSs with more discernible structures were far more apparent at 450°C (Figure 5.8c). Fairly uniform-shaped, rough-textured carbon nanotubes/nanofibers appeared to grow from some of the uraniferous particles. Similarly the greatest quantity of carbonaceous products were noted to have been formed at 600°C (Figure 5.8d & Figure 5.9a), which was consistent with previous observations. CNSs that were formed included: sheet-like carbonaceous materials (Figure 5.8d-1), spiral or helical shaped carbon nanofibers (Figure 5.8d-2), carbon nanotubes (Figure 5.8d-3) and complex spiral-shaped carbon nanofibers within larger carbon nanostructures (Figure 5.9a). In each case the CNSs that grew were found to be in direct association with the uraniferous particles.

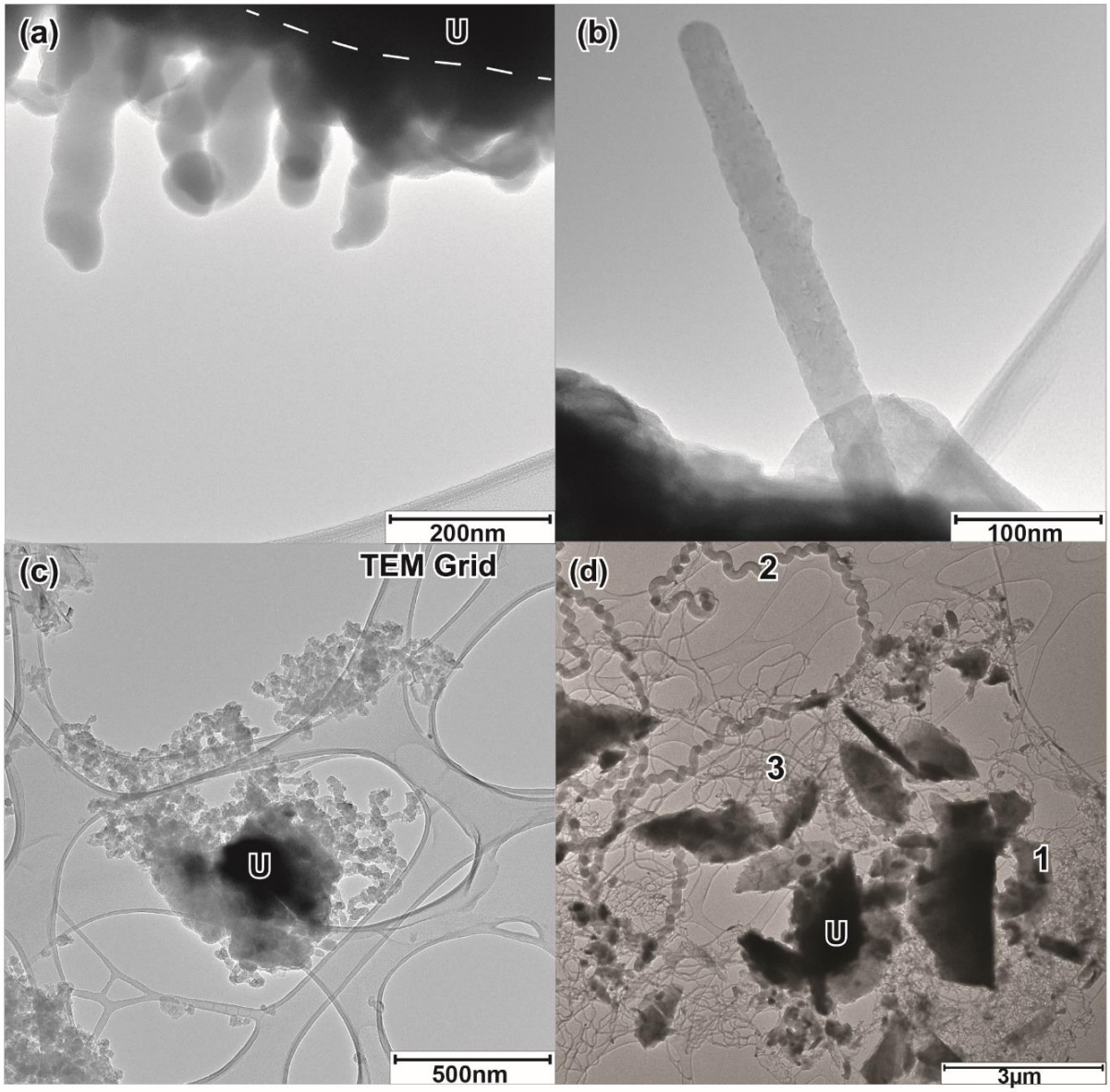


Figure 5.8 TEM micrographs of the CNSs that formed in the CCVD experiments

TEM micrographs of the CNSs that formed in the CCVD experiments: (a) IDAM10 <32 µm CCVD product reacted at 300°C showing small quantities of carbon nanofibers on the surface of uranium-rich grains (U); (b) IDAM10 <32 µm CCVD product reacted at 300°C showing a carbon nanotube emerging from the surface of uranium-rich grain; (c) HILG19 <32 µm CCVD product reacted at 450°C showing uniform rough textured CNSs; (d) HILG19 <32 µm CCVD product reacted at 600°C showing sheet-like carbonaceous materials-1, spiral-shaped carbon nanofibers-2, carbon nanotubes-3. **NOTE:** In each image, the rounded forms in the background represent the lacy copper-carbon TEM grids that samples were mounted on.

The experimental products were also compared to crushed seam carbon from the Carbon Leader Reef (CLR) in the Witwatersrand Basin (Figure 5.9b).

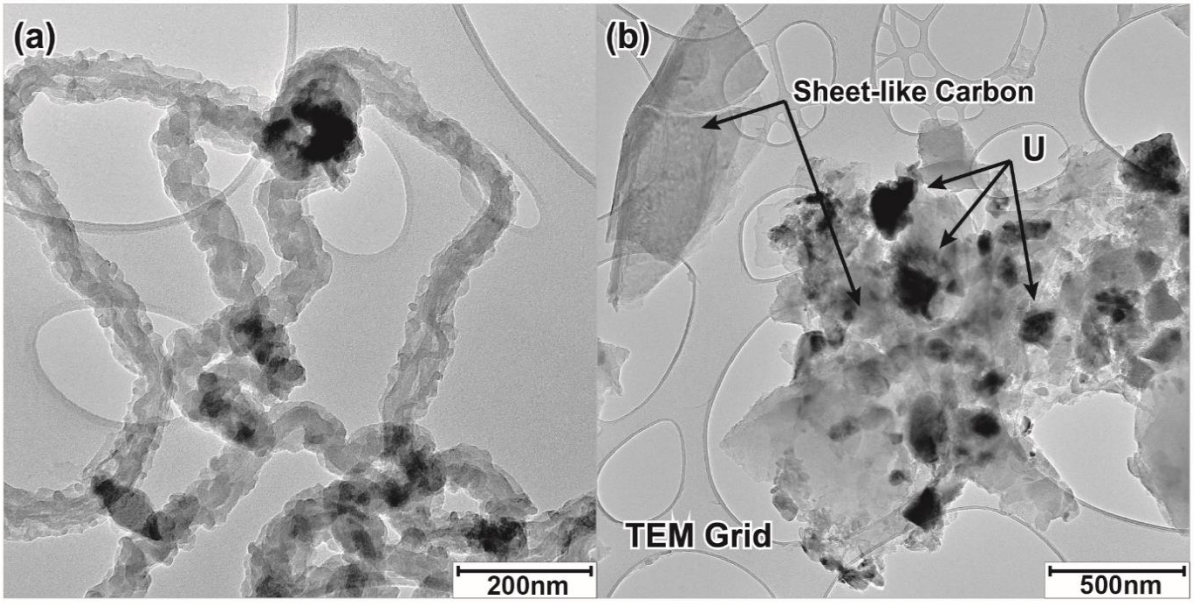


Figure 5.9 Additional TEM micrographs of the CNSs that formed in the CCVD experiments
(a) HILG19 <32 µm CCVD product reacted at 600°C showing complex spiral-shaped carbon nanofibers within larger carbon nanostructures. (b) Crushed CLR sample showing uraninite grains (U) surrounded by sheet-like carbonaceous material. **NOTE:** In each image, the rounded forms in the background represent the lacy copper-carbon TEM grids that samples were mounted on.

Carbon materials that were present in the seam carbon were found to surround the solid uraninite (U) particles (100 – 200 nm), in a manner similar to what was seen in the CCVD products in this study. These carbonaceous materials had a sheet-like form. Whenever an attempt was made to more closely observe these materials in the seam carbon, by increasing the intensity of the electron beam, it was noted that they deformed into rounded globular masses. Similar rounded globular masses were noted when a Raman laser was applied to fluid inclusions rich in hydrocarbon gases, by (Drennan, 1997) where the gasses formed globular nodules after exposure to the laser. Consequently, highly nanostructured carbon (e.g. carbon nanotubes/nanofibers and complex spirals) were not observed in the TEM micrographs of the CLR from the Witwatersrand Basin

When SEM images (Figure 5.10) of an ore block sample from the Beisa Reef (from the Witwatersrand Basin) and the black products formed at 600°C by CCVD were compared, a striking similarity was noticed.

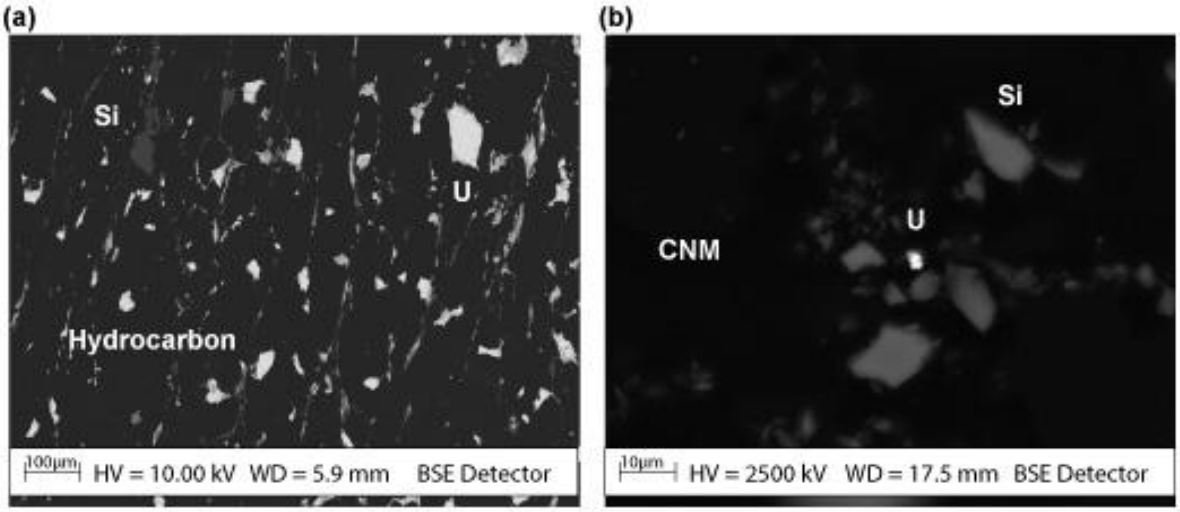


Figure 5.10 SEM Images of Beisa Reef compared to CCVD sample
SEM images comparing (a) Beisa Reef carbon seam sample showing small fragmented uraninite grains (U) encompassed in hydrocarbon and, (b) CCVD product mounted in resin and polished, showing powdered uraninite (U) and silicate minerals surrounded by carbon nanomaterials (CNM).

The Beisa Reef sample clearly showed the classic U-C association from the Witwatersrand Basin, where small uraninite grains were fragmented within a carbon seam (Figure 5.10a). The CCVD product by comparison, which was kept in its agglomerated form and mounted in resin, also showed uraninite completely encompassed within carbon nanomaterials along with other silicate minerals (Figure 5.10b). The EDS spectra from the sample analysed in Figure 5.11b showed that the uranium-bearing minerals were in fact uraninite (with some minor zircon grains also containing uranium, Appendix H). This provided evidence that not only was uranium present in the powders encapsulated by CNSs, but the uranium-bearing mineral was specifically uraninite.

5.6 Discussion

The ability to form ordered solid carbon nanomaterials, from a gas phase, was of great interest to this work in the context of the Witwatersrand Basin. In over one hundred experiments CNSs were grown onto uranium-bearing powders. This was also of interest as CNSs have been

observed to grow best with metals such as: Co, Ni, Au and Cu (Moshkalyov et al., 2004; Shaikjee and Coville, 2012). However, it was shown by leaching, that the U concentration appeared to be the most significant factor in the growth CNSs in the experiments undertaken in this study. Growth of CNSs in these experiments was found to be temperature dependant. At 300°C very little CNSs grew over a period of 2 h; this indicated a very slow growth rate at this temperature. At 450°C very small quantities of CNSs grew and the data revealed that the carbon in these products was not very well ordered (as confirmed by TEM and LRS). At 600°C the highest growth rate of CNSs was noted. The carbon in the CNSs was more ordered and consisted of: sheet-like carbonaceous materials, spiral-shaped carbon nanofibers, carbon nanotubes and complex spiral-shaped carbon nanofibers.

A number of other elements (in trace quantities) were also associated with CNS formation i.e. Cu, Mo and Sr. Although metals such as Cu, Ni, Co and Au have previously been used as catalysts in CNS formation (Thostenson et al., 2001; Zhou et al., 2006; Durbach et al., 2009; Li et al., 2009), these were usually carefully deposited in larger quantities on nanoporous supports. Hence their preparation was vastly different to the powdered granitic/meta-sedimentary substrates that were used in this study. The natural powders used here demonstrated that even small concentrations of these metals (e.g. 70 μg/g of Cu), were sufficient to drastically enhance the growth of CNSs. Since the concentrations Cu, Mo and Sr were significantly lower than that of the uranium (other than in the HILG19 powders), it was clear that growth of CNSs in these natural powders was controlled by a complex interaction of uranium and these metals. This was especially apparent when almost 50% of the U in these samples was removed and the mass of CNSs that formed decreased by 35% for <32 μm powders of HILG19. These leaching experiments showed that even in the sample with the highest concentrations of Cu, Mo and Sr, when a large portion of U was removed, this substantially reduced the quantity of CNSs that were formed. The deposition of ‘soot’ on the quartz boat demonstrated that carbonaceous materials could be precipitated onto surfaces free from metal supports. However, the negligible mass of the carbonaceous matter adhered to the quartz boat emphasised the importance of catalytic supports in the precipitation of carbonaceous materials.

With regards to the Witwatersrand Basin, there were at least two reasons why it was possible that the thermochemical reactions, which occurred in these CCVD experiments, could have played a role in hydrocarbon formation. Firstly, the reaction temperatures that were used to form these experimental products (i.e. 300-600°C) were plausible in the context of the Witwatersrand Basin, as researchers have obtained average values of 350°C crystallisation of chlorite and other minerals (Phillips and Law, 1994). However, fluid inclusion micro-thermometry has also identified hydrocarbon bearing fluids with temperatures postulated to be as high as 500°C. Secondly, it is plausible that if the correct gaseous hydrocarbon source was present (as is shown in Section 1.10), carbonaceous materials could have precipitated as nanostructured fibres, tubes and especially sheet-like carbons when in proximity to minerals containing U, Cu, Sr and/or Mo. It must be noted, that not all of these elements would have been specifically required for carbon to form in this way.

Laser Raman spectra of Witwatersrand seam and nodular carbon (Drennan, 1997), when compared with the experimental products, revealed that their signatures were very similar to those that were synthesised by CCVD. This indicated that the carbon in the Witwatersrand had a similar disordered-ordered (I_D/I_G) ratio (Ferrari and Robertson, 2000; Motchelaho et al., 2011) as the experimental products that were grown onto the uraniferous powders by CCVD. Indeed not only was the I_D/I_G ratio for LRS of the experimental products at 450°C similar to those of the Witwatersrand (Table 5.3), but their carbonaceous contents were also similar (Figure 5.9c vs Figure 5.10b). Interestingly, the habit and form of the CCVD products were very similar to the habit of natural Witwatersrand carbonaceous matter. On a millimetre-scale, the nanocarbon grew around the contours of the boat and formed in columnar fashion perpendicular to the base of the quartz boat. At low temperatures the growth of the CNSs was quite linear and somewhat perpendicular to the surface of the powdered crystals. However, samples that grew at higher temperatures showed a variety of nanostructures, which appear to have grown in all directions from the uraniferous powdered particles. TEM micrographs of the CLR from the Witwatersrand Basin showed remarkable similarity to those of the CCVD products, and it was seen that the fibrous, sheet-like nature of the Witwatersrand hydrocarbon extended to the nanoscale as well.

Radiolysis of hydrocarbons is an important process with regards to the Witwatersrand Basin (Schidlowski, 1981). However, with U, Pb and Th as the principle radiogenic elements, radiolytic polymerisation would be expected to take hundreds of millions to billions of years. Therefore, it is unlikely that there was sufficient time or radiation in these experiments for ionising radiation to effect the formation of carbonaceous products. Clearly catalysis played the most important role in nanocarbon growth and structural organisation in the CCVD experiments. Previous research shows the metals that are involved in the formation of CNSs are typically detached from the surface of the catalyst and included within the CNSs (Dupuis, 2005; Coville et al., 2011). The catalytic process at the nanoscale is called 'electron promotion' if the metal catalyst gives electrons to the carbon atoms, or 'structural promotion' if the catalyst shares electrons with the carbon atoms during the formation of CNSs (Coville et al., 2011). Therefore, the metal particles contained in Figure 5.8d and Figure 5.9a are significant as they demonstrate that hydrocarbon growth is catalysed by the metals U, Sr, Mo and Cu in these reactions. Critically, uranium from uraninite is specifically involved in the CNSs growth as is shown by Figure 5.10b and the SEM EDS results of these particles (Appendix H).

Despite all of the similarities between the signature and form of the CCVD products to the Witwatersrand carbon forms, the experimental conditions do differ from geological conditions. The temperature ranges, for instance, demonstrate the effect of increasing temperature on the form and signature of carbonaceous materials synthesised by catalysis. However, large temperature variations in the Witwatersrand Basin were unlikely to be widespread, with the highest temperatures likely to be restricted to heat associated with dykes and veins intrusions (Phillips and Law, 2000) as well as friction generated along fault planes. Therefore the lower temperature results showed that very slow formation of carbonaceous materials were important. The 300 °C experiments show that carbonaceous materials can catalyse onto uranium-bearing phases in short periods of time. If the experimental limitations allowed for far longer periods of reaction (days or even weeks) it is likely that larger masses of carbonaceous materials would form.

There are a number of other experimental factors that do not match up with the geological conditions of the Witwatersrand Basin: (i) the pressure is very low compared to likely lithostatic

pressures at even a few kilometres depth, (ii) the ratio of fluid/gas to rock/sample powder are much larger than , (iii) the experiments, necessarily, are more reducing than natural conditions, (iv) the uranium contents in the Witwatersrand Basin would be considerably higher than that of the experimental uraniferous powders and (v) the chemical system is also very simplified compared to the complex natural system. These factors do provide perspective as to why the experimental results may vary from the natural Witwatersrand carbonaceous matter. However, the experiments are designed to be simple, repeatable and demonstrate the specific role that uranium (and consequently other metal catalysts) played in the growth of carbonaceous materials. The data from these experiments strongly suggests that the growth of CNSs was correlated to the concentration of uranium.

Therefore, while the conditions do not, and at this stage cannot match natural conditions perfectly, the experiments do demonstrate that uranium and other metals could be responsible for catalysing carbon precipitation from a gas phase to a solid structured form.

5.7 Conclusions

- CNSs were successfully grown onto uranium-bearing powders,
- <32 µm uraniferous powders deposited more carbonaceous products than larger 32-75 µm powders,
- At 300°C, minor quantities of CNSs formed; at 450°C greater quantities of CNSs were formed, while at 600°C the greatest quantity of products was formed
- At 600°C the uraniferous powder was completely enveloped by carbonaceous product. Here the product followed the form of the boat, was fibrous in nature and exhibited a colloform form at the upper unrestricted surface. This form was similar to seam carbon in the Witwatersrand Basin
- U, Cu, Mo and Sr were strongly correlated with carbon formation in CCVD experiments.
- When c.a. 50% U was leached out of the uraniferous powder with the highest concentrations of Cu, Mo and Sr (i.e. HILG19 <32 µm), there was a 35% reduction in product formation

- The growth of these structures showed similarities in Raman signature (especially at 450°C) to the U-C associations seen in the Witwatersrand Basin.
- TEM images revealed the complex nature of CNSs formed at 600°C and the simpler more linear CNSs formed at lower temperatures
- TEM images reveal Witwatersrand carbon is sheet-like in form, which is similar to some of the CNSs formed in experiments
- SEM images of a Witwatersrand Beisa Reef ore block were very similar to an ore block of experimentally grown carbonaceous matter
- While the form and signature of the experimental carbon was similar to that of the Witwatersrand Basin, the effects of applied pressure, reaction time and radioactivity on the formation of these carbonaceous materials could not be ascertained in comparison to the carbon from the Witwatersrand Basin.

6 Micro-CT data from the Carbon Leader Reef

6.1 Introduction

Experiments proved it is possible to precipitate ordered solid carbonaceous materials onto uraninite grains (Chapter 5) and PIXE provides elemental distribution within these carbon forms (Chapter 4). However, further investigation was required into the mineralising process within the Witwatersrand Basin carbon seams. The best suited way to do this was to view the form of the carbon and gold structures in carbon seams. As such, computed tomography in conjunction with Auto-SEM-EDS maps was used to model the distribution of gold in 3D.

The results of this Chapter are in preparation for publication as:

Woods, T.H., Drennan, G.R., Carlson, K.J and Tonžetić, I. Ž. 2016c. The Anatomy of Gold: X-Ray Tomography of the Internal Structure of a Carbon Seam from the Witwatersrand Basin. In Preparation.

The data presented in this Chapter is the collaborative effort of the author and the co-authors whom operated the Auto-SEM and micro-CT instruments. Mr. I. Tonžetić analysed and classified the minerals for the Auto-SEM-EDS maps, and Dr. K. Carlson obtained the projections for the µCT scan. While machine operation was not performed by the author, the scientific ideas and direction crucial to obtaining meaningful results were. Data processing, image synthesis and compilation were all provided by the author. Prof. G. Drennan provided support and ideas that contributed to the processing of the data and the preparation of the paper.

6.2 Sample and Petrography

The sample selected for this study is an example of a well-developed carbon seam displaying clear carbon spindles from the Carbon Leader Reef (Carletonville Gold field) which has anomalous amounts of gold between spindles. The sample comprises a 22 mm thick carbon seam, enclosed between a quartz-pebble conglomerate (footwall) and a quartzite (hanging wall) layer (Figure 6.1). Whilst the whole sample was utilised for non-destructive µCT analysis (Section 2.2) only a

small portion of the sample (10 mm thick) was available for other analytic techniques which required preparation as a polished ore block.



Figure 6.1 Photograph of Carbon Leader Reef sample
Image showing carbon seam bound by a conglomerate footwall and quartzite hanging wall. The photo is taken parallel to strike, orthogonal to dip. The white dotted-line shows where the sample was cut and prepared as an ore block

6.3 Results

6.3.1 Internal structure of the carbon seam

The polished ore block was examined for trends in gold distribution and evidence of secondary features (veinlets, micro-faulting and secondary minerals). Figure 6.2 illustrates the carbon seam between the conglomerate footwall and quartzite hanging wall.

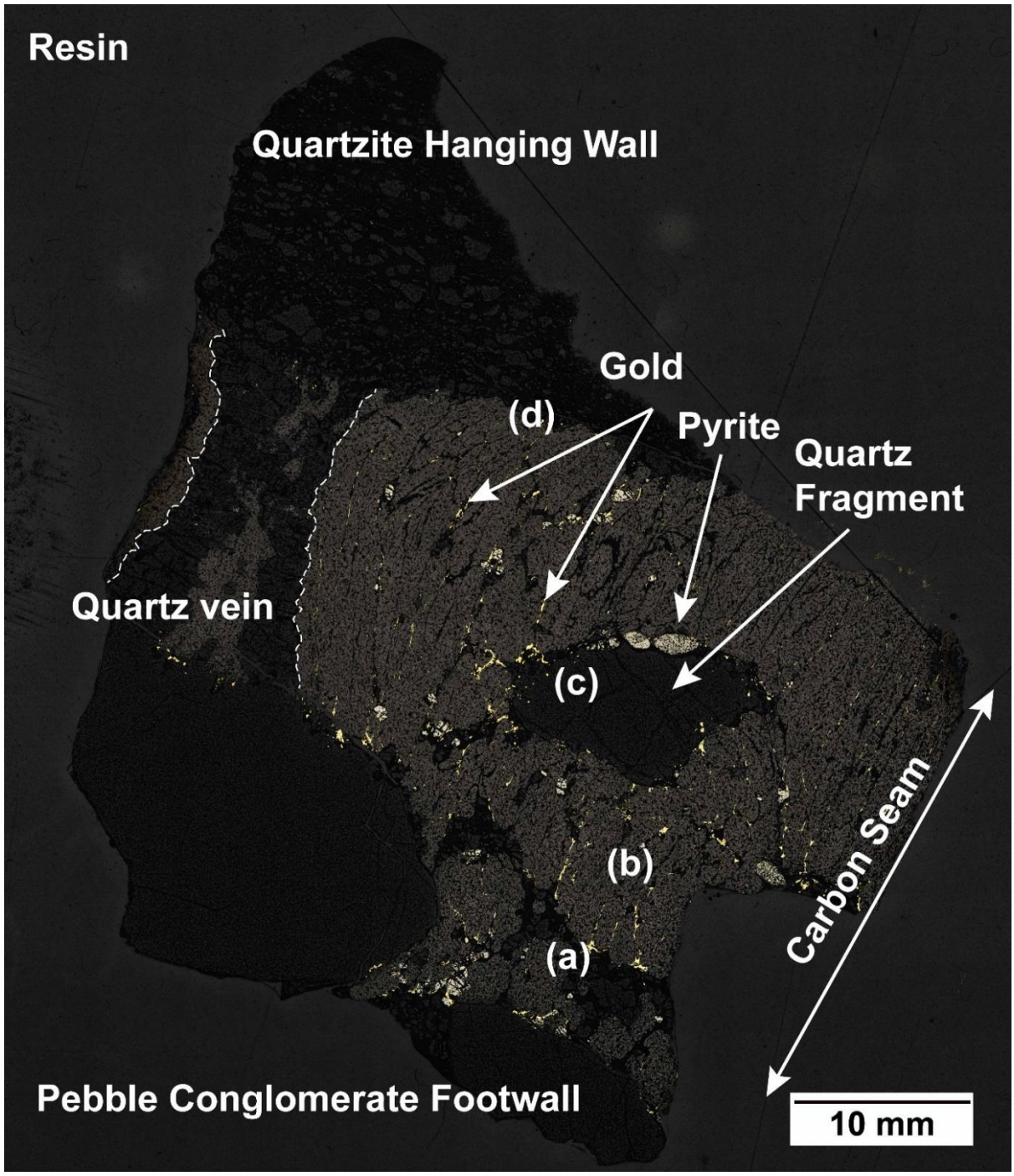


Figure 6.2. Stitched petrographic image of CLR ore block.
The carbon seam is bounded by a quartzite hanging wall and a conglomeratic footwall. The sample is mounted in resin. The quartz vein cutting the sample is highlighted (by the dotted white line) as well as the positions of the enlarged views for Figure 6.3a– d.

The undulating pebble surfaces form the base onto which carbonaceous material appears to have formed with smaller masses infilling spaces between the larger quartz clasts (Figure 6.3a). The base of the carbon seam contains fragmented pyrite grains within micro-crystalline silicate

minerals between rounded hydrocarbon masses (Figure 6.3a). Gold is seen infilling fractures in pyrite grains as well as coating the base of carbon spindles in contact with the clasts. Where the spindles extend upwards from the base, gold is seen infilling the tapered spaces between adjacent spindles (Figure 6.3b).

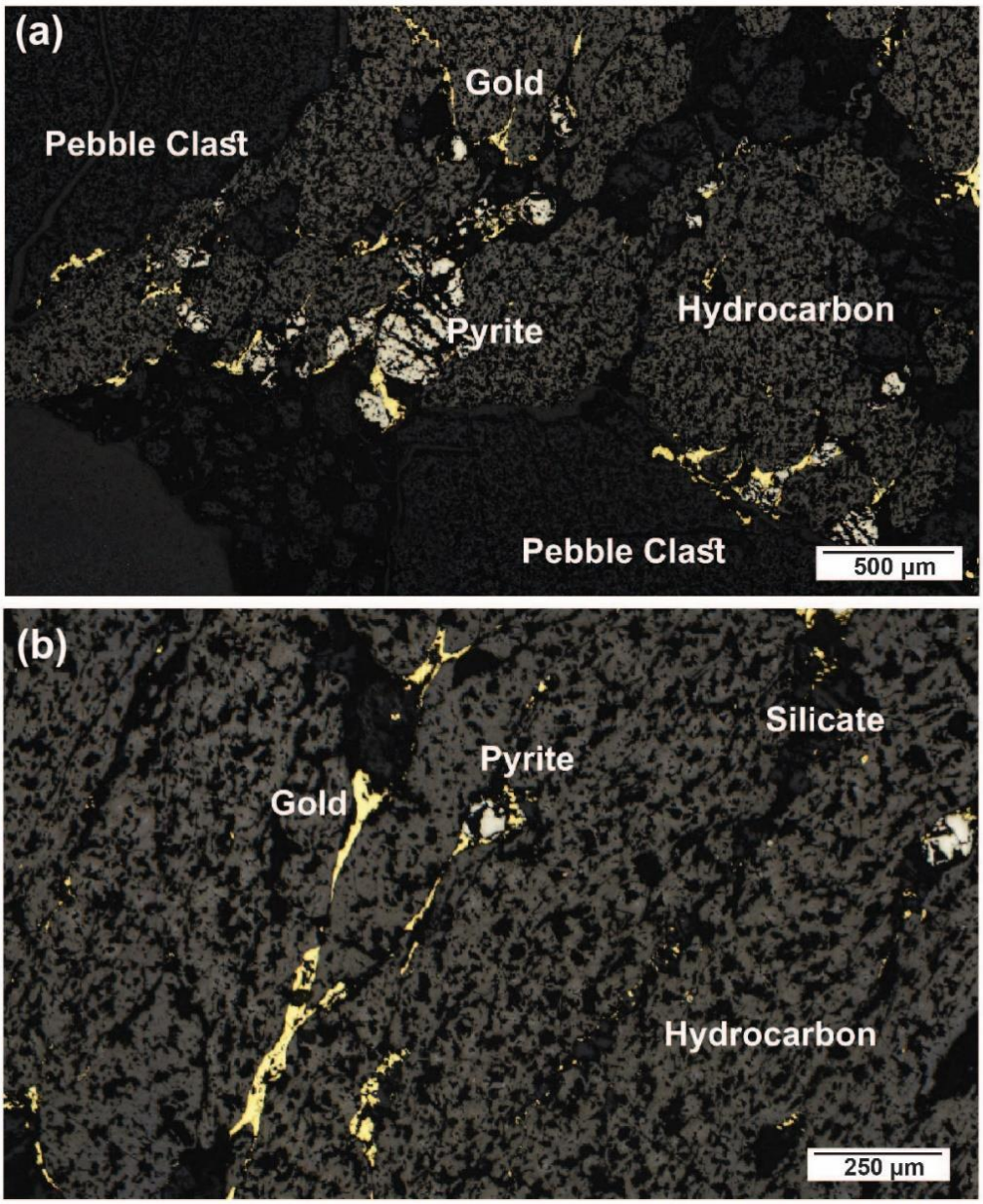


Figure 6.3 Enlarged reflected light images of CLR sample features
(a) Base of the carbon seam spindles, showing fractured pyrite and gold at pebble conglomerate contact; (b) lower carbon seam spindles with gold and silicate minerals between spindles;

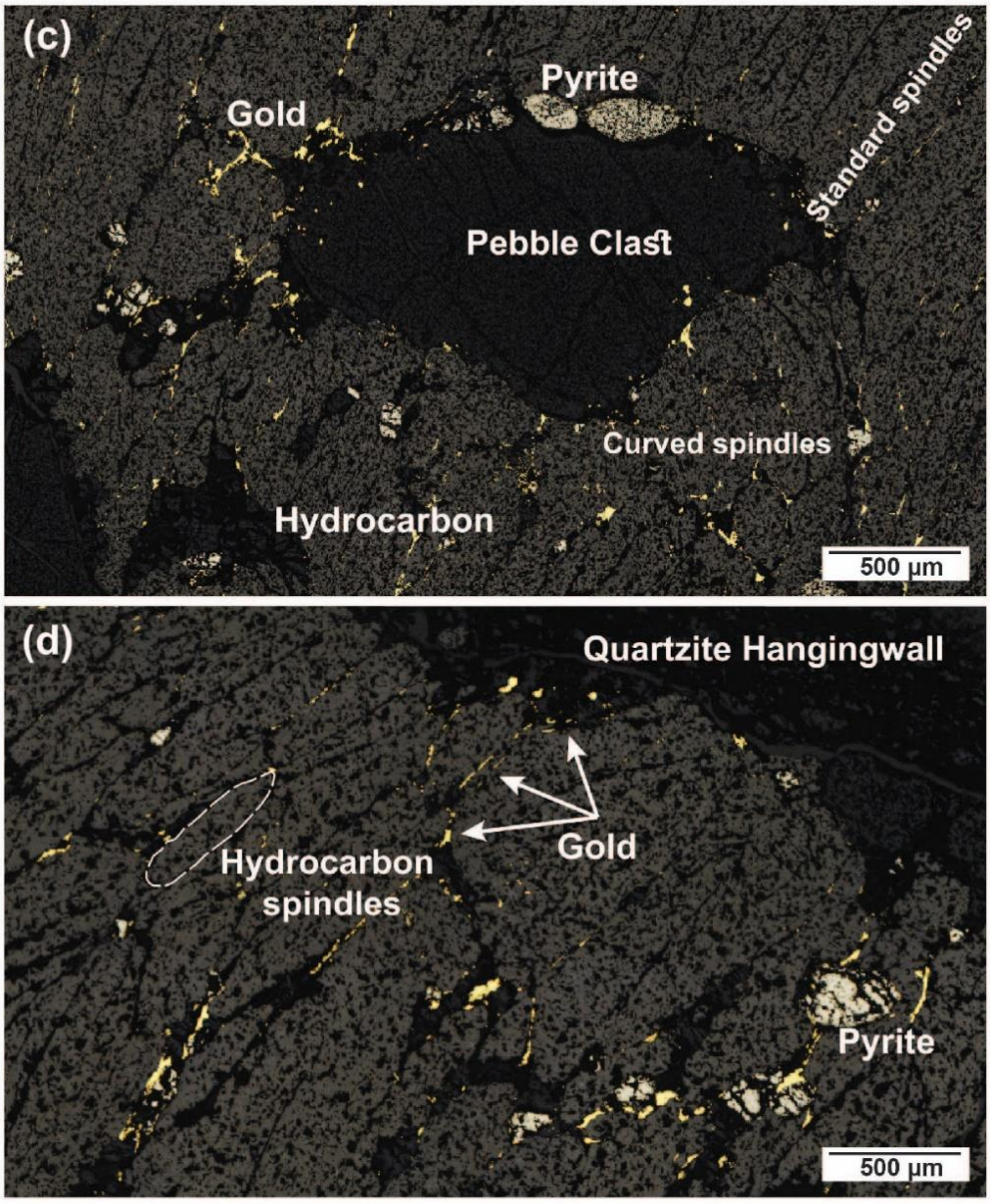


Figure 6.3 continued Enlarged reflected light images of CLR sample features
(c) Quartz pebble clast in the middle of the carbon seam and (d) upper carbon seam, with a single spindle highlighted and lesser gold at the contact with the hanging wall.

In addition to the gold between the hydrocarbons there is gold within an unidentified fine-grained silicate mineral (Figure 6.3b). Gold throughout the carbon seam in this section is most concentrated at the base of the spindles (Figure 6.2). Closer to the quartzite hanging wall the gold occurs as filaments between the hydrocarbon spindles gold as well as smaller particulate gold (Figure 6.3d). Gold throughout the sample follows the form of the surrounding hydrocarbon

or pyrite phases, with little or no visible rounded detrital gold (Figure 6.3b & d). Within the carbon seam, there is a sub rounded and fractured quartz clast (Figure 6.3c). The clast has an enrichment of gold at the contact between itself and the rounded porous pyrite and the enclosing hydrocarbon. The spindles of the carbon seam are elongated in two different directions around the quartz clast (Figure 6.3b) standard spindles are continuous; curved spindles below clast spindles are bent towards the clast). This is in contrast to carbon spindles above, which are quite uniform and occur perpendicular to the bounding surface of the hanging wall (Figure 6.3d). Carbon spindles are also seen forming between adjacent pyrite and quartz clasts. In these cases, the width of the spindle is reduced between clasts and then extending back to the same bounds on either side of the clasts. A small quartz vein occurs ross-cutting the carbon seam (Figure 6.3b & d). The quartz vein contains micro-crystalline pyrite and is fractured parallel to strike. These fractures are infilled with fine grained silicate minerals. A quartz vein cross-cuts the carbon seam, displacing hydrocarbon masses on either side (Figure 6.2). In summary, most of the gold, silicates and pyrite within the sample occur between spindles of the carbon seam whereas uraninite is seen contained within the spindles.

6.4 Minerals associated with gold in between the carbon spindles

BSE images of the various mapped portions of the CLR sample (Figure 6.4) reveal features that are not clear in petrographic images. The carbon seam has abundant, and fairly evenly distributed, uraninite grains (30-50µm) within the spindles (Figure 6.5). Some of the larger grains of uraninite (50 -120 µm) appear fragmented into a mosaic of smaller grains separated by hydrocarbon. The shape of the spindles is easier to distinguish in the BSE images (Figure 6.5). At the base of the carbon seam, the spindles are more bulbous having rounded bases that taper upwards through the seam. In the middle of the carbon seam, spindles are more uniform in width, tapering towards the ends which are also rounded. The top of the carbon seam also contains bulbous, tapered spindles, although these are inverted with respect to those at the base of the seam (wide rounded top, pointed tapered base).

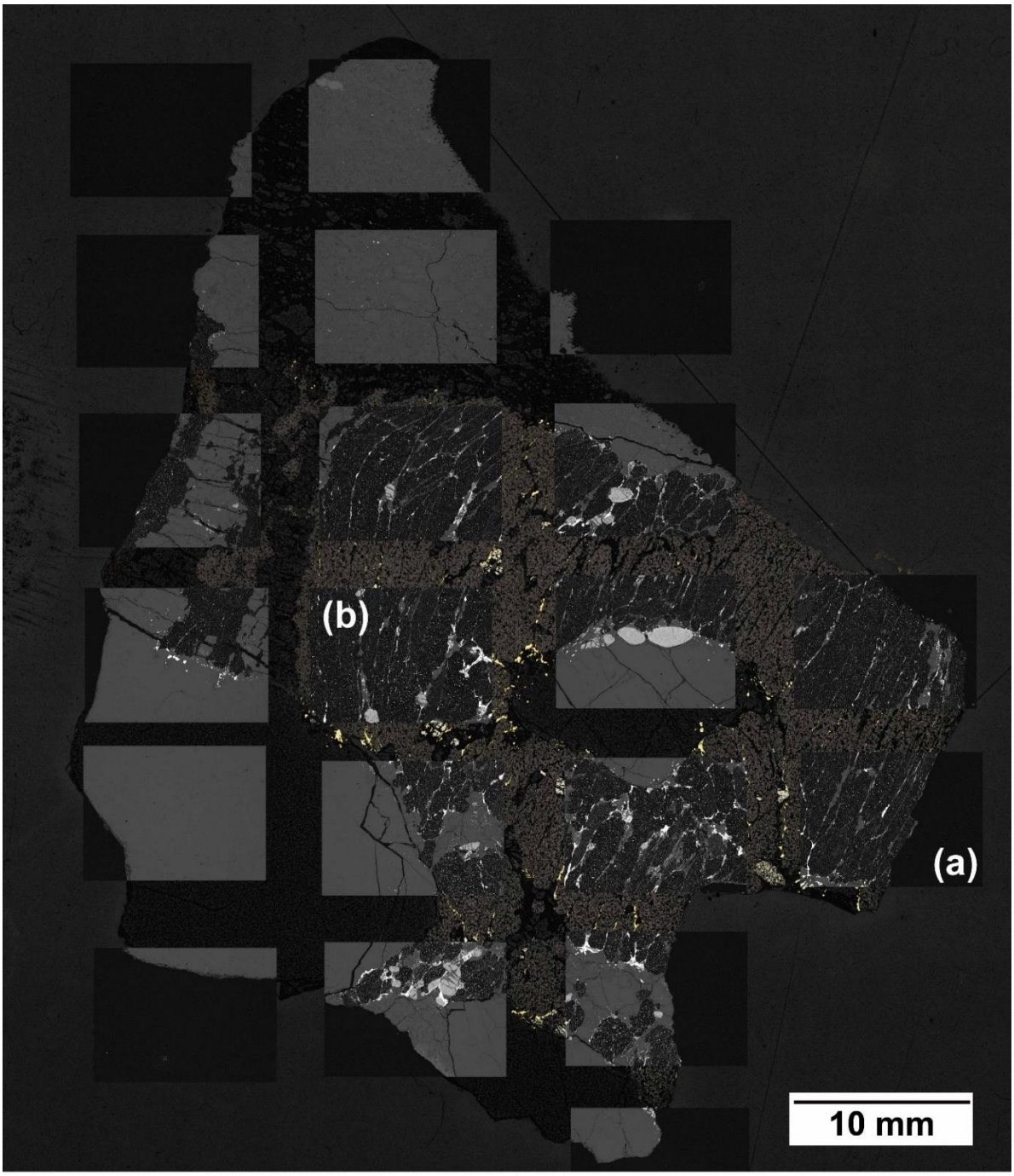


Figure 6.4. SEM BSE image overlaid over stitched optical microphotograph showing areas mapped by EDS.
The BSE overlays highlight materials between the spindles and enhance visibility of uraninite grains, gold and silicate minerals, (a) & (b) indicate the positions of Figure 6.5a & b respectively.

The images also reveal the presence of numerous smaller, rounded carbon nodules within the carbon spindles (Figure 6.5b). Multiple nodules are seen overgrown by a larger spindle (Figure 6.5 b). It is clear from the BSE images that the minerals between the spindles occur as separate phases with distinct boundaries (Figure 6.5a & b).

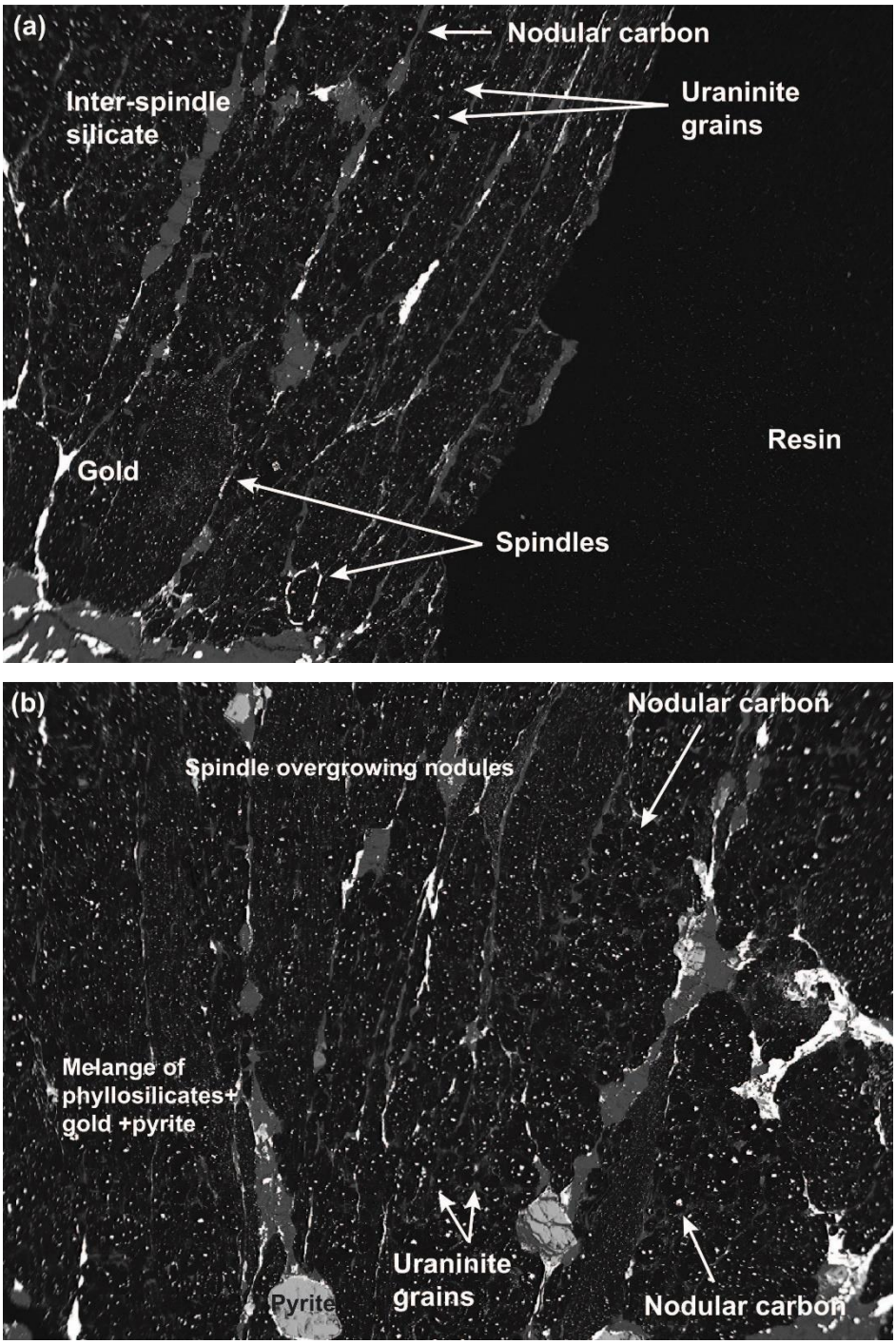


Figure 6.5 BSE image of seam portion of CLR sample
Images show the uraninite grains that are more easily distinguishable than observed by optical petrography. (a) The dark material is the hydrocarbon which forms spindles, outlined by the gold and silicate materials between them. One of the spindles is outlined to demonstrate this. (b) Small rounded carbon nodules overgrown by a larger spindle, also highlighted is the melange of phyllosilicates, gold and pyrite between the spindles.

The EDS mineral maps show that the inter-spindle fine-grained minerals are comprised of varying amounts of phyllosilicates, quartz, gold and pyrite (Figure 6.6).

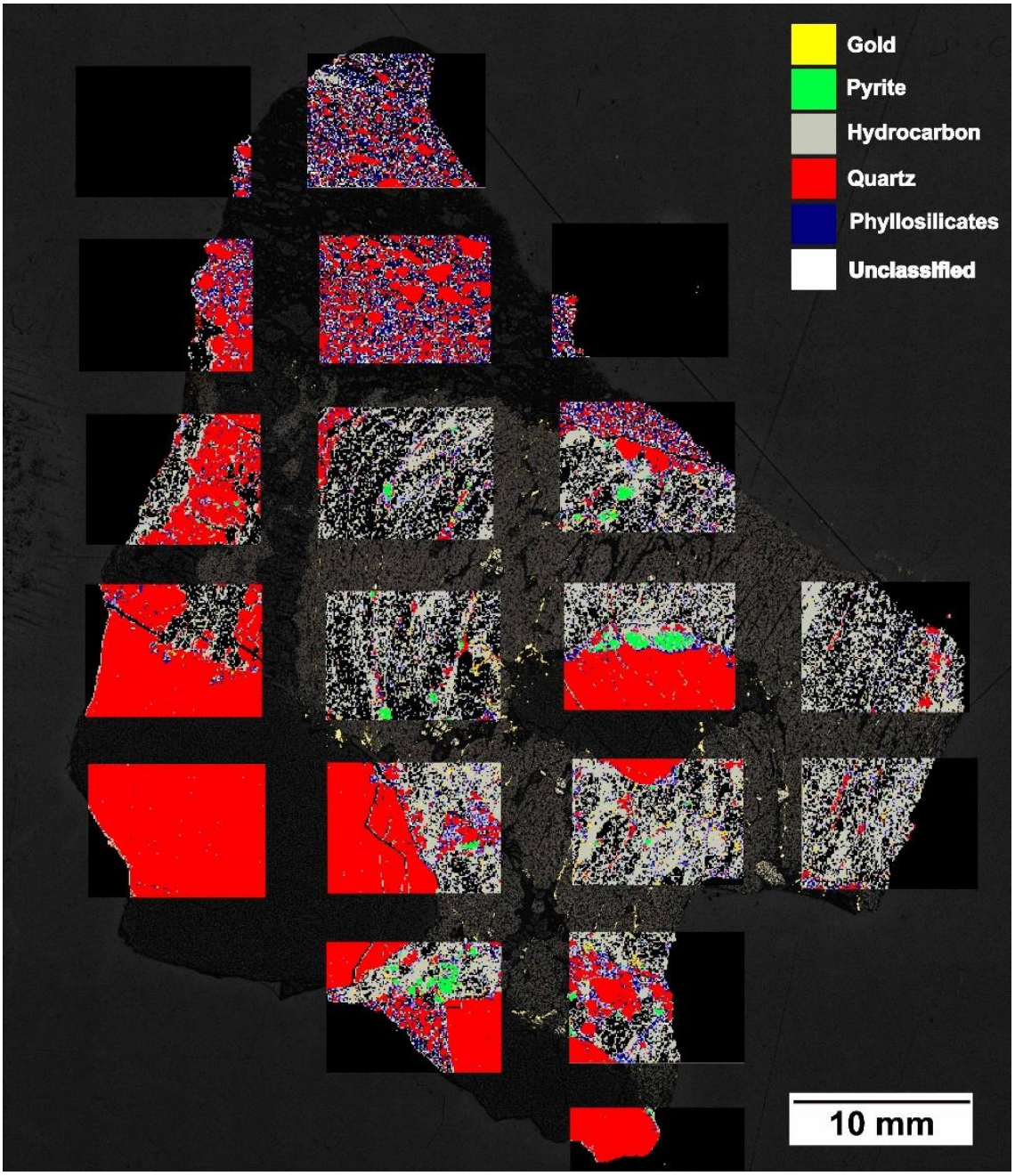


Figure 6.6 Mineral classification of CLR sample as shown by Auto-SEM-EDS
Image shows false colour composite map of minerals as identified by Auto-SEM-EDS. The abundance of phyllosilicates and pyrite is outlined especially well by these images.

Phyllosilicates predominantly include kaolinite, pyrophyllite, muscovite, illite, chlorite, chloritoid, and talc (see EDS quantified mineralogy in supplementary materials, Appendix I) ranging from ~65 to 150 µm. Pyrite grains (particularly the rounded porous pyrite) contain small amounts of gold. Hydrocarbons are also detected in the hanging wall as small rounded nodules (Figure 6.6).

The hanging wall contains the largest concentrations of phyllosilicate materials within a fine-grained matrix between the rounded quartzite grains.

6.4.1 Gold distribution in Three Dimensions

A threshold was applied to the µCT 3D rendered data (as outlined in Section 2.7) to display only the gold (based on a density contrast) in any selected area within the sample (Figure 6.7).

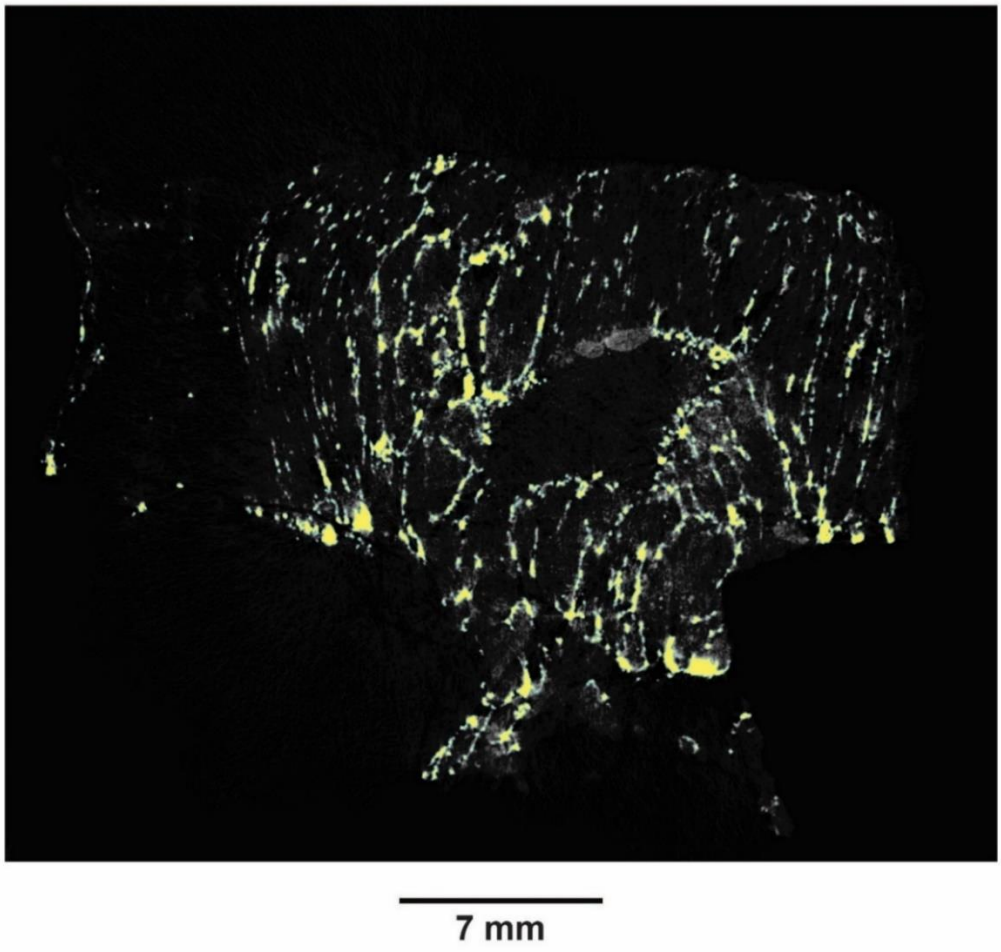


Figure 6.7. Gold regions of interest from µCT data threshold
The yellow areas with blue outlines (representing boundaries) encompass the gold. This image was compared to one derived from petrography to determine the accuracy of the threshold estimate of the gold

The render was able to differentiate between gold and other materials, but the other materials could not be further differentiated from each other (e.g. pyrite from phyllosilicates). This region of interest was compared against the background of hydrocarbon and silicate materials in order

to visualize and assess organisational characteristics in three-dimensional distributions (Figure 6.7).The 3D rendered µCT data (Figure 6.7) highlights a greater abundance of gold than first detected by traditional 2D petrographic methods. This is likely due to the limited 'slice' view that such 2D methods allow which may not highlight the full extent of mineralisation in all directions (e.g. parallel or perpendicular to the plane of view during SEM investigations). The 3D rendered µCT data (Figure 6.7) reveals that gold present in the pyrite grains was underestimated and this was taken into account when determining the rendered gold values of the sample (so as not to overestimate the volume of gold in the hydrocarbon). In both optical petrography and the BSE images gold was seen as inclusions in fractures in the pyrite grains.

Scanned data slices of µCT (rendered perpendicular to strike of the carbon seam) accentuate changes in the lateral distribution of gold between the lower and upper portions of the seam from the footwall to the hanging wall (Figure 6.8a – f). The base of the carbon seam has the highest concentrations of gold, occurring as grains and coatings to the spindles. The grains are concentrated in the interstices at the base of the carbon spindles. Slices through the centre of the carbon seam (Figure 6.8e & f) reveal that gold concentrates as filaments only in the space between spindles (as was seen in the vertical slices, see supplementary materials) and not as particulate gold. Beneath the displaced quartz clast, gold is also strongly concentrated in the spaces between the carbon spindles (Figure 6.7 & Figure 6.8f). Gold occurs at the top of the carbon seam (hanging wall contact) but is less concentrated than at the footwall contact (i.e., fewer gold globules are noted in the µCT data (Figure 6.8b vs. Figure 6.8h). The views in Figure 6.8 also show the extent of the cross-cutting quartz vein (Figure 6.8e, f & g). The vein cuts through the seam displacing masses of carbon and gold. Highest gold concentrations are seen at the base of the carbon seam within the carbonaceous material (Figure 6.8a & b).

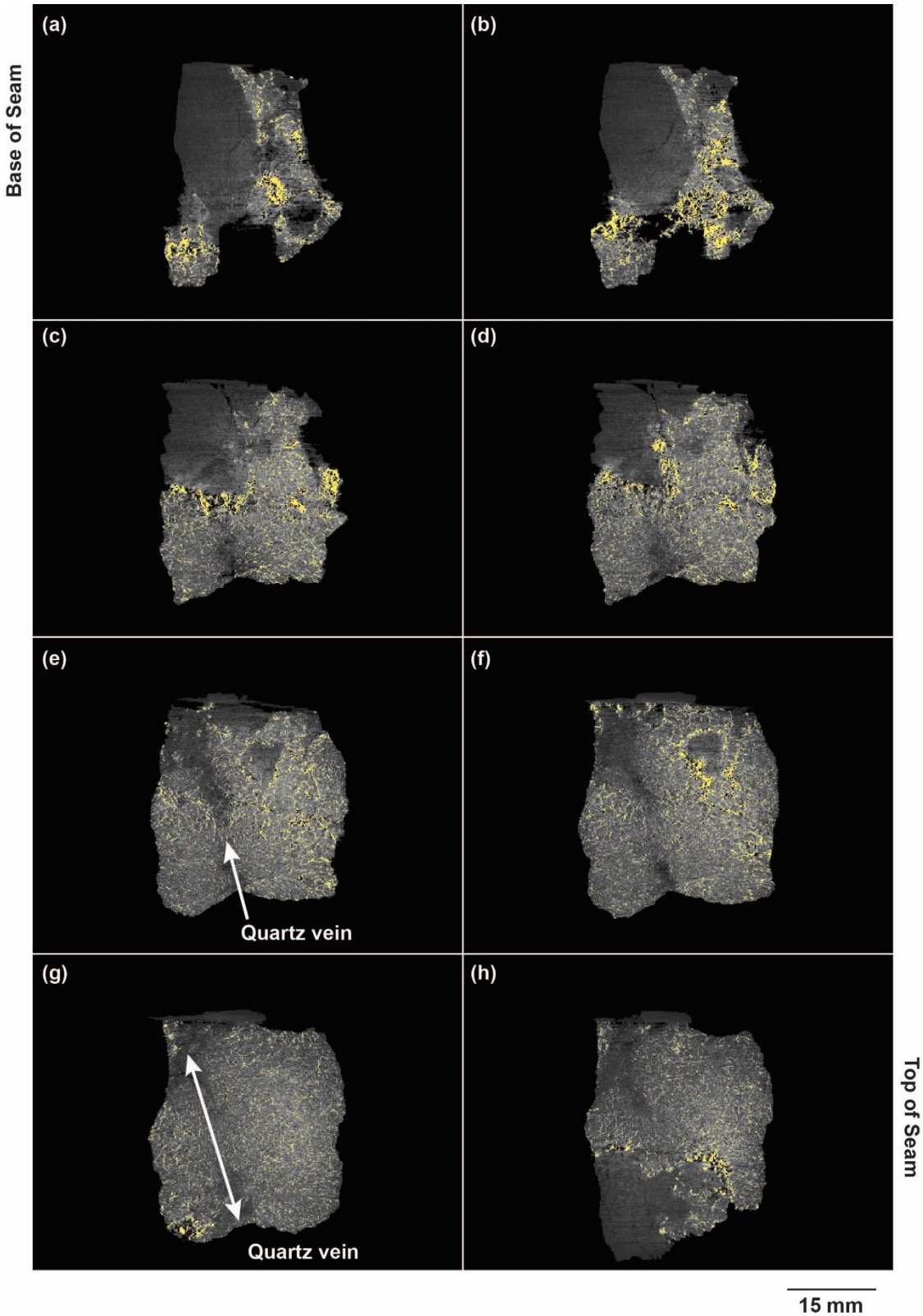


Figure 6.8. Tomography slices through CLR sample. The slices are taken from the base of the seam (a) moving up towards the quartzite hanging wall (h).

6.5 Discussion

6.5.1 Spindles and Mineralisation

The abundant fragmented uraninite grains throughout the carbon spindles are thought to be a substrate onto which the hydrocarbons precipitate (Schidlowski, 1981; England *et al*., 2002). The precipitation of hydrocarbon onto uranium-bearing phases has been shown to be the result of catalytic precipitation possibly with a component of radiolytic polymerisation (Chapter 5). Thus, it is suggested that the uraninite present in carbonaceous seam is of a detrital origin, but crucial to the formation of carbon seams and the enhancing of gold values.

The consistent occurrence of gold and phyllosilicates in the spaces between carbon spindles indicates an association between these minerals (Figure 6.3). Phyllosilicate minerals elsewhere in the Witwatersrand Basin have been described as secondary mineral phases (Phillips, 1987; Phillips and Law, 1994). Within the CLR sample, phyllosilicates occur as microcrystalline masses which include kaolinite, pyrophyllite, muscovite, illite, chlorite, chloritoid, and talc. Consequently the occurrences of phyllosilicates in the CLR sample are consistent with the minerals characterised as metamorphic minerals by Phillips (1987). Small inclusions of phyllosilicates and gold occur within the carbon spindles themselves (as shown by Figure 6.5 & Figure 6.6) but are predominantly found between spindles.

This supports the hypothesis of a multiple fluid component model recorded in the carbon seams and proposed in Chapter 4. Similar findings were reported by Drennan & Robb (2006) for the Beisa Reef and for carbon nodules found in quartz veins within the basin. This also suggests that the co-existing inter-spindle phyllosilicate and gold occurrences precipitated from the liquid remaining after the initial precipitation of spindles. This would explain the occurrence of finely disseminated gold and phyllosilicates within the spindles as well as microcrystalline gold and phyllosilicates between the spindles.

Additional evidence for a multiple fluid component mineralisation mechanism can be seen from the BSE images of the phyllosilicate minerals between the spindles i.e., the phyllosilicates, gold and other microcrystalline minerals form a “melange” between spindles. The rounded pyrite

grains and some quartz inclusions within the carbon seams that cause spindles to contort around them, provide evidence that these grains were present before the formation of the carbon seam

The contortion of the seam carbon, along with literary evidence for detrital mineralisation and remobilising fluid processes, led to the following hypothesis for carbon seam formation. It is suggested that initially gold, uranium and pyrite were deposited by fluvial processes followed by remobilisation of mineralisation by multiple fluids (including hydrocarbon-rich fluids), which later precipitated in the presence of concentrations of uraninite. This precipitation resulted in mineralised spindle growth. Precipitation of the mineralised hydrocarbon spindles caused supergene enrichment the remaining fluid with silicates, phyllosilicates, and whatever gold still remained in solution being enriched relative to the fluid that precipitated the hydrocarbon. This accounts for the presence of microcrystalline quartz, phyllosilicates and gold in the inter-spindle interstices.

6.5.2 3D Gold Distribution

This investigation presents the first published µCT scans of a carbon seam from the Witwatersrand Basin and allows the authors effectively display the 3D distribution of gold throughout this exceptional CLR sample. The most striking evidence supporting the epigenetic formation of hydrocarbons in the carbon seams is provided by the µCT render (Figure 6.7 & Figure 6.8). The presence of the quartz clast displaced within the CLR sample shows evidence of hydrocarbon precipitation after deposition. The clast appears to represent a fragment of a larger rounded pebble from the conglomerate below. This could be due to the greater porosity of the underlying conglomerate that allowed for fluid movement within the conglomerate. Evidence for fluid movement has been previously provided by Parnell (1999) and Jolley *et al.* (2004) where fluids appear to have moved parallel to bedding, as well as in thrust faults and in veins. Hydrocarbon precipitation along a pre-existing fracture in the quartz clast resulted in the displacement of the clast fragment. The accumulation of recrystallized gold in the hydrocarbon surrounding the fragment provides evidence of fluid migration along the pebble layer.

The µCT render shows that gold is most concentrated at the base of the carbon seam along pebble conglomerate contact of the footwall. From footwall to hanging wall, the gold

concentration decreases as the spindles develop before being concentrated again at the hanging wall contact (although the concentration of gold in the hanging wall contact is still markedly less than that of the footwall contact; Figure 6.8).

The spindles in the carbon seam are bulbous at the hanging wall and footwall contacts, and taper towards the centre of the carbon seam. Evidence that the carbon spindles were the product of hydrothermal precipitation is seen from the nodular carbon surrounded by phyllosilicates and gold that are overgrown by larger spindles. The forms of the carbon spindles, with maximum growth perpendicular to the bounding surfaces, are similar to crystals growth in quartz veins and pegmatites. Crystallisation in quartz veins and pegmatites is parallel to σ^1, the principle stress direction (Davis *et al*., 2012). In quartz veins crystals grow inwards from the bounding surfaces towards the centre. This provides a potential mechanism for the growth of the carbon spindles. Growth of the spindles commenced with globular masses of carbon and maximum gold precipitation adjacent to the bounding surfaces, becoming more elongated with lesser gold towards the centre of the carbon seam. The evidence presented in this research satisfies many of the issues concerning carbon seam formation in the Witwatersrand Basin and the distribution of gold within the seams.

However, here it is also apparent from the gold distribution that fluids moved from both the hanging wall and footwall in towards the reef contacts. This would explain the inverted spindle structures at the top of the seam. Additionally, it explains the tapering spindles, since with fewer fluids being available under pressure, slimmer spindles are precipitated.

6.6 Conclusions

- Gold and phyllosilicates occur as microcrystalline growths between spindles as well as disseminated within carbon spindles
- Spindle growth occurs principally perpendicular to bounding surfaces of footwall and hanging wall, becoming elongated parallel to the direction of principal stress

- Spindles displace around some rounded clast fragments, and appear to bend in towards these inclusions in places Gold is most concentrated at the base of the carbon seam and less concentrated towards the top contact with the hanging wall; gold concentrations decrease towards the centre of the carbon seam
- Evidence for µCT (as well as literature and previous research) suggests a fluid mechanism for precipitation and mineralisation redistribution as follows:
    - Carbon and gold (along with phyllosilicates, and pyrite) were precipitated from post-depositional, hydrocarbon-rich fluids around concentrations of uraninite by radiolytic polymerisation, resulting in the occurrence of disseminated gold, pyrite and phyllosilicate in hydrocarbon precipitates/spindles
    - Precipitation of quartz, phyllosilicate and gold in inter-spindle interstices from remaining fluid
    - Precipitation of quartz in late-stage cross-cutting quartz veins
- Gold distribution as shown by µCT data is indicative of bedding parallel fluid movement migrating through the more porous conglomerate and precipitating carbon inwards, similar to crystal growth in quartz veins

7 Solvothermal Experiments

7.1 Introduction

Based on results from the previous work, it became apparent that certain factors (e.g. reaction pressure) could not be modelled in the experiments that made use of the CCVD technique (Chapter 5). Therefore, an additional technique was sought where the effect of pressure could be explored. For instance, the solvothermal technique (where the carbon source is in a solution mixed with the solid powdered uraniferous material and placed in a thermostatically controlled autoclave) has been successfully used in the past to precipitate CNSs. The CNSs formed in these cases included nanospheres, nanobeads, nanonecklaces and sheet-like materials, at temperatures as low as 160 – 200°C (Kuang *et al*., 2004; Deshmukh *et al*., 2010). Since the formation of CNSs is modelled as the interaction between carbon atoms and the catalyst, the technique used to achieve changes the conditions of the experiments and not necessarily the interaction between the catalyst and the hydrocarbons (Deshmukh *et al*., 2010). Furthermore, solvothermal reactions have also been conducted at higher pressures, as they use reinforced reaction vessels (autoclaves). Hence the solvothermal technique allows for a study of the effect of pressure on the synthesis of CNSs. The effect of reaction temperature, powder size fraction, catalyst roles and uranium concentration on CNSs growth could be inferred by CCVD reactions (Chapter 5).

The objectives of the solvothermal experiments were to determine (I) if lower reaction temperatures could catalyse CNS formation in the presence of a uraniferous powder, (II) the effect of pressure on CNS formation, (III) if a sucrose carbonaceous source (derived from a biogenic source) could precipitate CNSs, and (iv) if gold could be precipitated out as a result of catalysing carbon in the presence of a uraniferous powder. In order to establish this, experiments using the method outlined in Section 2.12 were run at increasing pressures and then finally gold (in the form of aurichloric acid) was added to the system.

The results of this Chapter will be submitted as a manuscript for publication, which was in-preparation at the time this thesis was submitted.

The author conducted all the experimental design, work and sample preparation. Additionally, synthesis of the manuscripts for publication (still in preparation) were handled by the author. Due to time constraints, certain techniques required assistance from the instrument operators. Dr. R. Erasmus assisted with obtaining laser Raman spectra (guided by the author), Mr. O. Makgae assisted with the TGA analyses and Prof. H. Tutu assisted with ICP-OES analyses.

7.2 Mass and Physical Changes

Sucrose was selected for the carbon source in solution, as it is a common compound in primitive organic lifeforms. Additionally, it has very few metal contaminants and is known from previous studies to form solid carbon nanomaterials (Deshmukh *et al*., 2010). Solvothermal experiments run at 180°C for 18 h for various pressures (with or without uraniferous powders present) resulted in physical changes in the solutions in the autoclave. In each case the clear solution turned black and an odour akin to burnt sugar was noted. Similarly the walls of the Teflon inner cup and the thermocouple, were both covered in a fine black solid mass (Figure 7.1).

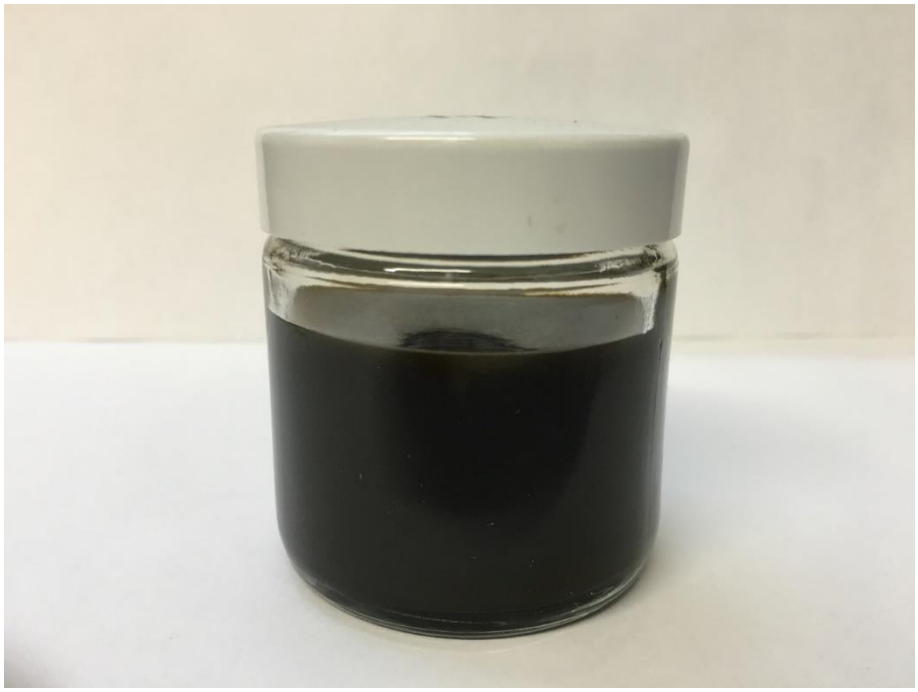


Figure 7.1 Product formed during solvothermal reaction of sucrose and HILG13 < 32µm
Liquid product of solvothermal reaction, the bottom of the container had a layer (only a couple millimeters thick) of solid "slurry".

The bottom of the Teflon inner cup also contained an accumulation of black solid material which had started to clump together. The products shown in Figure 7.1 demonstrate the physical change from a clear colourless liquid to a black opaque liquid.

It was observed that measuring the mass of products that were formed (once dried) was not a reliable indicator of the amount of growth that had occurred. The intention, as before, was to separate out the solid black-coloured products using standard filter paper and then measure the mass difference that had occurred. However, both the black-coloured product that was suspended in solution and the powder fractions (HILG19 < 32µm and HILG13 < 32µm) were too fine and some passed through the filter paper. This resulted in some product remaining on the filter paper and some in the solution. Thus other methods were required to quantify and qualify the effects of increased pressure on CNS formation in the solvothermal reactions that were conducted.

7.3 Laser Raman Spectroscopy

After each solvothermal reaction the black-coloured products were centrifuged. These materials were then separated and dried at 50°C for 2 h. The powders were then characterised by LRS and their spectra plotted (Figure 7.2). As with the materials formed by CCVD (Chapter 5), the Raman spectra revealed that these black-coloured products were also carbonaceous. As before, these solvothermal products had the characteristic “D” and “G” peaks that are associated with disordered and ordered/graphitic carbon respectively (Ferrari and Robertson, 2000; Reich and Thomsen, 2004). However, in contrast to the CCVD products (Chapter 5) the “G” peak was enhanced in the solvothermal products relative to the “D” peak. The Raman spectra showed that the solvothermal reactions produced proportionately more graphitic/ordered carbon (i.e. lower I_D/I_G ratios) than any of the Witwatersrand Carbon materials. Likewise they showed that the intensities of the spectra decreased as additional pressure (through the introduction of gaseous N_2) was added. The I_D/I_G ratios showed that reactions that were carried out at the highest pressures produced more graphitic products as compared to those with no additional pressure.

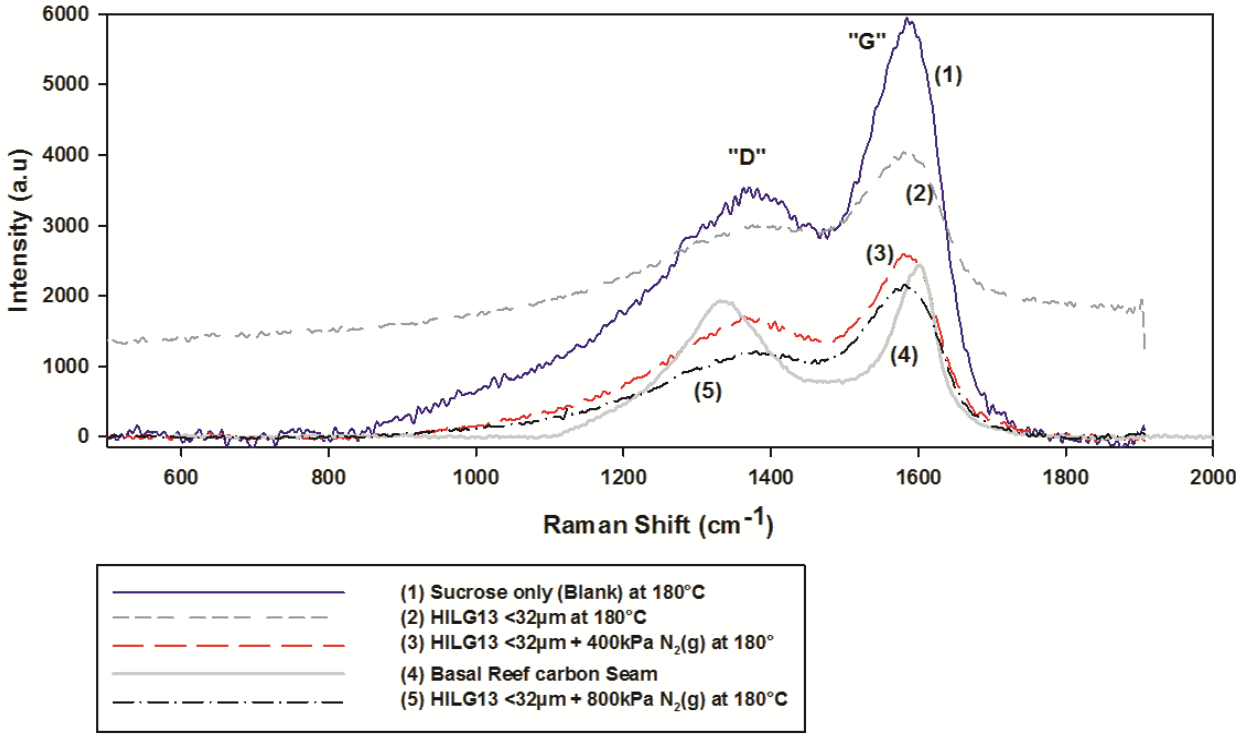


Figure 7.2 Raman spectra of the solvothermal products compared to Witwatersrand Carbon seam
(1) Reaction without any granitic powder added into system (only sucrose solution) run at 180°C; (2) Reaction using HILG19 <32 µm, with no added pressure, run at 180°C; (3) Reaction using HILG19 <32 µm, with 400 kPa N_2(g) added into system, run at 180°C; (4) Basal Reef carbon seam powder and (5) Reaction using HILG19 <32 µm, with 800 kPa N_2(g) added into system, run at 180°C.

Table 7.1 Raman and Thermal Analyses for solvothermal products compared to Witwatersrand Carbonaceous Materials

	Solvothermal Products	
	TGA T°	*I_D/I_G*
Sucrose only (blank),180°C @ atm. P	*386*	*0.65*
HILG13, 32 µm with sucrose, 180°C @ atm. P	300/342	0.60
HILG13, 32 µm with sucrose, 180°C @ atm. P + 400 kPa N_2	239/459	0.64
HILG13, 32 µm with sucrose, 180°C @ atm. P + 800 kPa N_2	242/345	0.55
HILG19, 32 µm with sucrose, 180°C @ atm. P	358	0.62
HILG19, 32 µm with sucrose, 180°C @ atm. P + 400 kPa N_2	284/386	0.60
HILG19, 32 µm with sucrose, 180°C @ atm. P + 800 kPa N_2	286/384	0.59
Witwatersrand Carbonaceous Materials		
Carbon Nodule from Beisa Reef		0.81
Carbon Seam from CLR		0.87
Carbon Seam from Basal Reef		0.82

7.4 Thermal Analysis

Thermal analyses were required to determine the thermal stability and confirm the nature of carbonaceous products formed in the solvothermal reactions. Here it was observed that the solvothermal type reactions formed vastly more masses of carbonaceous products as compared to the CCVD reactions (i.e. the higher derivative weight %'s reflected that higher quantities of carbonaceous material had formed - compare Figure 5.8 with Figure 7.3).

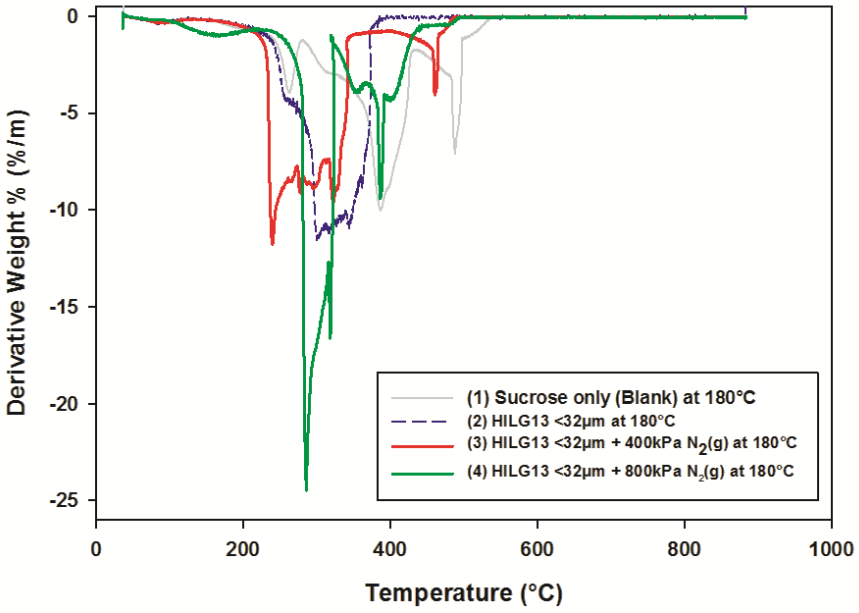


Figure 7.3 First derivative graphs of solvothermal products using HILG13 <32um powders
Positions of thermal maxima for (1) Reaction without any granitic powder added into system (only sucrose solution) run at 180°C; (2) Reaction using HILG19 <32 µm, with no added pressure, run at 180°C; (3) Reaction using HILG19 <32 µm, with 400 kPa N_2(g) added into system, run at 180°C and (4) Reaction using HILG19 <32 µm, with 800 kPa N_2(g) added into system, run at 180°C.

Additionally, the thermal maxima had increased to between 242 and 386°C (Table 7.1). This was higher than the temperatures at which the CCVD products had formed. The blank sample was found to have burnt at the highest temperature, which suggested that carbonaceous products with more structured/graphitic bonds had formed in the blank than the samples that contained granitic powders. However, it is important to note the highest pressures resulted in the greatest masses of carbonaceous products formed.

7.5 Transmitted Electron Microscopy

TEM images of the solvothermal products confirmed that nanostructured carbon had been deposited onto the uranium-bearing powders that were loaded into the reaction vessel (autoclave). The blank experiments (reacted without any uranium-bearing powders) only produced carbon microspheres which coalesced in some cases to form microbeads (Figure 7.4a). However, reactions that contained uranium-bearing powders also deposited sheet-like carbonaceous materials (in preference to micro spheres) onto or near the uraniferous powder particles (Figure 7.4b). With increasing pressure, the forms of the CNSs appeared to have changed. The carbon microspheres appeared to have joined together and the sphere shape was lost in favour of carbon nano-necklaces (Figure 7.5b).

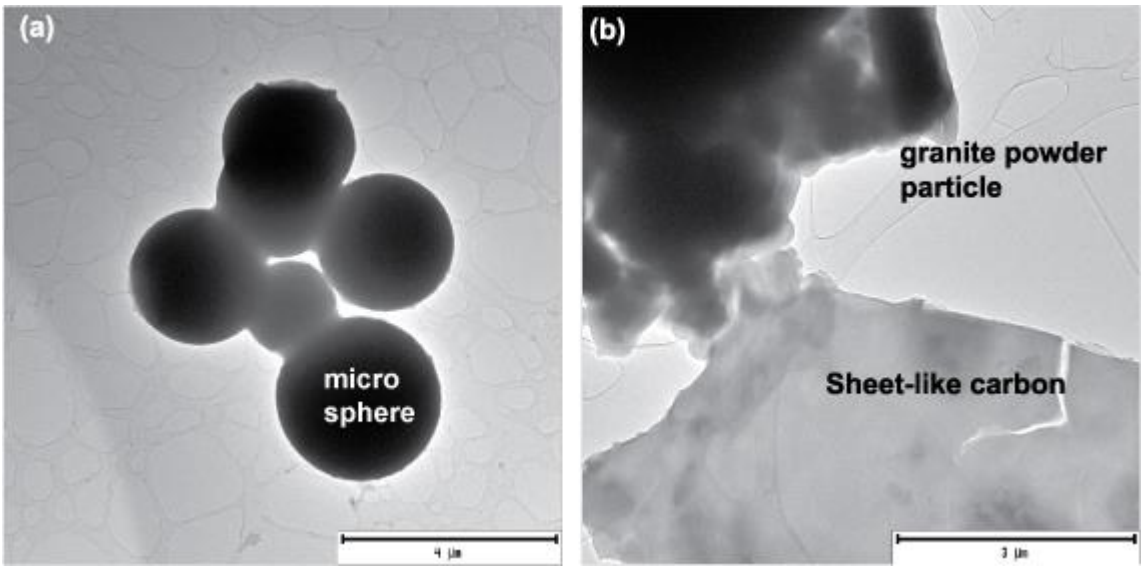


Figure 7.4 TEM images of solvothermal products
(a) Sucrose only (blank) run at 180°C and atmospheric pressure showing microspheres that are predominant and have started to weld together, (b)sheet-like carbonaceous products formed from reaction using HILG19 <32 µm, with 400 kPa N_2(g) added into system, run at 180°C

Additionally, crumpled nano-sheets were formed (Figure 7.5a). In one of the samples a U-particle was identified by EDS (see encircled item in red in Figure 7.5a). When pressures were increased to the maximum value regarded as 'safe' for the autoclave, the breakdown of carbon microspheres was almost complete and more complex forms of carbon with holes in the structure had formed (Figure 7.5c & d). The carbonaceous products which formed when 800 kPa

N_2(g) had been added, were more sausage like (Figure 7.5d). In addition more sheet-like carbonaceous materials were also present. The change from carbon microspheres to nanonecklaces and sheet-like materials were consistent with observations from the Raman and thermal analyses (Sections 7.3 & 7.4).

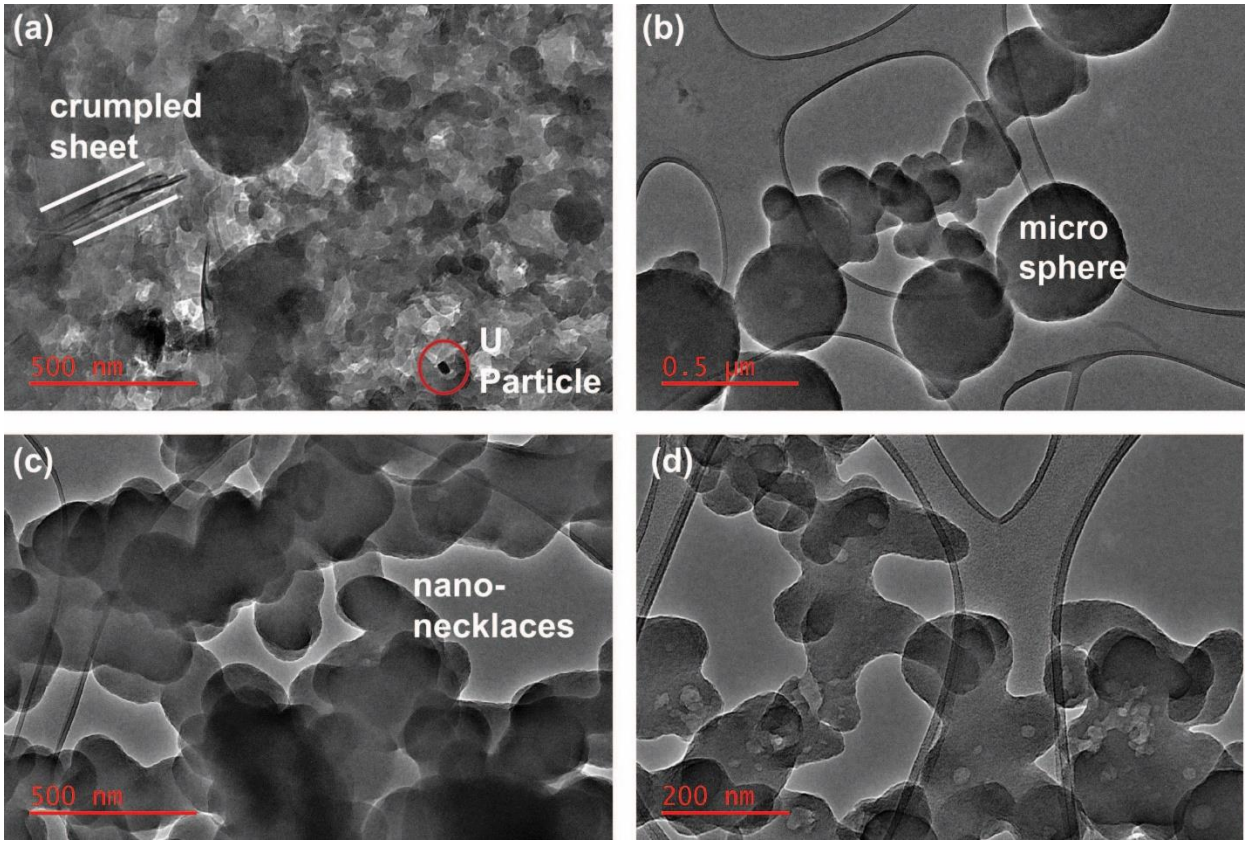


Figure 7.5 TEM of Solvothermal products formed on HILG13 32-75µm powders
(a)Mass of unstructured carbonaceous materials produced at 180°C, also seen are crumpled sheets of carbon and a uranium-rich particle from the granitic powder (U Particle). (b) With 400 kPa N_2 (g) added, the microspheres break down into nanobeads. (c). When 800 kPa N2 (g) was added nanonecklaces formed (d) also seen at higher pressures (800 kPa N2 (g) added) were holes in the CNSs.

7.6 Gold in Solution: Replicating Au-U-C associations

Although the results in the previous section had shown that carbonaceous materials could be precipitated onto uranium-bearing phases, one last component was needed to complete the understanding of Au-U-C associations in the Witwatersrand Basin – the role of gold. Therefore, it was imperative to determine whether gold dissolved in a solution was precipitated when carbonaceous products are formed in the presence of an uraniferous powder. In order to

determine this, aurichloric acid was added to the solvothermal conditions where the greatest deposit of carbonaceous materials were observed. Consequently, a set of solvothermal reactions with the HILG13 <32 μm powder were conducted where 20 mL of a ~0.1 M aurichloric acid ($HAuCl_4$) solution was combined with 60 mL of 0.05M sucrose solution and run at 180°C (along with 800kPa N_2(g)), for 18 h. The resulting solution was observed to have been vastly different in appearance to the solvothermal product solutions. Instead of having formed an opaque black suspension as before, here the resultant liquid was yellow-coloured and contained black particles. Figure 7.6 shows the different physical appearance of the product that was obtained from a solvothermal reaction which involved a gold solution, compared to the standard solvothermal reaction conditions (Figure 7.1). As before, some black products had also precipitated onto the thermocouple inside the Teflon inner cup. These products were similar to the black fine-grained solid masses previously observed (see Section 7.2), however a yellow-brown discolouration was noted that was different.

Based upon these observations it was clear that something had changed from the previous set of reactions. In order to confirm this, the concentration of gold in solution was measured with ICP-OES before and after the reaction. The initial concentration of aurichloric acid in solution was found to be ~ 1362 ppm Au. However, after the reaction had taken place this was drastically reduced to ~ 0.55 ppm Au (see Appendix J). Therefore, gold had been removed from solution. However, in order to confirm that it was the carbonaceous products that facilitated gold precipitation, a blank experiment was run. The blank was run under the exact same conditions as the previous gold experiment (HILG13 <32 μm powder with 20 mL of a ~0.1 M aurichloric acid ($HAuCl_4$) solution), however the sucrose solution was replaced with 60 mL of deionised water. With the carbon source removed there was still precipitation of gold particles, although the size was significantly larger and more visible in the reaction vessel (~300 – 800 μm). ICP-OES results of the blank showed that although gold had precipitated, significantly more gold was left in solution – 319 ppm Au compared to the solution that contained sucrose (~0.55 ppm Au).

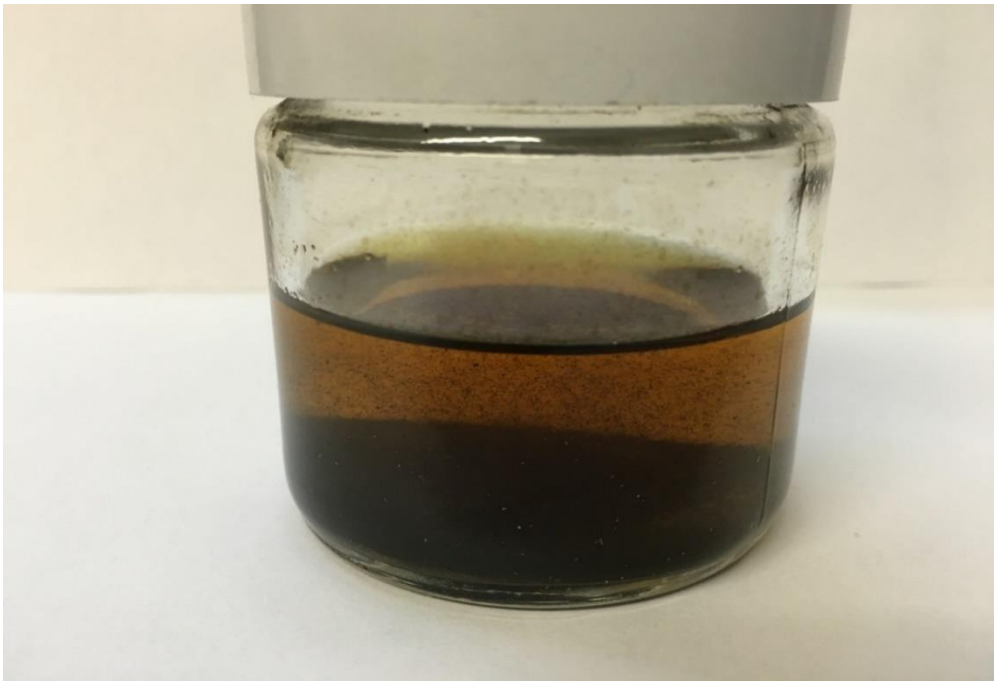


Figure 7.6 Solution produced by solvothermal gold in solution experiment
The solution formed by adding $HAuCl_4$ into sucrose solution, HILG13 <32 µm at 180°C with 800kPa N_2 (g) added over 18hrs.

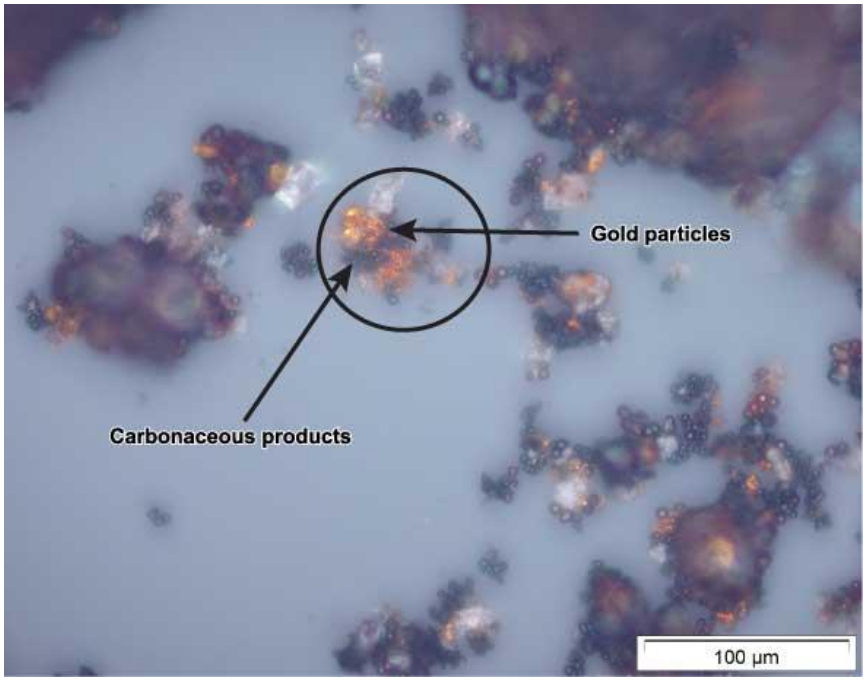


Figure 7.7 Optical microscope image of the solvothermal products formed from the gold in solution solvothermal experiment
Products formed from the reaction that had occurred between: sucrose, HILG13 <32 µm and $HAuCl_4$ at 180°C with 800kPa N_2 (g) added over 18 h. Carbonaceous products adhered to silicate materials, and crystalline gold particles adhered to the surface of the carbonaceous material.

The gold products were centrifuged and dried at 50°C for 2 h. The dried powder was then mounted under an optical microscope to establish what had become of the gold. Microscopy confirmed that gold, from the sucrose-aurichloric acid solution had precipitated (Figure 7.7). It was observed that the gold particles were crystalline in appearance and were preferentially associated with the carbonaceous products (see arrows and encircled region in Figure 7.7). However, even though the solution appeared to have different carbon forms, the predominant one that was observed under TEM appeared to be carbon microspheres (Figure 7.7). In addition to the larger forms of gold, nanoparticles of gold were also common in the solvothermal product. These particles were observed to have been coated with sheet-like carbonaceous products (Figure 7.8).

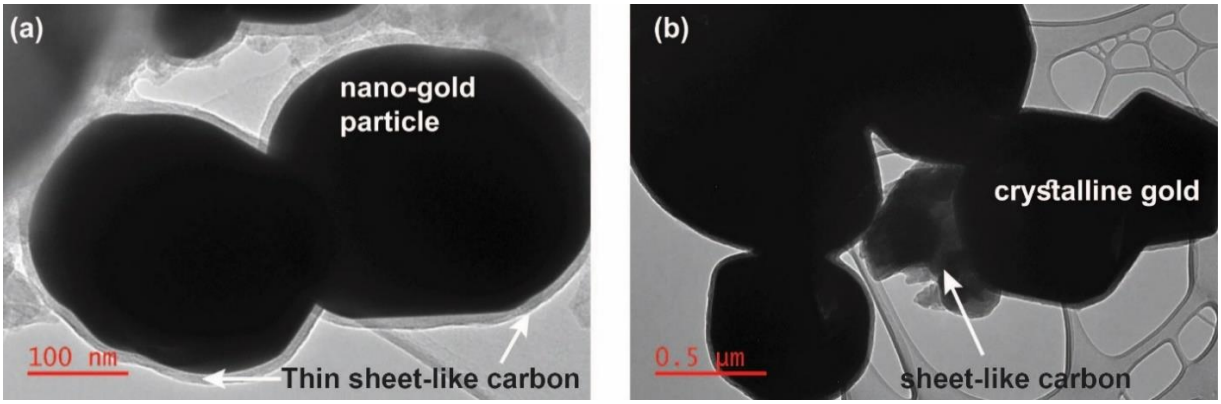


Figure 7.8 TEM images of gold products precipitated from a gold solution
Images show (a) Gold nanoparticles surrounded by carbonaceous materials and (b) Crystalline gold adjacent to sheet-like carbonaceous materials.

Some of these nanoparticles of gold were also crystalline in appearance. The Raman data also indicated a change in carbonaceous products, typically HILG13 <32 µm samples reacted at 180°C, with 800 kPa of N_2 (g) added, had I_D/I_G ratios of 0.55. However, with the addition of aurichloric acid the I_D/I_G ratios had increased to 0.60. This indicated that the gold in solution also had an effect of the precipitation of CNSs in solvothermal reactions, making the carbonaceous products less ordered than before.

7.7 Discussion

Hydrothermal processes provide a simple mechanism for C-U associations that can be replicated (Chapter 5). Previous research has provided evidence for oil migration in the Witwatersrand Basin (England et al., 2002) and later precipitation of hydrocarbons around detrital uraninite (Schidlowski, 1981; Drennan and Robb, 2006). The results presented in this solvothermal research, provided additional insights into the possible interactions of C-U formation of the Witwatersrand Basin.

C-U associations were simulated in Chapter 5. Conditions used in CCVD experiments required higher temperatures and a simple gaseous carbon source to replicate carbon seam precipitation than generally accepted for the Witwatersrand Basin. The technique adapted in this research successfully precipitated carbonaceous products from a solution onto the same uranium-bearing powders used in Chapter 5.

In these reactions the solvothermal conditions used resulted in the successful precipitation of an aqueous hydrocarbon from solution as CNSs. The carbonaceous products formed under these conditions displayed a greater degree of order (i.e. were more graphitic) than products synthesised by the CCVD technique. Additionally, lower temperatures for the precipitation of carbon were simulated by the solvothermal technique. Sucrose represented a different source of carbon than acetylene – the sucrose had more bonds that were required to be broken before new bonds could be formed. One consequence of this (as well as the reduced reaction temperature) was a smaller amount of complex carbon nanotubes, nanospirals and nanohelixes formed in comparison to the products formed by CCVD. The sucrose therefore represented a source more closely resembling decomposed biogenic hydrocarbons as the carbon source proposed for Witwatersrand Reefs (Mossman et al., 2008). The effect of pressure (at constant reaction temperature) in these experiments was to enhance the rate at which the pyrolised sucrose microspheres broke down to form microbeads, nano-necklaces and finally sheet-like carbonaceous materials. The graphitic signature also increased at higher pressures, although the thermal maxima (provided by TGA) were lowered as the bonds in the nanospheres were broken and reformed into sheet-like materials. Increased reaction pressure demonstrated that higher

pressures led to increased sheet-like structure formation. Such sheet-like materials were more similar to those observed in the Witwatersrand Basin carbonaceous materials e.g. TEM of CLR (Chapter 5). The pressures utilised demonstrated the effect of adding up to 800 kPa into the system, which is considerably lower than pressures estimated for the Witwatersrand Basin which are suggested to be between 150,000 – 300,000 kPa (Phillips, 1987; Phillips and Law, 1994). Such conditions could not safely be replicated under laboratory conditions in this study. The nature of the pressure in the experiments is also different. Experimental pressures are enhanced using N_2 (g) which is different from fluid pressure in a lithostatic system. However, the intention of the added pressure is to compress the fluid and enhance the pyrolysis of the hydrocarbon to produce sheet-like carbon structures as observed in Witwatersrand sample material.

Nevertheless, carbon is theorised to have formed in reefs where the pressure was reduced as compared to lithostatic pressure in the surrounding rocks, allowing for seams to grow preferentially inwards (akin to pegmatites or quartz veins (Chapter 6). It is vital to take stock of the processes being demonstrated in these experiments. Once again the experimental conditions are limited compared to geological conditions. However, the decomposition of the sucrose molecules demonstrates the pyrolysis of hydrocarbons. Complex hydrocarbons are broken up creating lighter hydrocarbons that are able to interact with metallic catalysts. Therefore, the effect of metallic catalysts and uranium-bearing minerals is to enhance and alter the formation of sheet-like carbonaceous materials. This effect demonstrates the benefit of using a simple, pure and well-researched hydrocarbon source such as sucrose.

The most striking evidence of gold re-precipitation has been observed in solvothermal studies when gold, in solution, was added to replicate the rich-gold mineralisation precipitated in Witwatersrand carbon seams. Gold successfully precipitated out of solution under the maximum solvothermal conditions. The ICP-OES data showed just how effective the precipitation was, removing almost all of the gold from the solution. Optical images revealed that the precipitated gold appeared to be crystalline and the colour of the gold products was consistent with native gold, rather than a gold oxide (confirmed with TEM EDS in Appendix J). The blank experiment, where sucrose was removed and replaced with deionised water, demonstrated that with the carbon source removed the precipitation of gold is significantly reduced. Moreover, the gold

particles tended to crystallise in contact with the carbonaceous products. TEM showed that gold formed as hexagonal crystalline forms and in many instances occurred as nanoparticles. The presence of these small particles is significant, as one of the concerns regarding gold mineralisation in the Witwatersrand Basin is the small nature of the gold particles (Frimmel and Hennigh, 2015). The experimentally precipitated particles of gold were also covered in a fine layer of carbonaceous material. The significance of the carbon layer is that it demonstrates that the precipitation of gold is due to an interaction with the carbon itself, not just a change in P-T conditions or redox conditions. Although a redox effect might have played a role, as is evidenced by the precipitation of gold in the blank solvothermal experiment, the effect of the carbon is pivotal in this instance (as is shown by the gold experiment that did not contain any sucrose).

The experiments in this Chapter provided proof of concept – uranium and other heavy detrital minerals provided sites for structured carbonaceous matter to form. High reaction pressure caused an increase in sheet-like carbonaceous materials and the precipitation of carbon caused gold in solution to precipitate out. Thus the author argues that, while there are still conditions that are difficult to replicate experimentally, the possible mechanisms that formed Au-U-C associations in the Witwatersrand Basin have been successfully demonstrated using uranium and metal catalysis.

7.8 Conclusions

- Solvothermal experiments successfully precipitated carbonaceous products onto uranium-bearing powders from a solution at 180°C, over 18 h in an autoclave.
- As the reaction pressure was increased sucrose broke down, from pyrolised carbon microspheres, to nanobeads to nano-necklaces to sheet-like materials.
- When reaction pressures were raised to 800 kPa (through added nitrogen gas) more abundant sheet-like carbon nanomaterials were formed.
- In order to simulate Au-U-C associations of the Witwatersrand Basin, gold in an aurichloric solution was added.
- Gold in solution precipitated out as crystalline gold and nanoparticles of gold, both of which have been observed under non-experimental conditions in the Witwatersrand carbon.

- The sucrose solution was highly effective at precipitating gold out of solution, and almost all of the ~1362 ppm Au was crystallised.
- In comparison, in a blank solution with sucrose removed, ~320 ppm Au remained dissolved in solution after reaction. The form of the gold in this blank solution was also significantly larger than the nano-particulate gold formed in the sucrose-aurichloric acid solution.
- Carbonaceous products that covered the gold showed a direct association between C and Au under experimental conditions.
- Although not all geological conditions could be matched, the experiments show that Au-U-C associations from the Witwatersrand Basin can be experimentally replicated.

8 Discussion and Conclusion

8.1 Discussion and Summary of Findings

Carbon seams were investigated using petrography (Chapter 3) and electron microscopy. It is well known that sedimentary features are abundant in the Witwatersrand Reefs (Feather and Koen, 1975; Minter et al., 1988). However, petrography showed that in the sampled carbonaceous reefs, gold and hydrocarbon displayed features attributed to remobilisation. Gold textures observed included veinlets, rims on oxide grains, micro-particles in phyllosilicates and secondary quartz growths, inclusions in secondary pyrite grains and micro-particles in carbon seams and nodules. These textures indicate that gold was remobilised in a fluid and precipitated out as secondary features under suitable conditions. Hydrocarbon textures further support remobilisation in the samples. Textures included carbon nodules encased in carbon spindles and carbon nodules infilling interstitial spaces in between quartz grains. These observations support the notion of multiple generations of hydrocarbon fluids present in the Witwatersrand sediments (see Sections 1.7.4 and 1.9).

The most important naturally occurring hydrocarbon features were observed using SEM. The images of the carbon nodule contained in crystalline pyrite from a dyke displayed the sheet-like nature of carbonaceous matter in what can only be described as a hydrothermal sample. These sheet-like hydrocarbon forms contained pyrite and gold microcrystals in small vesicles (or bubbles) within the carbon. In the same sample, hydrocarbon was observed as fibres in the space between adjacent carbon nodule and the host pyrite crystals. These forms (sheets and fibres) represent a more structured, graphitic carbon. Thus, some structuring process must have been present during the mineralisation from hydrocarbon fluids in the Witwatersrand Basin. This visual confirmation of micron-scale hydrothermal gold and fibrous hydrocarbons in a hydrothermal sample is a critical finding that is unique to this study.

Such compounding evidence supports a modified placer model (e.g. Robb and Meyer, 1995; Robb et al., 1997; Fuchs et al., 2014) and provides the best framework for further research into the formation of Au-U-C associations of the Witwatersrand Basin.

An investigation into the elemental composition of carbon seams and nodules provided evidence for the processes involved in remobilisation of hydrocarbons (Chapter 4). The hydrocarbon textures were further examined using PIXE micro-mapping. Gold in samples investigated occurred between carbon spindles with micro-particles dispersed within the spindles. The hydrocarbons contained numerous additional mobile elements including Al, K, P and Ca. Most notably there was also dispersed S within the carbonaceous materials. The presence of sulphur within the hydrocarbons is linked to organic sulphur compounds derived from the degradation of kerogens. Organic sulphur compounds provide additional evidence of a kerogen derived liquid hydrocarbon and sulphur. It is theorised that sulphur in hydrocarbons enhance the ability of the organic compounds to complex with metals (Section 4.4).

Hydrocarbons have been identified in fluid inclusion studies. Multiple types of fluid systems containing simple hydrocarbon sources (H_2O-CH_4-CO_2, CH_4-N_2 rich fluid population) could have been capable of forming organo-urano-gold-carbon complexes that could have precipitated out in the presence of detrital uraninite (Drennan, 1997; Drennan and Robb, 2006). Numerous elements were concentrated in and around the solid hydrocarbon phases in this study, indicating there may have been an additional process involved in concentrating elements such as Fe, Cu, Ni, Co, Au, U, Cr, V, Mn, Hg, Ag and Ti

Consequently, parameters from literature and the investigations in Chapter 3 and 4, provided a framework to simulate the C-U associations. Although radiolysis and pyrolysis of hydrocarbons has been researched, the role of metals, and specifically uranium, in hydrocarbon growth was relatively unknown. CCVD experiments successfully precipitated solid carbon nanomaterials from a gas phase onto uranium-bearing powders. This is significant as it provides a framework and mechanism for hydrothermally structured hydrocarbons to precipitate around uranium-bearing phases. In the experiments U, Cu, Sr and Mo were strongly correlated with hydrocarbon precipitation. However, when c.a. 50% U was leached out, there was a 35% reduction in the formation of carbonaceous products. Thus it was confirmed that while Cu, Sr and Mo in the powder substrate played some role in formation of carbonaceous products, the most significant role was played by the U content.

The growth of these structures displayed similarities in Raman signature (especially at 450°C) to the carbonaceous materials from the Witwatersrand Basin. The form of the friable carbonaceous products experimentally precipitated was similar to what was observed in seam carbon in the Witwatersrand Basin. Experimental products were compared to Witwatersrand carbon using TEM images of a powdered CLR sample. These images revealed that Witwatersrand carbon was sheet-like in form and encompassed uraninite, which was similar to the solid carbonaceous products formed during the experiments. Similarly, SEM images of a Witwatersrand Beisa Reef ore block were compared to an ore block of experimentally grown carbon. The experimentally grown carbonaceous products demonstrated that carbonaceous materials can precipitate onto uraninite grains. These experimentally grown carbon forms replicated the sheet-like structures and fibrous/tube-like structures observed in precipitated hydrocarbons (Chapter 3). This provides a key link in the precipitation of hydrothermal carbonaceous matter which is introduced in this study. Although pyrolysis or radiolysis of liquid hydrocarbons via radiation from uranium-bearing phases is an important process, the PIXE micromaps indicated that a metal component was distributed in Witwatersrand carbonaceous matter. This can be explained by the mechanism of carbon ordering known from the growth of CNSs. Carbonaceous materials formed by catalytic growth is theorised to receive electrons from metals called 'electron promoters' during formation (Deshmukh et al., 2010). Electron promoters are included within the CNSs. Therefore, it is proposed that radiolysis and pyrolysis of hydrocarbons formed a component of hydrocarbon growth in the Witwatersrand Basin. However, a significant part of the hydrocarbon growth is attributed to the process of electron promotion and catalysis of uranium and other metals.

Gold is the critical component in the Witwatersrand Au-U-C associations, and to date no data has been published (to the authors knowledge) that illustrates the form and three dimensional distribution of gold throughout a carbon seam. Consequently, a carbon seam with exceptional gold grades was examined using µCT and Auto-SEM-EDS (Chapter 6). Results showed that gold and phyllosilicates occur between carbon spindles. Small amounts of gold and phyllosilicates were also observed as inclusions within carbon spindles. The spindles of the carbon seam grew principally perpendicular to the bounding surfaces – the conglomerate footwall and quartzite hanging wall. Spindles of hydrocarbon displaced around some rounded grains. Gold

concentrations were highest at the bounding surfaces of the carbon seam, decreasing towards the centre. The form of the carbon spindles along with the inclusion of gold and phyllosilicates in the spindles indicate that the spindles of hydrocarbon grew parallel to the direction of principle stress (akin to quartz crystal growth in veins). It is argued that growth in this manner accounts for the decrease in gold concentration towards the centre of the carbon seam. Thus hydrocarbon fluids were confirmed to have moved into the lower pressure, more permeable layers of the sediments. This is a strong indication that physical processes played an important role in the orientation of structured carbonaceous matter in the carbon seams.

The most striking results presented in this thesis show that it is possible to experimentally simulate a hydrothermal mechanism for the formation Au-U-C associations in the Witwatersrand Basin. Solvothermal experiments (Chapter 7) were designed to demonstrate that dissolved gold and hydrocarbons could be precipitated from a prepared solution. Initial solvothermal experiments successfully precipitated carbon microspheres onto uranium-bearing powders from a sucrose solution (which roughly represented carbon derived from decayed organic organisms). The carbonaceous products formed at 180°C over 24 h, which is lower than temperatures observed during the formation of CCVD products (Chapter 5). Thus it was demonstrated that more carbonaceous product masses could be precipitated at lower temperatures when reacted for longer time intervals. The effect of pressure on carbon product formation was demonstrated with solvothermal experiments. Increasing pressure enhanced the breaking of bonds in the pyrolised sucrose, thus creating smaller more reactive hydrocarbon compounds and changing the form of CNSs from carbon spheres to sheet-like materials.

Gold in solution was added to these experiments in order to simulate Au-U-C associations. When a fixed concentration of a gold solution was added, the aqueous gold precipitated out as crystalline and nano-particulate gold. Both optical images and TEM micrographs confirmed that gold had formed crystals from the aurichloric solution. ICP-OES results revealed that almost all the gold in solution, in the presence of sucrose, was precipitated by the solvothermal process. In the absence of any sucrose only limited gold was precipitated. Additionally, nanoparticles of gold were seen to be coated with the carbonaceous products. This indicated that carbon precipitation was directly related to gold precipitation.

Solvothermal experimentation provides a potential proxy to organic fluids derived from Type I kerogens in the Archean Witwatersrand Basin. For example, in the Witwatersrand Basin the carbon source (suggested to be cyanobacteria or algae from the lower shale units) broke down into various petroleum compounds and became remobilised during metamorphism. The metamorphic fluids would be rich in gold as is demonstrated by inclusions of gold in remobilised hydrocarbons (Drennan and Robb, 2006). These gold and hydrocarbon rich fluids would have been transported to sites with high concentrations of uraninite and other metal catalysts. The precipitation of carbonaceous products facilitated an interaction between hydrocarbon and gold that caused gold to precipitate as micro-particles, coatings on spindles and inclusions within solid hydrocarbon materials.

Experimental conditions cannot match geological conditions postulated for the Witwatersrand Basin. However, this novel experimental approach to simulating the Au-U-C associations serves as a first approximation at the best achievable conditions. Gold, uranium and carbonaceous matter interacted in a complex array of processes that have been explored in this thesis. However, further experiments are required to more closely simulate geological conditions.

8.2 Implications

The results of this thesis significantly enhance our understanding of possible processes involved in the formation of Au-U-C associations in the Witwatersrand Basin. The petrography and PIXE provide a significant study of carbonaceous products from the Witwatersrand Basin. Utilising museum collections from currently mined-out reefs, current mine samples and samples from private collections that had not previously been available for research purposes, meant that this research was able to include many more examples of mineralisation from across the Central Rand Group. Along with µCT 3D rendered data and the two experimental techniques, new knowledge and new methodologies have been applied to the Witwatersrand Basin research. As a result the evidence in favour of the epigenetic origin of carbonaceous materials in the Witwatersrand Basin has been strengthened. While mining operations will continue to use sedimentary markers to guide operations, the case is made here that more thorough investigations into carbonaceous

materials and secondary features could enhance recovery. Additionally, models for mineralisation and exploration that do not consider the role of fluid remobilisation, and the existence of complex, multi component Au-U-C complexes, should be revised. Other deposits that contain significant amounts of carbonaceous materials and uranium-bearing minerals could apply the findings of the current research to better understand the Au-C associations in those deposits. An example of such a deposit is the Athabascan Basin where metamorphic rocks contain high concentrations of uranium mineralisation (Jefferson et al., 2007) in association with carbon. Similarly Cigar Lake exhibits an association between carbon and uranium (Landais et al., 1993). A comparative study to these deposits could refine some of the arguments developed in this study.

In the context of the Athabascan Basin, research postulates that zonation with large isotopic variations in $\delta^{13}C$ values for the solid bitumen indicates an alternative mechanism for formation (Sangély et al., 2007). The research proposes the bitumen in the Athabascan Basin was formed by the catalytic hydrogenation of CO_2 rather than the radiolysis of a petroleum product (Sangély et al., 2007). However, this cannot be applied to the Witwatersrand carbonaceous materials. Experiments that catalyse CO_2 as a supercritical fluid require temperatures in excess of 650°C and carefully prepared catalysts (Deshmukh et al., 2010). Therefore, it would be difficult to reconcile the hydrogenation of CO_2 with the low temperatures (~350°C average) and the biogenic origin (carbon isotope values) found in the Witwatersrand Basin. Instead a more robust array of hydrocarbons derived from a biogenic origin and a natural metal rich catalyst represents a process that can adapt to variations in the mineralogy of the Witwatersrand Reefs.

Research in the field of heterogeneous catalysis also benefits from the results of the current experimentation in this study. The catalytic effect of U was effectively shown and replicated. Here the use of natural materials as a substrate for CNSs formation was also enhanced. The addition of gold in solution demonstrated the efficiency of carbon deposition as a platform for metal precipitation. While these results demonstrate the mechanisms involved, there are also potential technological applications. Natural products could make synthesising nanostructured metal and non-metal materials cheaper.

8.3 Recommendations

While the investigation presented in this thesis was designed to encompass as many aspects of Au-U-C associations as possible, a few topics could be investigated further. The effect of radiation from uranium on CNSs formation remains a hypothesis. Carefully designed, interdisciplinary experiments could determine the mechanisms involved using material that has the degree of radiation that uraninite would have possessed during Archaean times, thus more effectively modelling conditions prevalent during the precipitation of the Witwatersrand mineralisation. The effect of pressure was demonstrated, but under the current experimental conditions it was not possible to simulate the lithostatic pressure conditions that the Witwatersrand Basin would have experienced. Collaborative high-pressure experimentation would be beneficial to better understanding conditions at the time of mineralisation.

Additionally, a complex multi-process set of experiments that could account for the biogenic signature of carbon in the Witwatersrand Basin (possibly by breaking down algae or type I kerogens), before solvothermal reactions involving gold in solution, could be useful. These studies would fall outside of the scope of this thesis, but might provide answers to the remaining critical topics of debate surrounding the Witwatersrand Au-U-C associations.

References

Agangi, A., Hofmann, A., Rollion-Bard, C., Marin-Carbonne, J., Cavalazzi, B., Large, R., Meffre, S., 2015. Gold accumulation in the Archaean Witwatersrand Basin, South Africa — Evidence from concentrically laminated pyrite. Earth-Science Reviews **140**, pg 27–53.

Agangi, A., Hofmann, A., Wohlgemuth-Ueberwasser, C.C., 2013. Pyrite zoning as a record of mineralization in the ventersdorp contact reef, Witwatersrand Basin, South Africa. Economic Geology **108**, pg 1243–1272.

Anglogold Ashanti, 2015. Mineral Resource and Ore Reserve Report 2015.

Armstrong, R.A., Compston, W., Retief, E.A., Williams, I.S., Welke, H.J., 1991. Zircon ion microprobe studies bearing on the age and evolution of the Witwatersrand triad. Precambrian Research **53**, 243–266.

Barnicoat, A.C., Henderson, I.H.C., Knipe, R.J., Yardley, B.W.D., Napler, R.W., Fox, N.P.C., Kenyon, A.K., Mintingh, D.J., Strydom, D., Winkler, K.S., Lawrence, S.R., Cornford, C., 1997. Hydrothermal gold mineralization in the Witwatersrand basin. Nature **386**, pg 820–824.

Cairncross, B., 2004. Field Guide to Rocks & Minerals of Southern Africa, Field Guide Series. Penguin Books, Johannesburg, South Africa, 288 pp

Catuneanu, O., Biddulph, M.N., 2001. Sequence stratigarphy of the Vaal Reef facies associations in the Witwatersrand foredeep, South Africa. Sedimentary Geology **141-142**, pg 113–130.

Coleman, J.N., Khan, U., Blau, W.J., Gun'ko, Y.K., 2006. Small but strong: A review of the mechanical properties of carbon nanotube–polymer composites. Carbon **44**, pg 1624–1652.

Collins, A., 1975. Geochemistry of oilfield waters. Elsevier, New York, 496 pp.

Cousins, C.A., 1973. Platinoids in the Witwatersrand system. Journal of the South African Institute of Mining and Metallurgy **73**, pg 184–199.

Coville, N.J., Mhlanga, S.D., Nxumalo, E.N., Shaikjee, A., 2011. A review of shaped carbon nanomaterials. South African Journal of Science **107 (4)**, pg 1-15

Dankert, B.T., Hein, K.A., 2010. Evaluating the structural character and tectonic history of the Witwatersrand Basin. Precambrian Research **177**, pg 1–22.

Davis, G.H., Reynolds, S.J., Kluth, C., Kluth, C.F., 2012. Structural Geology of Rocks and Regions. Wiley, 776 pp.

Depiné, M., Frimmel, H.E., Emsbo, P., Koenig, A.E., Kern, M., 2013. Trace element distribution in uraninite from Mesoarchaean Witwatersrand conglomerates (South Africa) supports placer model and magmatogenic source. Mineralium Deposita **48**, pg 423–435.

Deshmukh, A.A., Mhlanga, S.D., Coville, N.J., 2010. Carbon spheres. Materials Science and Engineering R: Reports **70**, pg 1–28.

Drennan, G.R., 1997. Fluid Inclusion Microthermometry of the Witwatersrand Basin. PhD Thesis, University of the Witwatersrand, pp. 228

Drennan, G.R., Boiron, M.C., Cathelineau, M., Robb, L.J., 1999. Characteristics of post-depositional fluids in the Witwatersrand Basin. Mineralogy and Petrology **66**, pg 83–109.

Drennan, G.R., Robb, L.J., 2015. Hydrocarbons , fluids and metal redistribution in the Witwatersrand Basin , South Africa, in: SGA 13th Biennial Meeting. Nancy, France, pg. 3–6.

Drennan, G.R., Robb, L.J., 2006. The nature of hydrocarbons and related fluids in the Witwatersrand Basin, South Africa: Their role in metal redistribution. Processes on the Early Earth, Special Papers **405 2405**, pg 353–386.

Dupuis, A., 2005. The catalyst in the CCVD of carbon nanotubes—a review. Progress in Materials Science **50**, pg 929–961.

Durbach, S.H., Krause, R.W., Witcomb, M.J., Coville, N.J., 2009. Synthesis of branched carbon nanotubes using copper catalysts in a hydrogen-filled DC arc-discharger. Carbon **47**, pg 635–644.

England, G.L., Rasmussen, B., Krapez, B., Groves, D.I., 2002. Archaean oil migration in the Witwatersrand Basin of South Africa. Journal of the Geological Society **159**, pg 189–201.

Feather, C.E., 1976. Mineralogy of platinum-group minerals in the Witwatersrand, South Africa. Economic Geology **71**, pg 1399-1428

Feather, C.E., Koen, G.M., 1975. Mineralogy of the Witwatersrand Reefs. Minerals Science and Engineering **7**, pg 198–224.

Ferrari, A., 2001. Model to Interpret the Raman Spectra of Disordered, Amorphous and Nanostructured Carbons, in: Materials Research Society. pp. 5–12.

Ferrari, A., Robertson, J., 2000. Interpretation of Raman spectra of disordered and amorphous carbon. Physical Review **B 61**, pg 14095–14107.

Filby, R.H., 1994. Origin and nature of trace element species in crude oils, bitumens and kerogens: implications for correlation and other geochemical studies. Geological Society, London, Special Publications **78**, pg 203–219.

Frimmel, H.E., Gartz, V.H., 1997. Witwatersrand gold particle chemistry matches model of metamorphosed, hydrothermally altered placer deposits. Mineralium Deposita **32**, pg 523–530.

Frimmel, H.E., Hallbauer, D.K., Gartz, V.H., 1999. Mineralogy and Petrology Gold mobilizing fluids in the Witwatersrand Basin : composition and possible sources. Mineralogy and Petrology **66**, pg 55–81.

Frimmel, H.E., Hennigh, Q., 2015. First whiffs of atmospheric oxygen triggered onset of crustal gold cycle. Mineralium Deposita **50**, pg 5–23.

Frimmel, H.E., Minter, W.E.L., 2002. Recent Developments Concerning the Geological History and Genesis of the Witwatersrand Gold Deposits , South Africa. Society of Economic Geologists **9**, pg 17–45.

Fuchs, S., Przybylowicz, W.J., Williams-Jones, A.E., 2014. Elemental imaging of organic matter and associated metals in ore deposits using micro PIXE and micro-EBS. Nuclear Instruments and Methods in Physics Research, Section B: Beam Interactions with Materials and Atoms **318**, pg 157–162.

Fuchs, S., Williams-Jones, A.E., Jackson, S.E., Przybylowicz, W.J., 2016a. Metal distribution in pyrobitumen of the Carbon Leader Reef, Witwatersrand Supergroup, South Africa: Evidence for liquid hydrocarbon ore fluids. Chemical Geology **426**, pg 45–59.

Fuchs, S., Williams-Jones, A.E., Przybylowicz, W.J., 2016b. The origin of the gold and uranium ores of the Black Reef Formation, Transvaal Supergroup, South Africa. Ore Geology Reviews **72**, pg 149–164.

Gartz, V.H., Frimmel, H.E., 1999. Complex metasomatism of an Archaean placer in the Witwatersrand Basin. Economic Geology **94**, pg 689–706.

Godel, B., Barnes, S.J., Maier, W.D., 2006. 3-D distribution of sulphide minerals in the Merensky Reef (Bushveld Complex, South Africa) and the J-M Reef (Stillwater Complex, USA) and their relationship to microstructures using x-ray computed tomography. Journal of Petrology **47**, pg 1853–1872.

Gray, G.J., Lawrence, S.R., Kenyon, K., Cornford, C., 1998. Nature and origin of “carbon” in the Archaean Witwatersrand Basin, South Africa. Journal of the Geological Society **155**, pg 39–59.

Guy, B.M., Ono, S., Gutzmer, J., Kaufman, A.J., Lin, Y., Fogel, M.L., Beukes, N.J., 2012. A multiple sulfur and organic carbon isotope record from non-conglomeratic sedimentary rocks of the Mesoarchean Witwatersrand Supergroup, South Africa. Precambrian Research **216-219**, pg 208–231.

Hall, R.C.B., Els, B.G., Mayer, J.J., 1997. The Ventersdorp Contact Reef: Final phase of the Witwatersrand basin, independent formation, or precursor to the ventersdorp supergroup? South African Journal of Geology **100**, pg 213–222.

Hallbauer, D.K., 1975. The plant origin of the Witwatersrand carbon. Minerals Science and Engineering **7**, pg 111–131.

Hayward, C.L., Reimold, W.U., Gibson, R.L., Robb, L.J., 2005. Gold mineralization within the Witwatersrand Basin, South Africa: evidence for a modified placer origin, and the role of the

Vredefort impact event. Geological Society, London, Special Publications **248**, pg 31–58.

Heinrich, C.A., 2015. Witwatersrand gold deposits formed by volcanic rain, anoxic rivers and Archaean life. Nature Geoscience **8**, pg 2–5.

Horscroft, F.D.M., Mossman, D.J., Reimer, T.O., Hennigh, Q., 2011. Witwatersrand Metallogenesis : the Case for (Modified) Syngenesis. Society for Sedimentary Geology Special Edition **101**, pg 75–95.

Jefferson, C.W., Thomas, D.J., Gandhi, S.S., Ramaekers, P., Delaney, G., Brisbin, D., Cutts, C., Portella, P., Olson, R.A., 2007. Unconformity-associated uranium deposits of the Athabasca Basin, Saskatchewan and Alberta. Bulletin-Geological Survey of Canada **588**, 23 pp.

Jolley, S.J., Freeman, S.R., Barnicoat, A.C., Phillips, G.N., Knipe, R.J., Pather, A., Fox, N.P.C., Strydom, D., Birch, M.T.G., Henderson, I.H.C., Rowland, T.W., 2004. Structural controls on Witwatersrand gold mineralisation. Journal of Structural Geology **26**, pg 1067–1086.

Jolley, S.J., Stuart, G.W., Freeman, S.R., Knipe, R.J., Kershaw, D., McAllister, E., Barnicoat, A.C., Tucker, R.F., 2007. Progressive evolution of a late orogenic thrust system, from duplex development to extensional reactivation and disruption: Witwatersrand Basin, South Africa. Geological Society, London, Special Publications **272**, pg 543–569.

Kharaka, Y.K., Maest, A.S., Carothers, W.W., Law, L.M., Lamothe, P.J., Fries, T.L., 1987. Geochemistry of metal-rich brines from central Mississippi Salt Dome basin, U.S.A. Applied Geochemistry **2**, pg 543–561.

Kirk, J., Ruiz, J., Chesley, J., Titley, S., Walshe, J., 2001. A detrital model for the origin of gold and sulfides in the Witwatersrand basin based on Re-Os isotopes. Geochimica et Cosmochimica Acta **65**, pg 2149–2159.

Koglin, N., Frimmel, H.E., Minter, W.E.L., Brätz, H., 2010a. Trace-element characteristics of different pyrite types in Mesoarchaean to Palaeoproterozoic placer deposits. Mineralium Deposita **45**, pg 259–280.

Koglin, N., Zeh, A., Frimmel, H.E., Gerdes, A., 2010b. New constraints on the auriferous

Witwatersrand sediment provenance from combined detrital zircon U-Pb and Lu-Hf isotope data for the Eldorado Reef (Central Rand Group, South Africa). Precambrian Research **183**, pg 817–824.

Krasheninnikov, A.V., Nordlund, K., 2004. Irradiation effects in carbon nanotubes. Nuclear Instruments and Methods in Physics Research Section B: Beam Interactions with Materials and Atoms **216**, pg 355–366.

Kuang, Q., Xie, S.Y., Jiang, Z.Y., Zhang, X.H., Xie, Z.X., Huang, R. Bin, Zheng, L.S., 2004. Low temperature solvothermal synthesis of crumpled carbon nanosheets. Carbon **42**, pg 1737–1741.

Kyle, J.R., Ketcham, R.A., 2003. In situ distribution of gold in ores using high-resolution X-ray computed tomography. Economic Geology **98**, pg 1697–1701.

Landais, P., Dubessy, J., Dereppe, J.-M., Philp, R.P., 1993. Characterization of graphite alteration and bitumen genesis in the Cigar Lake deposit (Saskatchewan, Canada). Canadian Journal of Earth Sciences **30**, pg 743–753.

Landais, P., Dubessy, J., Poty, B., Robb, L.J., 1990. Three examples illustrating the analysis of organic matter associated with uranium ores. Organic Geochemistry **16**, pg 601–608.

Large, R., Meffre, S., Burnett, R., Guy, B., Bull, S., Gilbert, S., Goemann, K., Danyushevsky, L., 2013. Evidence for an intrabasinal source and multiple concentration processes in the formation of the carbon leader reef, Witwatersrand Supergroup, South Africa. Economic Geology **108**, pg 1215–1241.

Li, Z., Dervishi, E., Xu, Y., Saini, V., Mahmood, M., Oshin, O.D., Biris, A.R., Biris, A.S., 2009. Carbon nanotube growth on calcium carbonate supported molybdenum-transition bimetal catalysts. Catalysis Letters **131**, pg 356–363.

Maclean, P.J., Fleet, M.E., 1989. Detrital pyrite in the Witwatersrand gold fields of South Africa: evidence from truncated growth banding. Economic Geology **84**, pg 2008–2011.

Magrez, A., Seo, J.W., Mikó, C., Hernádi, K., Forró, L., 2005. Growth of carbon nanotubes with

alkaline earth carbonate as support. Journal of Physical Chemistry **B 109**, pg 10087–10091.

Manzi, M.S.D., Durrheim, R.J., Hein, K. a. a., King, N., 2012. 3D edge detection seismic attributes used to map potential conduits for water and methane in deep gold mines in the Witwatersrand basin, South Africa. Geophysics **77**, WC133 – WC147.

Manzi, M.S.D., Gibson, M.A.., Hein, K.A.A., King, N., Durrheim, R.J., 2012. Application of 3D seismic techniques to evaluate ore resources in the West Wits Line goldfield and portions of the West Rand goldfield, South Africa. Geophysics **77**, WC163 – WC171.

Manzi, M.S.D., Hein, K.A.A., King, N., Durrheim, R.J., 2013. Neoarchaean tectonic history of the Witwatersrand Basin and Ventersdorp Supergroup: New constraints from high-resolution 3D seismic reflection data. Tectonophysics **590**, pg 94–105.

Mathur, R., Gauert, C., Ruiz, J., Linton, P., 2013. Evidence for mixing of Re-Os isotopes at <2.7Ga and support of a remobilized placer model in Witwatersrand sulfides and native Au. Lithos **164-167**, pg 65–73.

McCarthy, T.S., 2009. The Witwatersrand Supergroup, in: Johnson, M.R., Anhaeusser, C.R., Thomas, R.J. (Eds.), The Geology of South Africa. The Geological Society of South Africa, Johannesburg, South Africa, 619 pp.

Meier, D.L., Heinrich, C. a., Watts, M. a., 2009. Mafic dikes displacing Witwatersrand gold reefs: Evidence against metamorphic-hydrothermal ore formation. Geology **37**, pg 607–610.

Mellor, E.T., Banks, E.H., 1916. Geological Map of the Witwatersrand Gold Field. Department of Mines and Industries, Geological Survey.

Minter, W.E.L., 1999. Irrefutable detrital origin of Witwatersrand gold and evidence of Eolian signatures. Economic Geology **94**, pg 665–670.

Minter, W.E.L., 1976. Detrital gold, uranium, and pyrite concentrations related to sedimentology in the Precambrian Vaal Reef placer, Witwatersrand, South Africa. Economic Geology **71**, pg 157–176.

Minter, W.E.L., Feather, C.E., Glatthaar, C.W., 1988. Sedimentological and mineralogical aspects

of the newly discovered Witwatersrand placer deposit that reflect Proterozoic weathering, Welkom gold field, South Africa. Economic Geology **83**, pg 481–491.

Minter, W.E.L., Goedhart, M., Knight, J., Frimmel, H.E., 1993. Morphology of Witwatersrand gold grains from the Basal Reef: Evidence for their detrital origin. Economic Geology **88**, pg 237–248.

Moshkalyov, S.A., Moreau, A.L.D., Guttiérrez, H.R., Cotta, M.A., Swart, J.W., 2004. Carbon nanotubes growth by chemical vapor deposition using thin film nickel catalyst. Materials Science and Engineering: **B 112**, pg 147–153.

Mossman, D.J., Minter, W.E.L., Dutkiewicz, A., Hallbauer, D.K., George, S.C., Hennigh, Q., Reimer, T.O., Horscroft, F.D., 2008. The indigenous origin of Witwatersrand "carbon." Precambrian Research **164**, pg 173–186.

Motchelaho, M.A.M., Xiong, H., Moyo, M., Jewell, L.L., Coville, N.J., 2011. Effect of acid treatment on the surface of multiwalled carbon nanotubes prepared from Fe-Co supported on CaCO3: Correlation with Fischer-Tropsch catalyst activity. Journal of Molecular Catalysis A: Chemical **335**, pg 189–198.

Murowchick, J.B., Barnes, H.L., 1987. Effects of temperature and degree of supersaturation on pyrite morphology. American Mineralogist **72**, pg 1241–1250.

Myers, R.E., 1993. Sulphidation in the Witwatersrand Goldfields: Evidence from the Middelvlei Reef. Mineralogical Magazine **57**, pg 395–405.

Parnell, J., 1999. Petrographic evidence for emplacement of carbon into Witwatersrand conglomerates under high fluid pressure. Journal of Sedimentary Research **69**, pg 164–170.

Phillips, G.N., 2011. Origin of Witwatersrand gold: a metamorphic devolatilisation-hydrothermal replacement model. Applied Earth Science **120(3)**, pg 112 - 129.

Phillips, G.N., 1987. Metamorphism of the Witwatersrand Gold Fields - Conditions during Peak Metamorphism. Journal of Metamorphic Geology **5**, pg 307–322 ST

Phillips, G.N., Law, J.D.M., 2000. Witwatersrand Gold Fields: Geology, Genesis, and Exploration. SEG Review **13**, pg 439-500.

Phillips, G.N., Law, J.D.M., 1994. Metamorphism of the Witwatersrand gold fields: A review. Ore Geology Reviews **9**, pg 1–31.

Phillips, G.N., Myers, R.E., Palmer, J.A., 1987. Problems with the placer model for Witwatersrand gold. Geology **15**, pg 1027–1030.

Phillips, G.N., Powell, R., 2011. Origin of Witwatersrand gold: a metamorphic devolatilisation–hydrothermal replacement model. Applied Earth Science **120**, pg 112–129.

Pretorius, D.A., 1981. Gold and Uranium in Quartz-Pebble Conglomerates. Economic Geology **75th Anniversary Edition**, pg 117 – 138.

Pretorius, D.A., Brink, W.C.J., Fouché, J., 1986. Map of the Witwatersrand Basin: Surface and Subsurface Geology and Structure, in: Mineral Deposits of South Africa. Geological Society of South Africa, Johannesburg, South Africa.

Prozesky, V.M., Przybylowicz, W.J., van Achterbergh, E., Churms, C.L., Pineda, C.A., Springhorn, K.A., Pilcher, J.V., Ryan, C.G., Kritzinger, J., Schmitt, H., Swart, T., 1995. The NAC nuclear microprobe facility. Nuclear Inst. and Methods in Physics Research, **B 104**, pg 36–42.

Rasmussen, B., Fletcher, I.R., Muhling, J.R., Mueller, A.G., Hall, G.C., 2007. Bushveld-aged fluid flow, peak metamorphism, and gold mobilization in the Witwatersrand basin, South Africa: Constraints from in situ SHRIMP U-Pb dating of monazite and xenotime. Geology **35**, pg 931–934.

Reich, S., Thomsen, C., 2004. Raman spectroscopy of graphite. Philosophical transactions. Series A, Mathematical, physical, and engineering sciences **362**, pg 2271–2288.

Reimold, W.U., Gibson, R.L., 1996. Geology and evolution of the Vredefort impact structure, South Africa. Journal of African Earth Sciences **23**, pg 125–162.

Robb, L.J., Charlesworth, E.G., Drennan, G.R., Gibson, R.L., Tongu, E.L., 1997. Tectono-metamorphic setting and paragenetic sequence of Au-U mineralisation in the Archaean Witwatersrand Basin, South Africa. Australian Journal of Earth Sciences **44**, pg 353–371.

Robb, L.J., Davis, D.W., Kamo, S.L., 1991. U-Pb Ages on Single Detrital Zircon Grains from the Witwatersrand Basin, South Africa: Constraints on the Age of Sedimentation and on the Evolution of Granites Adjacent to the Basin: A Reply. The Journal of Geology **99**, pg 495–496.

Robb, L.J., Davis, D.W., Kamo, S.L., Meyer, F.M., 1992. Ages of altered granites adjoining the Witwatersrand Basin with implications for the origin of gold and uranium. Nature **357**, pg 677–680.

Robb, L.J., Meyer, M.F., 1995. The Witwatersrand Basin, South Africa: Geological framework and mineralization processes. Ore Geology Reviews **10**, pg 67–94.

Robb, L.J., Robb, V.M., 1998. Gold in the Witwatersrand basin. Mineral Resources of South Africa **16**, pg 294–349.

Rollinson, H.R., 2014. Using Geochemical Data: Evaluation, Presentation, Interpretation, Longman Geochemistry. Taylor & Francis.

Ryan, C.G., 2000. Quantitative trace element imaging using PIXE and the nuclear microprobe. International Journal of Imaging Systems and Technology **11**, pg 219–230.

Ryan, C.G., Cousens, D.R., Sie, S.H., Griffin, W.L., Suter, G.F., Clayton, E., 1990. Quantitative pixe microanalysis of geological matemal using the CSIRO proton microprobe. Nuclear Inst. and Methods in Physics Research, **B 47**, pg 55–71.

Ryan, C.G., Jamieson, D.N., 1993. Dynamic analysis: on-line quantitative PIXE microanalysis and its use in overlap-resolved elemental mapping. Nuclear Inst. and Methods in Physics Research, **B 77**, pg 203–214.

Ryan, C.G., Jamieson, D.N., Churms, C.L., Pilcher, J. V., 1995. A new method for on-line true-elemental imaging using PIXE and the proton microprobe. Nuclear Inst. and Methods in Physics Research, **B 104**, pg 157–165.

Saager, R., 1981. Geochemical Studies on the Origin of the Detrital Pyrites in the Conglomerates of the Witwatersrand Goldfields, South Africa, in: Genesis of Uranium- and Gold-Bearing Precambrian Quartz-Pebble Conglomerates. Golden, Colorado.

SACS, 1980. Stratigraphy of South Africa, Part 1, in: Kent, L.E. (Ed.), Lithostratigraphy of the Republic of South Africa, South West Africa/Namibia and the Republics of Boputhatswana, Transkei and Venda: Handbook of the Geological Survey of South Africa,. pp. 690.

Safonov, Y.G., Prokof'ev, V.Y., 2006. Gold-bearing reefs of the Witwatersrand Basin: A model of synsedimentation hydrothermal formation. Geology of Ore Deposits **48**, pg 415–447.

Schidlowski, M., 1981. Uraniferous constituents of the Witwatersrand conglomerates: ore-microscopic observations and implications for the Witwatersrand metallogeny, in: Genesis of Uranium- and Gold-Bearing Precambrian Quartz-Pebble Conglomerates. US Geological Survey Professional Paper **1161N**. Golden, Colorado, pp. N1 – 29.

Seward, T.M., Williams-Jones, A.E., Migdisov, A.A., 2013. The Chemistry of Metal Transport and Deposition by Ore-Forming Hydrothermal Fluids, 2nd ed, Treatise on Geochemistry: Second Edition. Elsevier Ltd.

Shah, K.R., Filby, R.H., 1970. Determination of trace elements in petroleum by neutron activation analysis. Journal of Radioanalytical and Nuclear **6**, pg 413 – 422.

Shaikjee, A., Coville, N.J., 2012. The role of the hydrocarbon source on the growth of carbon materials. Carbon **50**, pg 3376–3398.

Simanovich, I.M., 2009. Auriferous Precambrian conglomerates of Witwatersrand. Lithology and Mineral Resources **44**, pg 497–509.

Simpson, P.R., Bowles, J.F.W., 1977. Uranium Mineralization of the Witwatersrand and Dominion Reef Systems. Philosophical Transactions of the Royal Society A: Mathematical, Physical and Engineering Sciences **286**, pg 527–548.

Smart, K.A., Tappe, S., Stern, R.A., Webb, S.J., Ashwal, L.D., 2016. Early Archaean tectonics and mantle redox recorded in Witwatersrand diamonds. Nature Geoscience **9**, pg 1–6.

Smieja-Król, B., Duber, S., Rouzaud, J.N., 2009. Multiscale organisation of organic matter associated with gold and uranium minerals in the Witwatersrand basin, South Africa. International Journal of Coal Geology **78**, pg 77–88.

Smith, N.D., Minter, W.E.L., 1980. Sedimentological controls of gold and uranium in two Witwatersrand paleoplacers. Economic Geology **75**, pg 1–14.

Smits, G., 1984. Some Aspects Of The Uranium Minerals In Witwatersrand Sediments Of The Early Proterozoic. Precambrian Research **25**, pg 37–59.

Spangenberg, J.E., Frimmel, H.E., 2001. Basin-internal derivation of hydrocarbons in the Witwatersrand Basin, South Africa: evidence from bulk and molecular δ13C data. Chemical Geology **173**, pg 339–355.

Stanistreet, I.G., McCarthy, T.S., 1991. Changing tectono-sedimentary scenarios relevant to the development of the Late Archaean Witwatersrand Basin. Journal of African Earth Sciences (and the Middle East) **13**, pg 65–81.

Stewart, R. a., Reimold, W.U., Charlesworth, E.G., 2004. Tectonosedimentary model for the Central Rand Goldfield, Witwatersrand Basin, South Africa. South African Journal of Geology **107**, pg 603–618.

Thostenson, E.T., Ren, Z., Chou, T.-W., 2001. Advances in the science and technology of carbon nanotubes and their composites: a review. Composites Science and Technology **61**, pg 1899–1912.

Tonžetić, I.Ž., 2015. Quantitative analysis of iron ore using SEM-based technologies. Iron Ore: Mineralogy, Processing and Environmental Sustainability 161pp.

Tucker, R.F., 1980. Sedimentology and Mineralogy of the Composite Reef on Cooke Section, Randfontein Estates Gold Mine, Witwatersrand, South Africa. MSc Thesis, University of the Witwatersrand.

Van der Westhuizen, W.A., De Bruiyn, H., Meintjes, P.G., 1991. The Ventersdorp supergroup: an overview. Journal of African Earth Sciences **13**, pg 83–105.

Williams-Jones, A.E., Bowell, R.J., Migdisov, A.A., 2009. Gold in solution. Elements **5**, pg 281–287.

Young, R.B., 1917. The Banket: A Study of the Auriferous Conglomerates of the Witwatersrand System and the Associated Rocks. Gurney & Jackson, London, 125 pp.

Zeh, A., Ovtcharova, M., Wilson, A.H., Schaltegger, U., 2015. The Bushveld Complex was emplaced and cooled in less than one million years - results of zirconology, and geotectonic implications. Earth and Planetary Science Letters **418**, pg 103–114.

Zezin, D.Y., Migdisov, A.A., Williams-Jones, A.E., 2007. The solubility of gold in hydrogen sulfide gas: An experimental study. Geochimica et Cosmochimica Acta **71**, pg 3070–3081.

Zhou, W., Han, Z., Wang, J., Zhang, Y., Jin, Z., Sun, X., Zhang, Y., Yan, C., Li, Y., 2006. Copper catalyzing growth of single-walled carbon nanotubes on substrates. Nano Letters **6**, pg 2987–2990.

Zumberge, J.E., Sigleo, A.C., Nagy, B., 1978. Molecular and Elemental Analyses of the Carbonaceous Matter in the Gold and Uranium Bearing Vaal Reef Carbon Seams, Witwatersrand Sequence. Minerals Science and Engineering **10**, pg 223–246.

Appendices